



UNIVERSIDADE ESTADUAL DE CAMPINAS
Faculdade de Engenharia Química

JULIANE FIATES

**UNDERSTANDING THE ROLE OF ELECTROLYTES AND
ELECTRODES ON LI-AIR BATTERIES THROUGH
MOLECULAR DYNAMICS SIMULATION**

*COMPREENDENDO O PAPEL DO ELETRÓLITO E DO
ELETRODO NA BATERIA LI-AR POR MEIO DE SIMULAÇÃO
DE DINÂMICA MOLECULAR*

CAMPINAS

2020

JULIANE FIATES

**UNDERSTANDING THE ROLE OF ELECTROLYTES AND ELECTRODES ON
LI-AIR BATTERIES THROUGH MOLECULAR DYNAMICS SIMULATION**

***COMPREENDENDO O PAPEL DO ELETRÓLITO E DO ELETRODO NA BATERIA
LI-AR POR MEIO DE SIMULAÇÃO DE DINÂMICA MOLECULAR***

Thesis presented to the Faculty of Chemical Engineering of the University of Campinas in partial fulfillment of the requirements for the degree of Doctor in Chemical Engineering.

Tese apresentada à Faculdade de Engenharia Química da Universidade Estadual de Campinas como parte dos requisitos exigidos para a obtenção do título de Doutora em Engenharia Química.

Supervisor/*Orientador*: GUSTAVO DOUBEK

Co-supervisor/*Coorientador*: LUÍS FERNANDO MERCIER FRANCO

ESTE TRABALHO CORRESPONDE À VERSÃO FINAL DA TESE DEFENDIDA PELA ALUNA JULIANE FIATES, E ORIENTADA PELO PROF. DR. GUSTAVO DOUBEK.

CAMPINAS

2020

Ficha catalográfica
Universidade Estadual de Campinas
Biblioteca da Área de Engenharia e Arquitetura
Rose Meire da Silva - CRB 8/5974

F442u Fiates, Juliane, 1989-
Understanding the role of electrolytes and electrodes on Li-air batteries through molecular dynamics simulation / Juliane Fiates. – Campinas, SP : [s.n.], 2020.

Orientador: Gustavo Doubek.
Coorientador: Luís Fernando Mercier Franco.
Tese (doutorado) – Universidade Estadual de Campinas, Faculdade de Engenharia Química.

1. Baterias. 2. Eletrodos. 3. Eletrólitos. 4. Dinâmica molecular. I. Doubek, Gustavo, 1984-. II. Franco, Luís Fernando Mercier, 1988-. III. Universidade Estadual de Campinas. Faculdade de Engenharia Química. IV. Título.

Informações para Biblioteca Digital

Título em outro idioma: Compreendendo o papel do eletrólito e do eletrodo na bateria Li-ar por meio de simulação de dinâmica molecular

Palavras-chave em inglês:

Batteries
Electrodes
Electrolytes
Molecular dynamics

Área de concentração: Engenharia Química

Titulação: Doutora em Engenharia Química

Banca examinadora:

Gustavo Doubek [Orientador]

Raphael Soeiro Suppino

Hudson Giovanni Zanin

Eudes Eterno Fileti

Pedro de Alcântara Pessoa Filho

Data de defesa: 16-09-2020

Programa de Pós-Graduação: Engenharia Química

Identificação e informações acadêmicas do(a) aluno(a)

- ORCID do autor: <https://orcid.org/0000-0003-1866-9039>

- Currículo Lattes do autor: <http://lattes.cnpq.br/4806780326753043>

Folha de Aprovação da Defesa de Tese de Doutorado defendida por JULIANE FIATES em 16 de setembro de 2020 pela banca examinadora constituída pelos doutores.

Prof. Dr. Gustavo Doubek - Presidente e Orientador
FEQ / UNICAMP
(Videoconferência)

Prof. Dr. Raphael Soeiro Suppinno
FEQ / UNICAMP
(Videoconferência)

Prof. Dr. Hudson Giovani Zanin
FEEC / UNICAMP
(Videoconferência)

Dr. Eudes Eterno Fileti
Instituto de Ciência e Tecnologia da Universidade Federal de São Paulo
(Videoconferência)

Dr. Pedro de Alcântara Pessôa Filho
Escola Politécnica da USP
(Videoconferência)

A Ata da defesa com as respectivas assinaturas dos membros encontra-se no SIGA/Sistema de Fluxo de Dissertação/Tese e na Secretaria do Programa da Unidade.

To my Parents, Zelinda and Ary.

Acknowledgment

First, I would like to thank God for always guiding my journey through this life and giving me incredible opportunities for personal and professional growth.

Second, I would like to thank my family for all the support and love that they gave to me during my whole life, but especially at these past four years.

I am also deeply grateful for my supervisors, Dr. Gustavo Doubek and Dr. Luís Fernando Mercier Franco, for all the support and for always believing in my potential. I would like to especially thank Dr. Edward Joseph Maginn for receiving me in his group and for all time he spent guiding and teaching me; without his help most part of this work would not be possible. I am also grateful for all the help Dr. Yong Zhang gave me and for all the precious discussions that enriched my knowledge on thermodynamics and MD simulation.

Thanks are also due to my lab-mates in Brazil for their friendship during this time at FEQ-Unicamp, especially Lorrane Cristina Cardozo Bonfim Oliveira and Letícia Frigério Cremasco who always supported me since the beginning of our group. I would like to thank my colleagues at the University of Notre Dame for all friendship and knowledge shared with me during my period abroad, especially Bridgette Befort and Jialu Wang who made my life abroad more happy and colorful.

I would like to thank my Teaching Assistance Program Supervisor, Dr. Marco Aurélio Cremasco, who inspired me to be an ethical professional and to follow the academic path. I am also grateful for the students with which I worked. They taught me more than I taught them.

I also would like to thank my colleagues at PUC-Campinas who I had the pleasure to work with, especially Betânia Hoss Lunelli, José Antonio Carnevalli, Kristiane Cêra Carvalho and Leandro Alonso Xastre who are big inspirations to me. I am also grateful for all the students with which I had the pleasure to participate in the formation. In especial the former First Class of Chemical Engineering and all my supervised students.

Thanks are also due to Leandro Negrini Zanotto for helping me with my programing

questions and for introducing me to Professor Guido Costa Souza de Araújo who let me use the CCES cluster and gave me my first insights into parallel programming and CUDA employment for simulation. I would also like to thank my friend Rodrigo de Lima Amaral for teaching me to draw using open source programs and helping me to create some figures used in this thesis. Thanks to my English teacher Mary Anne Rugeroni who helped me to get through all the scholarship process to make part of PhD abroad and, my yoga teacher Naira Rodrigues who guided me to develop self-knowledge and to handle my emotions during this past four years.

My gratitude also goes to my close friends Jacqueline Inácio de Oliveira and Carla Sant'Ana Razori who are always at my side motivating me, thanks for your love. I would like also to thank Daniella Rebouças who received me in the USA and helped me with my first steps abroad. And finally, my gratitude to my friend Jacob Gerace who was always available for answering my questions and who "saved" my life several times in the USA, thanks for helping me with the English correction of this thesis.

Thanks are also due to the Center for Computing in Engineering & Sciences (CCES) (FAPESP grant 2013/08293-7) at the University of Campinas and the Center for Research Computing (CRC) at the University of Notre Dame for the computational resources, which were essential for the development of this thesis. This study was financed in part by the Coordenação de Aperfeiçoamento de Pessoal de Nível Superior - Brasil (CAPES) - Finance Code 001 and by the Conselho Nacional de Desenvolvimento Científico e Tecnológico - Brasil (CNPq) - Reference Number 203393/2018-0. This work was also supported by FAPESP grant 2017/11958-1, Shell, and the strategic importance of the support given by ANP (Brazil's National Oil, Natural Gas and Biofuels Agency) through the R&D levy regulations. I would also like to thank the University of Campinas and the University of Notre Dame for the structure and all the employees and professors which in somehow contributed to this work.

I also would like to thank the committee members who spent their time to evaluate and contribute to this doctoral thesis.

“..it’s not about winning. But what it’s about is not giving up. If you have a dream, fight for it. There’s a discipline for passion. And it’s not about how many times you get rejected or you fall down or you’re beaten up. It’s about how many times you stand up and are brave and you keep on going.”

Lady Gaga, The Oscar Award 2019.

Abstract

The increase in CO₂ emissions and the agenda proposed by some countries to ban on fossil-fuelled cars are motivating the development of efficiency batteries. The lithium-air battery is a good candidate because of its high energy density which is comparable to the gasoline combustion. However, several challenges need to be overcome for lithium-air batteries to be commercially viable. One of which is understanding the role that each battery component plays on the reaction pathway in order to achieve higher cyclability (discharge/charge). Data presented in this work was derived from molecular dynamics simulation (MD). Two scenarios were evaluated: the behavior of the bulk electrolyte with different anions and the interaction of the electrolyte with the electrode interface during discharge. The first project shows that anions with different shapes can result in similar Li⁺ transport, however, the solvation shell may differ. It may have impact on reaction mechanism since Li⁺ solvation structure plays an important role on Li⁺'s reaction with O₂. The second project explored the impact of electrode material and solvent choice on the behavior of electrolyte (especially Li⁺) under the presence of electric charge. The results show that both electrode and solvent impact the interface behavior in different ways. This suggests that a synergistic effect might be considered when selecting battery materials to achieve good reaction reversibility and therefore increasing the cycling number during battery life time. The findings and discussion highlighted in this thesis can be a valuable source for experimentalists to propose reaction pathways based on the macroscopic observations and the insights of molecular phenomena presented here.

Keywords: Li-air battery, MD simulation, electrolyte, anion shape, interface simulation, electrode, solvent.

Resumo

O aumento das emissões de CO_2 e a agenda proposta por alguns países para proibir carros movidos a combustíveis fósseis estão motivando o desenvolvimento de baterias de alta eficiência. A bateria de lítio-ar aparece como uma boa candidato devido à sua alta densidade de energia, comparável à combustão da gasolina. No entanto, vários desafios precisam ser superados para que as baterias de lítio-ar sejam comercialmente viáveis. Uma delas é entender o papel que cada componente da bateria desempenha no caminho da reação, a fim de obter maior ciclabilidade (descarga/carga). Os dados apresentados neste trabalho foram derivados de simulação de dinâmica molecular (MD). Dois cenários foram avaliados: o comportamento do eletrólito avaliando a região do seio do eletrólito utilizando diferentes ânions e a interação do eletrólito com a interface do eletrodo durante a descarga. O primeiro projeto mostra que os ânions com formas diferentes podem resultar em transporte Li^+ semelhante; no entanto, a estrutura de solvatação pode ser diferente. O que pode ter impacto no mecanismo de reação, uma vez que a estrutura de solvatação desempenha um papel importante na reação do Li^+ com o O_2 . O segundo projeto explorou o impacto do material do eletrodo e da escolha do solvente no comportamento do eletrólito (especialmente do Li^+) sob a presença de carga elétrica. Os resultados mostram que o eletrodo e o solvente afetam o comportamento da interface de diferentes maneiras. Isso sugere que um efeito sinérgico pode ser considerado na seleção dos materiais da bateria no sentido de se obter uma boa reversibilidade da reação e, portanto, aumentar o número de ciclos durante o tempo de vida da bateria. As descobertas e discussões evidenciadas nesta tese podem ser uma fonte valiosa para os experimentalistas proporem rotas reacionais baseados nas observações macroscópicas e nos *insights* de fenômenos moleculares apresentados aqui.

Palavras-chave: bateria de Li-ar, simulação DM, eletrólito, forma do ânion, simulação de interface, eletrodo, solvente.

List of Figures

Figure 1.1	Greenhouse gas emission (million metric of carbon dioxide equivalents) in the US in total and by economic sector in 2018 (reproduced from the United States Environmental Protection Agency ¹).	24
Figure 1.2	CO ₂ emission by transportation mode in the EU at 2016. Data to create this figure was taken from European Parliament web page ²	25
Figure 1.3	Comparison of practical energies densities and estimated driving range between selected rechargeable batteries. The range for all batteries was extrapolated from data from Nissan Leaf vehicles ³ using Li-ion batteries. For gasoline, the range was calculated based on the average distance driven an one tank. Data from energy densities was taken from Girishkumar <i>et al.</i> ⁴	25
Figure 2.1	A schematic representation of an aprotic lithium-air battery. The detail illustrates the porous carbon cathode flooded with the electrolyte, catalyst particles, and the product Li ₂ O ₂	30
Figure 2.2	Two main challenges in battery performance: (a) Current charge, and (b) Energy efficiency. The data for this figure is from Girishkumar <i>et al.</i> ⁴ . . .	31
Figure 2.3	A schematic of the ORR mechanism as a function of solvent DN. Adapted from Johnson <i>et al.</i> ⁵	33
Figure 2.4	Examples of systems which simulate: (a) EMD, (b) NEMD with direct shear flow perturbation, (c) NEMD with oscillatory shear flow perturbation, and (d) NEMD with heat flux perturbation (red - hot side; blue - cold side).	39

Figure 3.1	All-atom representations of DMSO, Li^+ , PF_6^- , and Pyr^- . Color code: oxygen (red), sulfur (yellow), carbon: (cyan), hydrogen: (white), lithium (magenta), phosphorus (orange), fluorine (green), and nitrogen (blue).	46
Figure 3.2	Density of LiPF_6 and LiPyr in DMSO solutions as a function of salt molality at 298 K and 1 atm.	50
Figure 3.3	Density of pure DMSO as a function of temperature at 1 atm. Experimental measurements were taken from literature ^{6,7}	51
Figure 3.4	Shear viscosity of LiPF_6 and of LiPyr in DMSO solutions at 1 atm as a function of: (a) salt molality at 298 K, and (b) temperature for solutions with $1 \text{ mol}\cdot\text{kg}^{-1}$ (simulation and experimental ^{6,7} values for pure DMSO are also shown for comparison purposes). Uncertainties are on the order of $\pm 0.1 \text{ mPa}\cdot\text{s}$ for all simulated results.	51
Figure 3.5	Self-diffusion coefficients of Li^+ and PF_6^- in DMSO solution of LiPF_6 , and of Li^+ and Pyr^- in DMSO solution of LiPyr , at 1 atm as a function of: (a) salt molality at 298 K, and (b) temperature for solutions with $1 \text{ mol}\cdot\text{kg}^{-1}$ (The self-diffusion coefficients of DMSO in the salt solutions are also shown). The error bars at the lowest temperature are smaller than the symbol size.	52
Figure 3.6	Ionic conductivity of LiPF_6 and LiPyr in DMSO solutions at 1 atm as a function of: (a) salt molality at 298 K (experimental data values for concentrations of $0.1 \text{ mol}\cdot\text{kg}^{-18}$ and $1 \text{ mol}\cdot\text{kg}^{-19}$ of LiPF_6 in DMSO are also presented), and (b) temperature for solutions with $1 \text{ mol}\cdot\text{kg}^{-1}$. Nernst-Einstein (NE) ionic conductivities are shown for comparison purposes. The uncertainties for NE ionic conductivities were propagated from the uncertainties of the corresponding diffusion coefficients. The error bars at the lowest temperature are smaller than the symbol size.	53

Figure 3.7	The Nernst-Einstein deviation parameter, Δ , for LiPF_6 and LiPyr in DMSO solutions at 1 atm as a function of: (a) salt molality at 298 K, and (b) temperature for solutions with $1 \text{ mol}\cdot\text{kg}^{-1}$. The uncertainties were propagated from the uncertainties of the corresponding conduction coefficients.	54
Figure 3.8	Walden plot for LiPF_6 and LiPyr in DMSO solutions, using both calculated ionic conductivity and the calculated Nernst-Einstein (NE) ionic conductivity for different temperatures. Some error bars cannot be seen because they are smaller than the symbol size. Note the different scales in X and Y-axes.	55
Figure 3.9	Radial distribution functions (RDF) (solid lines, left y axis), and coordination numbers (dashed lines, right y axis) for Li-O (DMSO) - red. Li-F(PF_6) - black, and Li-P(PF_6) - green at 298 K and 1 atm for $1.0 \text{ mol}\cdot\text{kg}^{-1}$ DMSO solution of LiPF_6 . The inset plot shows the solvation structure of Li^+ . The distances are in Angstrom. Atom color code: lithium (magenta), oxygen (red), phosphorus (orange), and fluorine (green).	56
Figure 3.10	Radial distribution functions (RDF) (solid lines, left y axis), and coordination numbers (dashed lines, right y axis) for Li-O (DMSO) - red, Li-N(Pyr) - black, Li-H4(Pyr) - blue, and Li-Ha(Pyr) - green at 298 K and 1 atm for $1.0 \text{ mol}\cdot\text{kg}^{-1}$ DMSO solution of LiPyr . The inset plot shows the solvation structure of Li^+ . The distances are in Angstrom. Atom color code: lithium (magenta), oxygen (red), nitrogen (blue), carbon (cyan), and hydrogen (white).	56

Figure 3.11 Solvation: (a) Li^+ coordination numbers for the first shell shown in Figures 4.9 and 3.10 as function of molality at 298 K (Experimental data taken from ¹⁰ are also shown), and (b) as function of temperature for solutions with $1 \text{ mol}\cdot\text{kg}^{-1}$, (c) probability distribution of Li^+ coordination environment in the first solvation shell for O from DMSO, F from PF_6^- , and N for Pyr^- at $1 \text{ mol}\cdot\text{kg}^{-1}$ and 298 K.	58
Figure 3.12 The Li^+ transference number (t^+) for LiPF_6 and LiPyr in DMSO solutions at 1 atm and 298 K for different molalities calculated from Green-Kubo diffusivity. Uncertainties are on the order of ± 0.0001 for all results. Experimental measurements for LiPF_6 and LiBF_4 in PC ¹¹ and, simulation results for poly(allylglycidyl ether-lithium sulfonate) (PAGELS) in DMSO ¹² are also shown for comparison purposes.	59
Figure 4.1 Schematic representation of the simulated systems: (a) gold electrodes and DMSO/ LiPF_6 electrolyte, (b) graphene electrodes and DMSO/ LiPF_6 electrolyte, and (c) graphene electrodes and TEGDME/ LiPF_6 electrolyte. Electrolyte atom color code: oxygen (red), hydrogen (white), carbon (cyan), sulfur (yellow), lithium (magenta), phosphorus (orange), and fluorine (green).	66
Figure 4.2 Local concentration profiles of: ions (left y axis) and DMSO solvent (right y axis). DMSO (this work) - black solid line, DMSO (Sergeev <i>et al.</i> ¹³) - red dot dashed line; Li^+ (this work) - magenta dotted line, Li^+ (Sergeev <i>et al.</i> ¹³) - yellow long dashed line; PF_6^- (this work) - green dashed line, PF_6^- (Sergeev <i>et al.</i> ¹³) - blue dot dot dashed line. Surface charges applied: (a) zero, (b) $-4.85 \mu\text{C}\cdot\text{cm}^{-2}$, and (c) $-9.7 \mu\text{C}\cdot\text{cm}^{-2}$. The insets show the visualization of ions and electrodes (left-negative and right-positive). Atom color code: gold (yellow), lithium (magenta), phosphorus (orange), and fluorine (green).	69

Figure 4.3	Local concentration profiles of: ions (left y axis) and DMSO solvent (right y axis). DMSO - black solid line; Li^+ - magenta dotted line; PF_6^- - green dashed line. Surface charges applied: (a) zero, (b) $-4.85 \mu\text{C}\cdot\text{cm}^{-2}$, and (c) $-9.7 \mu\text{C}\cdot\text{cm}^{-2}$. The insets show the visualization of ions and electrodes (left-negative and right-positive). Atom color code: graphene (gray), lithium (magenta), phosphorus (orange), and fluorine (green).	70
Figure 4.4	Local concentration profiles of: ions (left y axis) and TEGDME solvent (right y axis). TEGDME - black solid line; Li^+ - magenta dotted line; PF_6^- - green dashed line. Surface charges applied: (a) zero, (b) $-4.85 \mu\text{C}\cdot\text{cm}^{-2}$, and (c) $-9.7 \mu\text{C}\cdot\text{cm}^{-2}$. The insets show the visualization of ions and electrodes (left-negative and right-positive). Atom color code: graphene (gray), lithium (magenta), phosphorus (orange), and fluorine (green).	71
Figure 4.5	Order parameter ($P_2(\cos \theta)$) for DMSO in gold (red dot-dashed line) and graphene (black solid line) electrode systems subjected to different surface charges: (a) zero, (b) $-4.85 \mu\text{C}\cdot\text{cm}^{-2}$, and (c) $-9.7 \mu\text{C}\cdot\text{cm}^{-2}$	72
Figure 4.6	DMSO ordering: (a) $P_2(\cos \theta) = -0.5$, and (b) $P_2(\cos \theta) = 1$. Li^+ solvation by O from solvent: (c) in DMSO (the oxygen atoms came from three different molecules), and (d) in TEGME (the dashed line represents that the oxygen atoms came from only one molecule).	74
Figure 4.7	Free energy profile ($W(z)$) for lithium near the electrodes for (a) gold/DMSO, (b) graphene/DMSO, and (c) graphene/TEGDME.	76
Figure 4.8	Potential profiles near the left electrode (negative) increasing the charge density (the bulk was set to 0 V): (a) at DMSO solvent and gold electrode, (b) at DMSO solvent and graphene electrode, and (c) at TEGDME solvent and graphene electrode.	78

Figure 4.9	Voltage drop ($\phi - \phi_z$) between electrode and electrolyte as a function of the electrode surface charge density (σ) (left y axis). The amount of Li^+ adsorbed (%) in the first layer at electrode surface as a function of the electrode surface charge density (σ) (right y axis). Filled symbols and dashed lines represent the voltage drop. Opened symbols and solid lines represent the % of Li^+ adsorbed. Red square - DMSO solvent and gold electrode; blue circle - DMSO solvent and graphene electrode; black triangle - TEGDME solvent and graphene electrode.	79
Figure A.1	The shear viscosity corresponding to the running integral (Eq. 2) averaged over 30 trajectories (dashed line) and the fitting empirical function (Eq. 3) (solid line) at $1 \text{ mol}\cdot\text{kg}^{-1}$ and 298 K for: (a) LiPF_6 , and (b) LiPyr	101
Figure A.2	Self-diffusion corresponding to the running integral (Eq. 6) averaged over 10 trajectories (dashed line) and the fitting empirical function (Eq. 7) (solid line) at $1 \text{ mol}\cdot\text{kg}^{-1}$ and 298 K for: (a) Li^+ in solution with PF_6^- , (b) Li^+ in solution with Pyr^- , (c) PF_6^- , and (d) Pyr^- . The insets show the normalized velocity autocorrelation function (VACF).	102
Figure A.3	Ionic conductivity corresponding to the running integral (Eq. 9) averaged over 10 trajectories (dashed line) and the fitting empirical function (analogous to Eq. 7) (solid line) at $1 \text{ mol}\cdot\text{kg}^{-1}$ and 298 K for: (a) LiPF_6 , and (b) LiPyr . The insets show the normalized electrical current autocorrelation function (JACF).	102
Figure A.4	System size effect on the transport properties of LiPF_6 in DMSO and LiPyr in DMSO both at $1 \text{ mol}\cdot\text{kg}^{-1}$ and 298 K: (a) Self-diffusion coefficients without size effect correction, (b) Self-diffusion coefficients of Li^+ of LiPF_6 in DMSO without correction and corrected, and (c) Ionic conductivity coefficients.	104

Figure A.5	Radial distribution functions (RDF) (solid lines, left y axis), and coordination numbers (dashed lines, right y axis) for LiPF ₆ in solution with DMSO as function of: (a) concentration at 298 K for Li–O (DMSO), (b) concentration at 298 K for Li–F (PF ₆), (c) temperature at 1.0 mol·kg ⁻¹ for Li–O (DMSO), and (d) temperature at 1.0 mol·kg ⁻¹ for Li–F (PF ₆).	106
Figure A.6	Radial distribution functions (RDF) (solid lines, left y axis), and coordination numbers (dashed lines, right y axis) for LiPyr in solution with DMSO as function of: (a) concentration at 298 K for Li–O (DMSO), (b) concentration at 298 K for Li–N (Pyr), (c) temperature at 1.0 mol·kg ⁻¹ for Li–O (DMSO), and (d) temperature at 1.0 mol·kg ⁻¹ for Li–N (Pyr).	107
Figure A.7	Solvation probability distribution of the first shell layer at: (a) 0.25 mol·kg ⁻¹ and 298 K, (b) 0.50 mol·kg ⁻¹ and 298 K, (c) 0.75 mol·kg ⁻¹ and 298 K, (d) 1.00 mol·kg ⁻¹ and 330 K, (e) 1.00 mol·kg ⁻¹ and 360 K,	108
Figure A.8	Schematic illustrations of molecular structures for DMSO, PF ₆ ⁻ , Li ⁺ , and Pyr ⁻ with assignment of atom types.	109
Figure C.1	TEGDME molecule charge assignment for each atom ¹⁴ . Color code: oxygen (red), hydrogen (white), carbon (cyan).	145
Figure C.2	Local concentration profiles and standard deviation for gold/DMSO systems: ions (left y axis), and solvent (right y axis). DMSO - black solid line; Li ⁺ - magenta dotted line; PF ₆ ⁻ - green dashed line. Surface charges applied: (a) zero, (b) -4.85 μC·cm ⁻² , and (c) -9.7 μC·cm ⁻² . The shaded area represents the standard deviation.	147

Figure C.3	Local concentration profiles and standard deviation for graphene/DMSO systems: ions (left y axis), and solvent (right y axis). DMSO - black solid line; Li^+ - magenta dotted line; PF_6^- - green dashed line. Surface charges applied: (a) zero, (b) $-4.85 \mu\text{C}\cdot\text{cm}^{-2}$, and (c) $-9.7 \mu\text{C}\cdot\text{cm}^{-2}$. The shaded area represents the standard deviation.	148
Figure C.4	Local concentration profiles and standard deviation for graphene/TEGDME systems: ions (left y axis), and solvent (right y axis). TEGDME - black solid line; Li^+ - magenta dotted line; PF_6^- - green dashed line. Surface charges applied: (a) zero, (b) $-4.85 \mu\text{C}\cdot\text{cm}^{-2}$, and (c) $-9.7 \mu\text{C}\cdot\text{cm}^{-2}$. The shaded area represents the standard deviation.	149
Figure C.5	Gold/DMSO profiles along z -direction for uncharged and charged electrodes: (a) charge density ($\rho_q(z)$), and (b) electric field ($E(z)$). . . .	150
Figure C.6	Graphene/DMSO profiles along z -direction for uncharged and charged electrodes: (a) charge density ($\rho_q(z)$), and (b) electric field ($E(z)$). . . .	151
Figure C.7	Graphene/TEGDME profiles along z -direction for uncharged and charged electrodes: (a) charge density ($\rho_q(z)$), and (b) electric field ($E(z)$).152	

List of Tables

Table 3.1	Density of $1 \text{ mol}\cdot\text{kg}^{-1}$ LiPF_6 in DMSO solution, and of $1 \text{ mol}\cdot\text{kg}^{-1}$ LiPyr in DMSO solution, as a function of temperature at 1 atm.	50
Table 3.2	The Li^+ transference number (t^+) for LiPF_6 and LiPyr in DMSO solutions with $1 \text{ mol}\cdot\text{kg}^{-1}$ at different temperatures at 1 atm, calculated from Green-Kubo diffusivity ^a	59
Table 4.1	Coordination number calculated from running integrals of the radial distribution functions of Li^+ and O (from the solvent)	74
Table 4.2	Differential capacitance of each electrical double layer	80
Table A.1	Coordination numbers of the first solvation shell for Li-O (DMSO), $\text{Li-F}(\text{PF}_6)$ and $\text{Li-N}(\text{Pyr})$ at 1 atm for different salt molalities and at different temperatures.	105
Table C.1	Force field parameters for nonbonded interactions	145
Table C.2	Force field parameters for bonded interactions	146

Contents

1	Introduction	24
1.1	Objective	26
1.2	Thesis outline	27
1.3	Supplemental information	27
2	Literature review	29
2.1	The lithium-air battery and its challenges	29
2.1.1	Electrochemical mechanisms	32
2.1.1.1	Oxygen Reduction Reaction (ORR)	32
2.1.1.2	Oxygen Evolution Reaction (OER)	34
2.1.2	Electrolyte	34
2.1.3	Electrode	36
2.2	Molecular Dynamics Simulation	37
2.2.1	Transport properties calculation	38
2.2.2	Electrified electrolyte/electrode interface simulation	40
3	Impact of anion shape on Li⁺ solvation and on transport properties for lithium-air batteries: a molecular dynamics study	43
3.1	Abstract	43
3.2	Introduction	44
3.3	Computational details	46
3.3.1	Force fields	46
3.3.2	Molecular dynamics simulations	47

3.3.3	Transport properties calculation	47
3.4	Results and discussion	49
3.4.1	Density	49
3.4.2	Transport properties	51
3.4.3	Structural arrangement	55
3.4.4	Consequences for Li-Air battery	59
3.5	Conclusions	61
3.6	Permission to reproduction	62
4	Effect of electrode material and solvent donor number in Li-air battery: insights from Molecular Dynamics simulations	63
4.1	Abstract	63
4.2	Introduction	64
4.3	Simulation details	65
4.4	Results and discussion	67
4.4.1	Electrolyte local concentration	67
4.4.2	DMSO ordering and Li ⁺ solvation	71
4.4.3	Voltage drop between electrode and electrolyte	76
4.4.4	Final remarks	80
4.5	Conclusion	81
4.6	Acknowledgement	82
5	Discussion	83
6	Conclusions and future work	85
6.1	Conclusions	85
6.2	Future work	86
	References	87

Appendix A	Electronic supplementary information (ESI) for: Impact of anion shape on Li⁺ solvation and on transport properties for lithium-air batteries: a molecular dynamics study	100
A.1	Time correlation functions	101
A.2	System size analysis	103
A.3	Structural arrangement	105
A.4	Simulation details	109
A.4.1	Molecular sketches	109
A.4.2	Dimethyl sulfoxide molecule	109
A.4.3	Hexafluorophosphate molecule	110
A.4.4	Lithium molecule	111
A.4.5	Pyrrrolide molecule	112
A.4.6	Force field for DMSO/LiPF ₆	113
A.4.7	Force field for DMSO/LiPyr	114
A.4.8	LAMMPS initialization file for DMSO/LiPF ₆	116
A.4.9	LAMMPS initialization file for DMSO/LiPyr	118
Appendix B	Codes to calculate transport and structural properties	120
B.1	Viscosity code	120
B.2	Self-diffusion code	125
B.3	Ionic conductivity code	129
B.4	Radial distribution function and coordination number code	137
B.5	Average and standard deviation code	141
Appendix C	Supporting Information for: Effect of electrode material and solvent donor number in Li-air battery: insights from Molecular Dynamics simulations	144
Appendix D	LAMMPS and codes files to simulate and calculate properties on confined systems	153
D.1	LAMMPS running file	153
D.2	Post processing codes	156

D.2.1	Density distribution and free energy profile ($W(z)$) code	157
D.2.2	Integral of the normalized concentration code	161
D.2.3	Radial distribution function and coordination number code	164
D.2.4	Order parameter code ($P_2(\cos \theta)$)	169
D.2.5	Charge density and electric field code	173
D.2.6	Electrostatic potential code	177
D.2.7	Electrostatic potential calculation using LAMMPS	179

Chapter 1

Introduction

The world is facing an increase in average temperature which is associated with greenhouse gas emissions. Data from the United States Environmental Protection Agency-EPA¹ shown in Figure 1.1 presents the amount of greenhouse gas production in the United States (US) in 2018 based on the emissions in million metric tons of carbon dioxide equivalents. Figure 1.1 clearly illustrates that CO₂ plays an important role on the air pollution. The distribution among different sectors shows that transportation has the highest impact on gas emissions. As shown in Figure 1.2, it is undoubtedly seen that in the transport sector, cars have the largest impact to CO₂ emissions, accounting for around 60% of emitted gas. The fossil fuels combustion are responsible for 97% of produced CO₂¹. Thus, the desire to use sustainable energy sources is motivating the reduction to use fossil fuels. Along with this, some countries are approving an agenda for replacement of fossil-fuelled cars to fully-electric cars¹⁵.

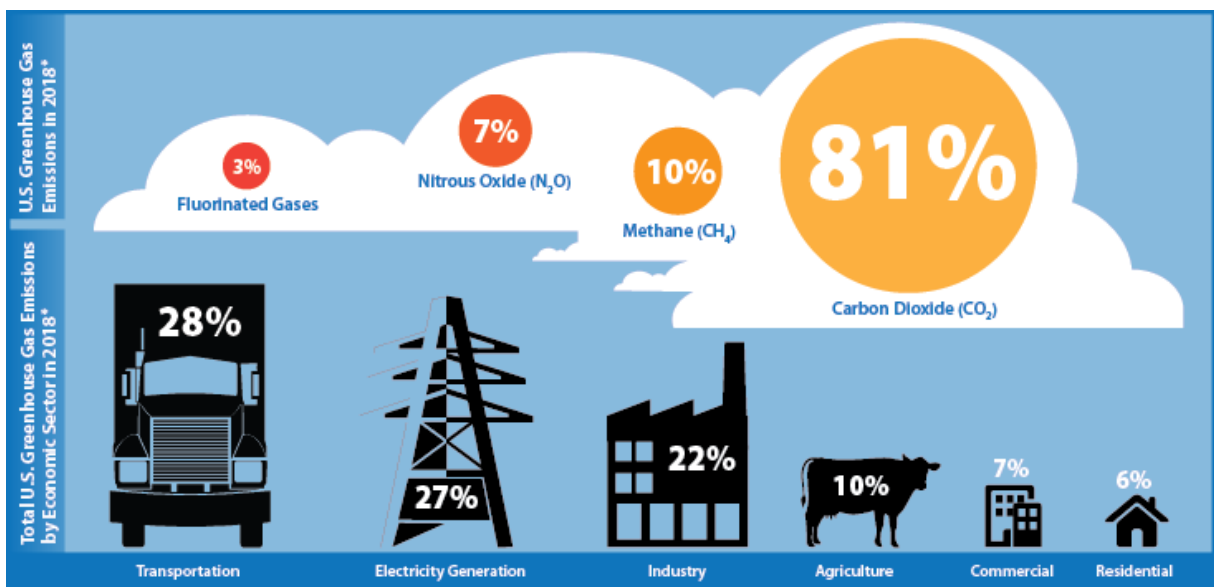


Figure 1.1: Greenhouse gas emission (million metric of carbon dioxide equivalents) in the US in total and by economic sector in 2018 (reproduced from the United States Environmental Protection Agency¹).

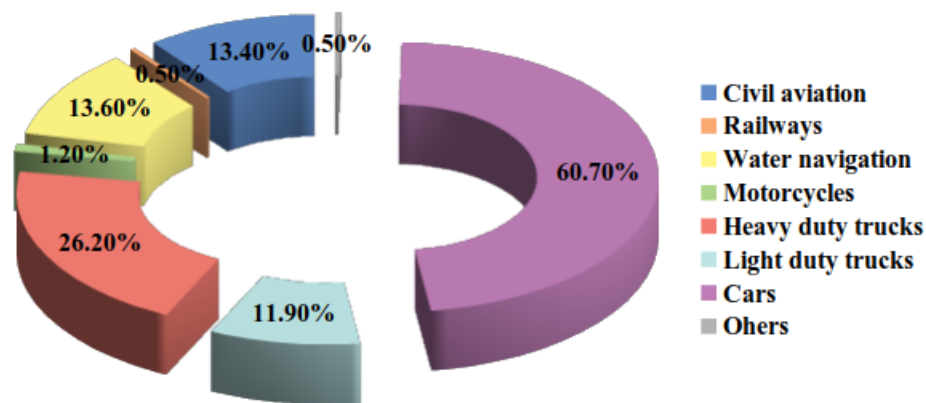


Figure 1.2: CO₂ emission by transportation mode in the EU at 2016. Data to create this figure was taken from European Parliament web page².

In this context, the development of advanced energy storage devices appears as a possibility to turn feasible the transition from internal combustion vehicles to fully electric drive. The lithium-ion battery, the dominant battery technology used in portable electronics, has already achieved its theoretical limit (around 300 Wh/kg)^{4,16}. Therefore, the development of novel high energy density batteries is essential to overcome limitation of the actual system. In recent years the lithium-oxygen/air battery has received great attention because of its high practical energy density (1700 Wh/kg), which is comparable to gasoline⁴. Figure 1.3 presents an overview of batteries technologies and estimated driving ranges based on data from the Nissan Leaf³ electric vehicle with a Li-ion battery system. It is possible to see that Li-O₂ batteries can provide almost double of driving range of a gasoline tank (~700 Km).

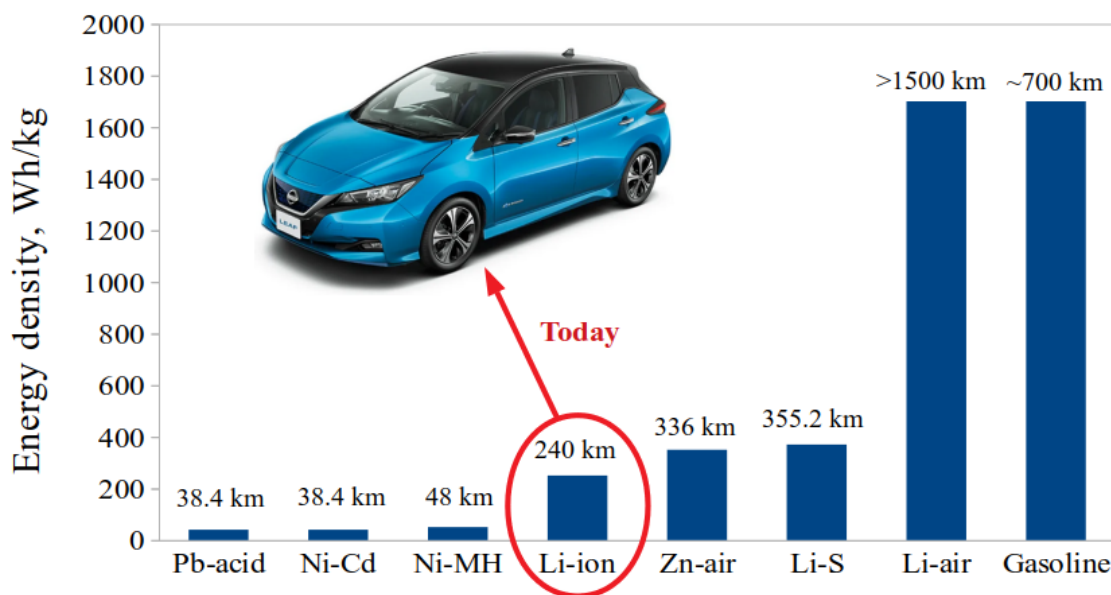


Figure 1.3: Comparison of practical energy densities and estimated driving range between selected rechargeable batteries. The range for all batteries was extrapolated from data from Nissan Leaf vehicles³ using Li-ion batteries. For gasoline, the range was calculated based on the average distance driven in one tank. Data from energy densities was taken from Girishkumar *et al.*⁴.

The lithium-air battery is a technology based on the storage of energy through oxidized species of lithium. The lithium-oxygen reaction takes place at a porous media known as cathode, which is commonly made of carbon based materials and catalysts. Lithium is provided by the formation of Li^+ ions from a metallic plate known as anode. The Li^+ ions are transported from anode to cathode by the electrolyte, which is composed by a solvent and a lithium salt. The battery cycle is composed by the discharge where the oxidation of lithium occurs and the charge where the reaction products are decomposed in Li^+ and O_2 .

Several issues need to be overcome to have a commercial $\text{Li}-\text{O}_2$ technology. Some of them consists on the selection of cathode materials, catalysts, as well as solvents and lithium salts. Others regard the operation safety and the utilization of atmospheric air. The dendrites formation in lithium anode can lead to battery explosion. Additionally, the employment of air can contribute to side reactions between Li^+ and other components present in the air.

Some experimental research has been carried out on lithium-air battery to solve limitations of the system, but the molecular behavior (mechanisms and molecular interactions) from key features of battery design including the role of cathode, catalyst, and electrolyte remains poorly understood. Most of the prior research was dedicated to overall battery parameters including cyclability, capacity, overpotentials, and characterization of reaction products¹⁷⁻²⁷. However, molecular scale phenomena that occurs at battery operation (for example, species interaction and individuals behavior during charge/discharge process^{13,28}) is still underreported.

Therefore, this thesis proposes a more complete evaluation of electrolyte and electrode conditions under operation through molecular dynamic simulation of bulk and confined systems. A full understanding of each battery element and their impact over the system is important to determine an optimal composition of electrolyte and electrode materials to achieve good reversibility and discharge/charge capacities for Li-air battery.

1.1 Objective

The aim of this work is to uncover the molecular interactions of the Li-air battery system through molecular dynamics simulation. The project described in this thesis addresses three specific steps developed to achieve the objective:

- Study the impact of anion choice on the transport and structural properties of the electrolyte.
- Analyze the impact of electrode and solvent materials on system behavior under electrical charge.

- Correlate the findings of topics above with experimental data from literature to contribute to the discussion about the impact of those variables over reaction pathways and battery performance.

1.2 Thesis outline

Chapter 1 gives a general introduction of Li-air battery importance and challenges.

Chapter 2 reviews previous literature on the Li-air system as well as computational methods to simulate and process data from bulk and confined systems.

Chapter 3 presents a first paper published in the *Physical Chemistry Chemical Physics Journal (PCCP)*. It describes property calculation of bulk electrolytes composed of different anions.

Chapter 4 presents a second paper which will be submitted to *The Journal of Physical Chemistry C*. It discusses the simulation of electrolytes confined by two electrodes, and analyzes different electrode materials and solvents types when subjected to electrical charges.

Chapter 5 discusses correlations between the literature review and the findings of both papers.

Chapter 6 gives conclusions and describes future work.

Appendix A consists of supplementary material published with the first paper.

Appendix B consists of all the codes developed to generate the results presented in the first paper.

Appendix C consists of supplementary material that will be submitted with the second paper.

Appendix D gives all inputs necessary to reproduce the molecular dynamics simulations used for the second paper, and all codes developed to process data and yield the results presented in the second paper.

1.3 Supplemental information

All simulations and analysis presented in this thesis were developed using the Ubuntu 16.04 LTS operation system. Molecular Dynamics simulations were run with LAMMPS (Large-scale Atomic/Molecular Massively Parallel Simulator)²⁹. MD visualizations were rendered using VMD (Visual Molecular Dynamics)³⁰. All plots were created using gnuplot 5.2³¹. All figures were drawn using Inkscape 1.0³². Post processing codes were

written in the C programming language. This thesis was written in \LaTeX environment using TeXstudio 2.12.6³³. All tools referenced above are free and open-source.

Chapter 2

Literature review

This literature review is composed of two main topics. The first regards the lithium-air battery system details such as design and operation as well as its hurdles. The second relies on the simulation approaches adopted to elucidate macroscopic behaviors and to help experimentalists on the development of optimized devices.

2.1 The lithium-air battery and its challenges

The concept of the lithium-air battery dates from 1974 when an aqueous battery was created by Littauer and Tsai^{34,35}. Since then a strong technological evolution on the system occurred. Currently, the most common type of battery is composed of an aprotic configuration³⁶. A typical aprotic Li-O₂ battery consists of an anodic electrode of metallic lithium, a porous air-breathing cathodic electrode that can be impregnated with active materials (catalysts), and an electrolyte composed by a lithium salt in an aprotic solvent^{4,36}. This scheme is presented in Figure 2.1.

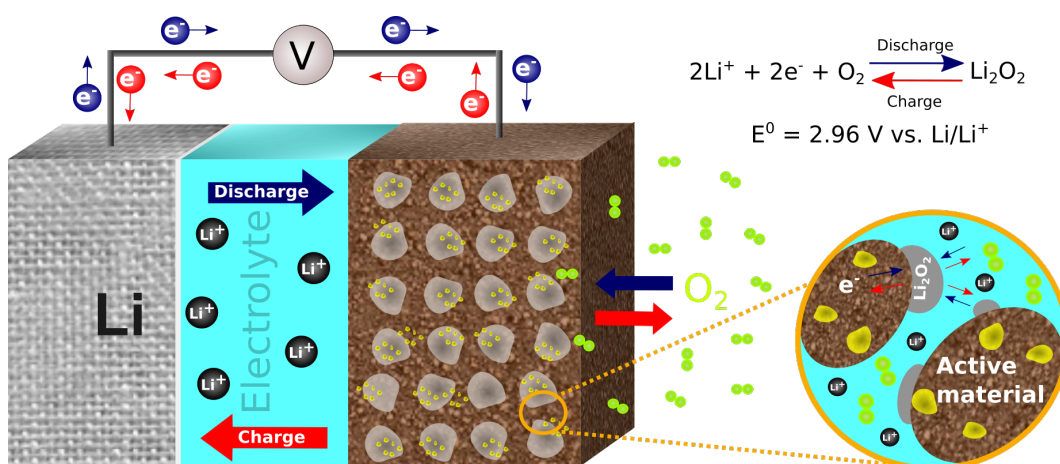


Figure 2.1: A schematic representation of an aprotic lithium-air battery. The detail illustrates the porous carbon cathode flooded with the electrolyte, catalyst particles, and the product Li_2O_2 .

Battery operation consists of cycles of discharge and charge. During discharge, lithium is oxidized at the anode producing electrons and Li^+ ions. Electrons are transported by the external circuit generating electrical work and leading to oxygen reduction at the cathode. The oxygen reduction reaction (ORR) occurs when reduced oxygen combines with Li^+ ions, transported through the electrolyte. The most common product of this reaction is lithium peroxide (Li_2O_2). The limited solubility of Li_2O_2 in the electrolyte leads to its accumulation in the pores of the cathode. During charging an external potential is applied to the air electrode. Thus, Li_2O_2 undergoes decomposition, producing electrons, Li^+ ions, and gaseous O_2 . This electrochemical reaction is known as oxygen evolution reaction (OER)^{4,36}.

Considering the complexity of this system a wide variety of challenges must be overcome for commercial viability. The two main operational hurdles are the limited current density and energy efficiency. A good discharge capacity is only achieved at low current densities ($0.1\text{-}0.5 \text{ mA} \cdot \text{cm}^{-2}$) as exemplified in Figure 2.2 (a); by comparison, Li-ion current densities are two orders of magnitude greater. When current density is increased a fast pore clogging process decreases free space available for the reaction, depending on the electrode's pre distribution. Additionally, the insulating nature of Li_2O_2 creates an electronic barrier that limits the electric current⁴.

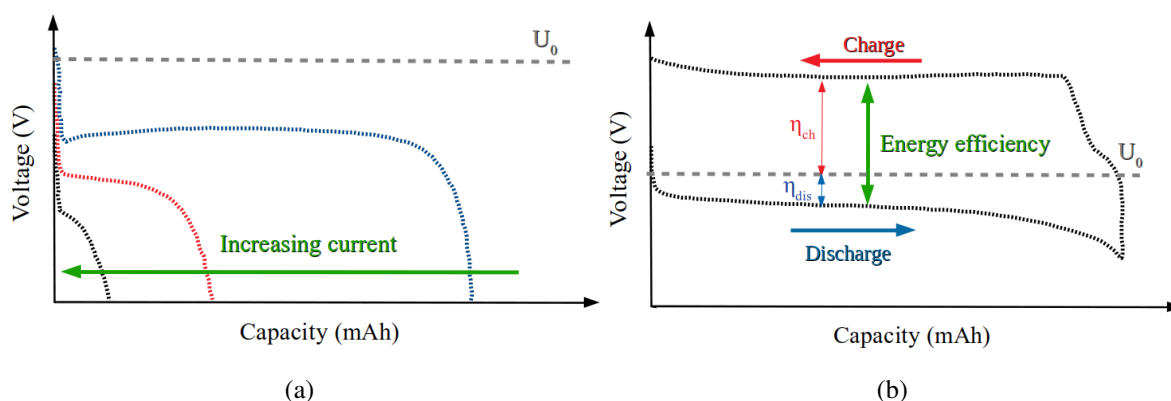


Figure 2.2: Two main challenges in battery performance: (a) Current charge, and (b) Energy efficiency. The data for this figure is from Girishkumar *et al.*⁴

Another issue is the high overpotentials shown in Figure 2.2 (b). The overpotential measures the difference between the charge and discharge potentials (around 1.0 V). This leads to a discharge-charge cycle energy efficiency of about 70% (3.8 V/2.7 V), which is lower compared to the 90% efficiency in Li-ion^{4,36}. As shown in Figure 2.2 (b) the charge (η_{ch}) and discharge (η_{dis}) overpotentials are a deviation from the equilibrium potential (U_0). Those differences are caused not only by the energy barriers for the kinetic process but also influenced by the strong build-up of insoluble discharge products at the cathode surface limiting the transport of reactants⁴. To solve this obstacle it is important to develop electrodes with controlled porosity in order to provide enough space for reaction products. Moreover, constraints related with activation polarization, which leads to low reaction velocities, need to be considered. The selection of catalytic materials are a way to solve this problem³⁷.

The aforementioned limitations also impact the number of discharge-charge cycles. As cycle number is increased the battery capacity strongly decreases. Tan *et al.*³⁶ report a cycle life lower than 500 cycles. As a comparison a Tesla Model S has a battery with around 1,000 to 2,000 discharge cycles³⁸.

A safety issue related with lithium dendrite formation is also addressed in the literature^{4,39}. The dendrite formation is caused by irregular current distribution along the interface of metal-electrolyte. Because of lithium high reactivity when in contact with electrolyte some reactions may occur. A passivation layer known as the SEI (solid electrolyte interphase) composed by the products of these reactions, appears at the metallic surface. The accumulation of these materials can create a morphological structure which enables heterogeneous current distribution, contributing to dendrite formation. These dendrites can lead to short circuits between the anode and the cathode⁴.

An operational issue is the consumption of pure oxygen instead of air. A pure O_2 atmosphere is used to avoid contaminations, such as H_2O and CO_2 , found in the air. Those

compounds would lead otherwise to side reactions which can form irreversible products thus degrading the system³⁶.

Several unresolved issues need to be overcome in order to make lithium-air aprotic batteries commercially viable. These issues, summarized, are³⁹:

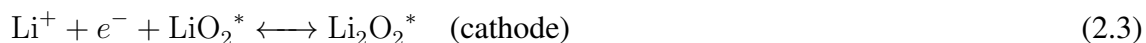
1. Selection of a nonaqueous electrolyte which improves oxygen solubility, Li⁺ diffusivity, and stabilization of the peroxide radical.
2. Selection of a catalyst that enables Li₂O₂ reduction.
3. The suppression of lithium dendrite formation.
4. Protection of the cathode from carbon dioxide and water in the ambient air.

2.1.1 Electrochemical mechanisms

The electrochemical reactions that occur during the Li-air battery charge and discharge are fundamental to the design of electrodes and the selection of electrolytes. The electrochemistry of this device will be explored in subsequent subsections.

2.1.1.1 Oxygen Reduction Reaction (ORR)

The Oxygen Reduction Reaction (ORR) occurs during the discharge process. Using first principles of thermodynamics a theoretical mechanism reaction was proposed by Hummelshøj and co-workers⁴⁰⁻⁴² as follows:



where * refers to a surface-adsorbed species.

In the case of aprotic electrolytes the products of reaction are insoluble (Nuclear magnetic resonance (NMR) studies have shown that the solubility at [Li⁺]=1 M is in order of < 10⁻¹⁰). Thus, the product (Li₂O₂^{*}) and its intermediate (LiO₂^{*}) are formed at the cathodic surface by the ion transfers and remain there permanently⁴².

Some authors^{20,42,43} suggest that the reactions presented above are composed of multiple steps. They suggest that Equation 2.2 occurs in two stages (Eq. 2.4 and 2.5) instead of the indicated ion transfer surface mechanism.





In this case oxygen suffers reduction in a one-electron transfer (Eq. 2.4), then in the presence of Li^+ it forms lithium superoxide (LiO_2^*) (Eq. 2.5). This intermediate product undergoes disproportionation (Eq. 2.6)^{20,43,44}, or undergoes another one-electron transfer electrochemical reaction forming solid Li_2O_2^* (Eq. 2.7)³⁶.



and/or



According to Tan *et al.*³⁶, different morphologies of Li_2O_2 (toroid, film, etc.) suggest different reactions pathways. Johnson *et al.*⁵ propose two reaction mechanisms (solution and surface), as illustrated in Figure 2.3, for different morphologies obtained using different donor number (DN) solvents.

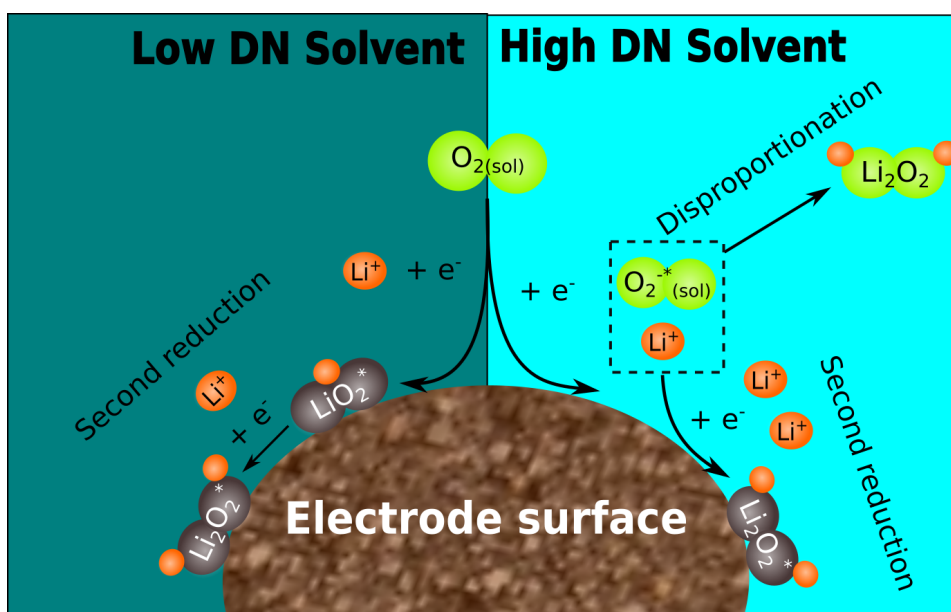
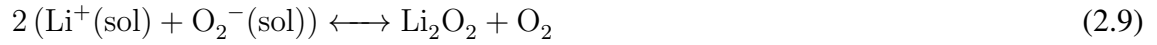
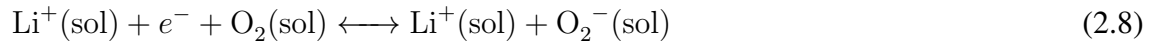


Figure 2.3: A schematic of the ORR mechanism as a function of solvent DN. Adapted from Johnson *et al.*⁵

The solution mechanism occurs in high DN solvents. In this case the Li_2O_2 forms in solution (dissolved in the electrolyte) and in surface (adsorbed in the surface). Both are in equilibrium according to the solubility-adsorption free energy. Even though the solution has prevalence of Li_2O_2 by disproportionation (Eq. 2.9), a one-electron electrochemical process also occurs forming Li_2O_2 at the surface (Eq. 2.10). In low DN number solvents the surface pathways occurs. In this situation, a reaction composed by two sequential one-electron transfer leads to Li_2O_2 insoluble formation at the oxygen electrode (Eqs. 2.11-2.13).

Solution Mechanism



Surface Mechanism



2.1.1.2 Oxygen Evolution Reaction (OER)

The reverse mechanism consists of the electrochemical decomposition of solid Li_2O_2 into Li^+ and O_2 . Thus, during charging an external potential is applied to the system leading to a $2e^-$ direct charge reaction (Eq. 2.14). It can also involve an intermediate step which by passes LiO_2^* formation^{36,42,44}.



The charge overpotential is in general large. This may be caused by the insulator property of Li_2O_2 . The model described here is oversimplified, however the details of Li_2O_2 decomposition is still poorly understand. The elucidation of ORR and OER reactions in aprotic electrolytes is a fundamental key to project optimized materials in order to decrease operation overpotentials³⁶.

2.1.2 Electrolyte

The electrolyte has a strong influence on the reactions for both the cathode and the anode. Device charge-discharge performance is strongly correlated with the electrolyte. In particular, the formation and decomposition of Li_2O_2 imposes a great challenge. Many electrolytes undergo decomposition especially during charging when they are subjected to an external potential. Electrolyte degradation in a battery leads to poor kinetics of discharge and charge, low cyclability and ending its life prematurely. Alongside this limitation the influence of cathode nature can play an important role in the electrolyte stability. Some essentials characteristics that may be present in a good electrolyte candidate include⁴⁵:

- *Conductivity*: sufficiently high to achieve the expected rate capability;

- *Stability*: within potential window applied to the charge-discharge cycle; in interaction with O_2 and its reduced species during discharge; in contact with Li_2O_2 and its intermediates during charge; at anode interface or at the stable SEI formed on the anode.
- *Low volatility*: to reduce evaporation at the porous cathode.
- *O_2 solubility and diffusivity*: to provide adequate mass flow at the cathode.
- *Li_2O_2 solubility*: to promote interaction with Li_2O_2 and its intermediates thereby enabling high rate and packing of Li_2O_2 .
- *Ability to wet the electrode surfaces*: to provide Li^+/O_2 diffusion.
- *Safety, low cost, and toxicity*.

A first step for electrolyte selection for a Li-air battery has focuses on organic carbonates, which are widely used in Li-ion batteries. Further research showed they were unsuitable due to side reactions which generates stable products^{17,45,46}. Following extensive investigation to find an aprotic electrolyte able to fulfill the requirements enumerated earlier, electrolytes based on ethers, amides, ionic liquids (IL), sulfones, and dimethyl sulfoxide (DMSO) have been identified to form and decompose Li_2O_2 during discharge and charge⁴⁵.

Some computational and experimental approaches have been used for the research of suitable electrolytes. Several quantum chemical calculations such as Density Functional Theory (DFT) were employed to understand the interaction of O_2 reduced products and the solvent. Free energies calculations have shown possible reaction pathways where O_2 or LiO_2 attack the solvent⁴⁵. Molecular dynamics simulation of Li^+ transport and ionic conductivity also contributed in the selection of electrolytes for systems where Li^+ transport is the limiting factor for battery operation⁴⁷. Experimental also play an important role in this process. Direct electrochemical measurement by cyclic voltammograms and cathode characterization techniques (i. e., Raman and mass spectroscopy etc.) has shown reaction between O_2 and the electrolyte; they also provide data to calculate oxygen concentration which is essential for battery operation^{45,47}.

Salt selection is also important for the electrolyte composition. Salt ions are responsible for provide the required conductivity. They play a vital role in interfacial phenomena such as SEI stability, conductivity, and current passivation^{45,47}. The earliest commonly used salt was $LiPF_6$, based on Li-ion technology. $LiPF_6$ is still in use, but others salts are being studied including $LiClO_4$, $LiBF_4$, $LiSO_3CF_3$, $LiNO_3$, and $LiN(SO_2CF_3)_2$ (TFSI). Analogous to the solvents, a usable salt requires high stability when exposed to reduced oxygen⁴⁵.

The electrolyte selection should be based on both experimental and simulation efforts. Understanding the reaction mechanism and mass transport through experimentation and simulation methods provides valuable guidance for the design of more stable electrolytes.

2.1.3 Electrode

The unique electrochemistry of Li-air battery requires a rational electrode project to provide high reaction activities³⁶. According to Laoire *et al.*²⁰ Carbon and Nickel foam has high discharge capacities. Additionally, Laoire *et al.*⁴³ demonstrated that by using an appropriate porous carbon electrode the Li-air cell can achieve high discharge-charge efficiency. Because the reaction product, Li_2O_2 , is insoluble in most electrolytes, porous electrodes with appropriate morphology, surface structure, pore volume, and surface area are crucial for enabling good battery performance during the oxygen reduction reaction (ORR) and oxygen evolution reaction (OER) cycles⁴³.

Along with those characteristics an appropriate material should have^{48,49}:

- A good electronic conductivity, due to the insulating profile of the Li_2O_2 .
- A high stability over the operating voltage (typically 2-4 V versus Li^+/Li), as the lower stability can lead to side reactions such as the formation of Li_2CO_3 . This undesired product can also contribute to electrolyte degradation.
- A low cost and should be non-toxic.

The electrode microstructure plays an important role in the electrode performance. It enhances the electrochemical accessibility and provides a shorter diffusion route to O_2 ⁵⁰. Some physical properties of the porosity of the cathode are addressed in the literature including porous size distribution and electrode thickness which impact on discharge capacity. Ding *et al.*⁵¹ have noticed a correlation between carbon pore size and cell capacity; they claim that larger pore size yields to higher capacity. Additionally, the wettability of the electrode by the electrolyte has a large impact⁵². Read⁵³ has shown that battery cell capacity is strictly related with the wetted electrode area, and is independent of the total surface area.

Tran *et al.*⁵⁴'s findings have shown that an electrical double layer governs the electrochemical phenomena in electrodes when soaked in an aprotic electrolyte. First, the authors claim that a three-phase interface (solid/liquid/gas) is essential for the reaction process, because the interface can provide a path for oxygen diffusion through electrolyte/electrode media. Second, micropores can be quickly blocked by reaction products at the beginning of the discharge, impeding future electrochemical reactions. Along with this, the solid lithium oxides are mostly present inside of these large pores. Finally, Tran *et al.*⁵⁴ note that the reduction reaction is connected with the lithium oxides density. The electrode capacity can be estimated by the amount of lithium oxides which can be accommodate in large pores. They conclude that there is a linear relationship between average pore diameter and capacity. Hence, larger pores are more able to accommodate reaction products.

Ma *et al.*⁵⁵ found that carbon pore volume has more impact than the surface area of the

electrode. They also noticed that mesopores drive a higher discharge capacity and a better pore utilization, which enhances the performance to accommodate lithium oxides products. Alongside this, the electrode completely soaked with electrolyte presented a linear discharge profile, the absence of a potential plateau characterized by Li_2O_2 formation suggest a higher supply of oxygen to the electrode pores.

Furthermore, Jung *et al.*⁵⁶ claim that mesopore accessibility enhances Li_2O_2 deposition during battery operation. They claim that it is crucial to incorporate abundant mesopores in electrode design, ranging from 2-50 nm in size, in order to improve the electrochemical performance of Li-air batteries.

Along with those variables, the addition of catalysts may enhance battery performance. The main objectives of catalysts is the reduction of the overpotential between ORR/OER cycle and improve the solid Li_2O_2 decomposition during charge¹⁷.

Based on this brief literature analysis, it is evident that a careful selection of cathode material and morphology is necessary to enable larger round-trip cycle and charge rates for lithium-air battery operation.

2.2 Molecular Dynamics Simulation

A molecular dynamics simulation (MD) is the name given to describe the computation solution of Newton's equations of motion of a set of molecules⁵⁷. MD is based on the computation of equilibrium and transport properties of many-body systems⁵⁸. A basic MD code simulation can be constructed with following steps:

1. The definition of parameters that specify the simulation conditions (such as temperature, number of particles, density, time step and etc.)
2. The initialization of the system with construction of an initial configuration assigning positions to the particles.
3. The computation of the net forces on each particle.
4. The integration of Newton's equation of motion.
5. The steps 3 and 4 are the central part of the code. Repeat them until the simulation length is reached.
6. After finish the core loop compute/save and save simulation data including velocity, position, temperature, volume, stress tensors etc.
7. Run post-processing codes to calculate dynamic and structural properties.

More details on the creation of these codes and mathematical basis can be found in Frenkel and Smit⁵⁸, Allen and Tildesley⁵⁷, and McQuarrie⁵⁹.

Computer simulations are useful tools to provide microscopic information about a system, such as atoms interaction, molecular geometry, etc. Using molecular data it is possible to calculate macroscopic properties like transport coefficients, structural order parameters etc. A computational approach is extremely important, for instance at extremes temperature and pressures conditions where experimentation struggles⁵⁷. MD can also be a valuable tool when the objective is understanding phenomena at preliminary stages or/and when a experimental approach suffers with the complexity of the variables.

The MD simulation has a complementary place in lithium-air battery area. Once the phenomena behind this system is quite complex as previous discussed in Section 2.1. Thus, experimental approach is unable to capture the individual impact of each variable such as solvent, lithium salt, electrode or catalyst during system operation. Even applying *in-situ* and *in-operando* techniques is hard to define individual contributions to products formation and decomposition during battery operation. In this scenario the molecular findings provided by different simulation techniques are important to complement the results obtained by experimentalists. The flexibility of the simulation gives the opportunity to study in details the impact of materials selection as well as to provide data of molecular structures of Li⁺ solvation which are crucial for the understanding of reaction mechanisms.

2.2.1 Transport properties calculation

Transport properties are measures of mass, momentum, heat or charge flux of a given component. Simulation methods to compute transport properties can be categorized as equilibrium molecular dynamics (EMD) or nonequilibrium molecular dynamics (NEMD). EMD relies on post-processing results of standard MD simulation trajectories based on spontaneous fluctuations of the properties of a fluid. Whereas NEMD is based on the response of the system when subjected to a perturbing field, as for instance: force, electricity etc. This method requires the modification of force/motion equations and/or boundary conditions^{60,61}. Figure 2.4 illustrates: (a) an equilibrium MD simulation, (b) and (c) some types of shear stress perturbations to calculate viscosity by NEMD, and (d) modification of boundary condition to create temperature flux to calculate thermal conductivity coefficient by NEMD.

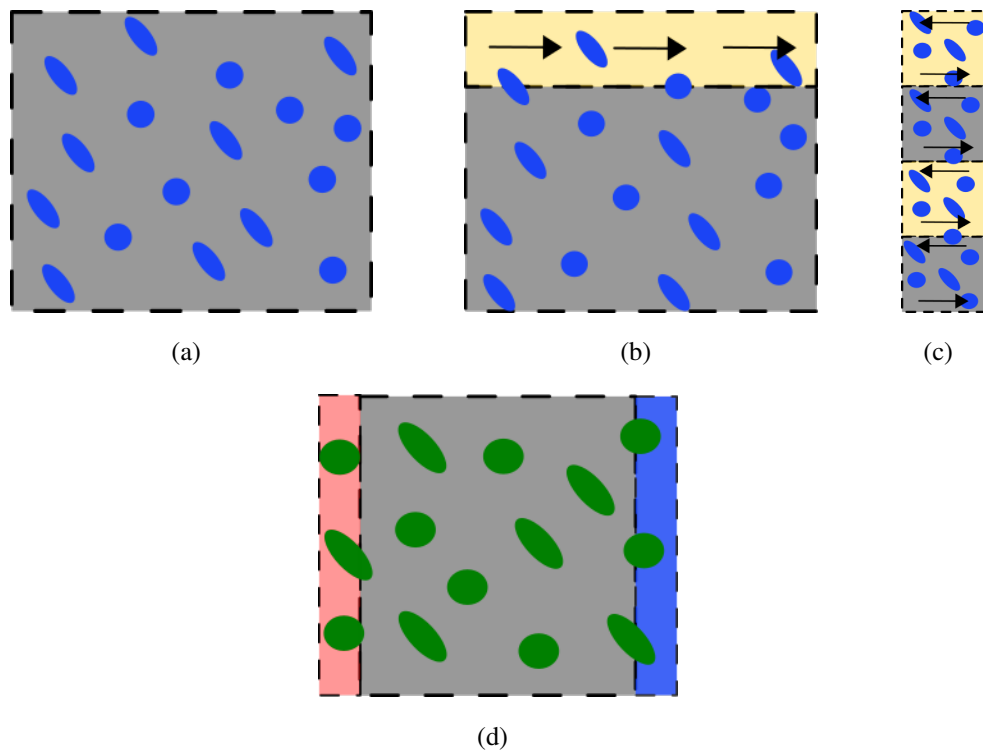


Figure 2.4: Examples of systems which simulate: (a) EMD, (b) NEMD with direct shear flow perturbation, (c) NEMD with oscillatory shear flow perturbation, and (d) NEMD with heat flux perturbation (red - hot side; blue - cold side).

EMD methods are based on the calculation of equilibrium time correlation functions (known as Green-Kubo (GK) relations) or on measuring the accumulated displacements over time (called Einstein-Helfand (EH) relations). The advantage of this technique is that multiple properties can be calculated using a single simulation, while for NEMD each property requires a unique simulation. However, high viscosity systems are difficult to compute using EMD, while NEMD methods have often show better performance⁶¹. Systems with high viscosity tend to be hard to compute using EMD because of the slow fluctuation in equilibrium.

In this work we evaluate transport properties of a DMSO solvent-based electrolyte. Because of its low viscosity and the computational cost of multiple simulations to calculate different properties, the EMD was adopted. Thus, this literature review will be focus on EMD methods.

The conventional way to compute transport properties from EMD simulations is the calculation of them as a secondary step, using Equations 2.15 or 2.16, known as the Green-Kubo (GK) and the Einstein-Helfand (EH) relations, respectively.

$$\gamma = \int_0^{\infty} \langle \dot{\xi}(t) \dot{\xi}(0) \rangle dt \quad (2.15)$$

where γ is the transport coefficient, $\dot{\xi}(t)$ is the variable used to the particular transport

property being calculated, and where the dot represents a time derivative. An integrated form of Equation 2.15 results in an equivalent expression for γ known as the Einstein equation for self-diffusion. Helfand⁶² developed a similar method for viscosity. Thus those relations are known as Einstein-Helfand and have the structure as follows:

$$\gamma = \lim_{t \rightarrow \infty} \frac{\langle [\xi(t) - \xi(0)]^2 \rangle}{2t} = \frac{1}{2} \lim_{t \rightarrow \infty} \frac{d}{dt} \langle [\xi(t) - \xi(0)]^2 \rangle \quad (2.16)$$

According to Frenkel and Smit⁵⁸, in an EMD simulation the Green-Kubo and the Einstein-Helfand methods are rigorously equivalent. Maginn *et al.*⁶¹ also claim that both methods theoretically give the same value. However there are some practical reasons to chose one or the other. The Green-Kubo and Einstein-Helfand methods have equivalent computational costs, however a specific set-up for data acquisition is required. Good reproducibility for these methods requires a custom sampling technique⁶¹. For example, calculating self-diffusion coefficient using the Einstein-Helfand method, it is necessary to run long trajectories to achieve reasonable averages, however it requires less data, once they should be sampled less frequently to capture the system behavior. In contrast, the Green-Kubo method requires shorter trajectories but with more frequent sampling because of the fast decay in time correlation function.

Ma *et al.*⁶³ evaluated the GK and the EH approaches for calculations of self-diffusivity, ionic conductivity and shear viscosity of 1-n-butylpyridinium tetrafluoroborate ionic liquid. Both methods were able to predict self-diffusion coefficient and ionic conductivity in close agreement with experimental data. However, both methods equally underestimated shear viscosity from literature, suggesting that the nonequilibrium molecular dynamics technique would be a better fit to calculate viscosity in this scenario.

Lee and Kim⁶⁴ compared the GK and EH approaches to calculate water self-diffusion coefficient using different force fields. Their findings show that both methods leads to roughly equivalent results with excellent agreement to experimental data.

Several open-source codes are available for port-processing EMD simulations, TRAVIS⁶⁵, MDAnalysis⁶⁶, MDTraj⁶⁷, and PyLAT⁶⁸ are some examples. All codes developed in this doctoral thesis are available to use (Appendix B). Alongside with the input files to run the EMD simulation using LAMMPS (Appendix A). Note that these codes should not be used as a “black box”, a careful EMD simulation set up and data analysis are crucial to ensure meaningful predictions⁶¹. More details about "best practices" to simulate and to calculate self-diffusion and viscosity coefficients can be found at Maginn *et al.*⁶¹.

2.2.2 Electrified electrolyte/electrode interface simulation

The method for simulating an electrolyte/electrode interface with the addition of an electric field at the electrode is addressed in the literature as: the Fixed Charge Method (FCM)

or the Constant Potential Method (CPM). Both methods are widely used in MD simulation of electrochemical systems. There are practical reasons to use each of them based on the specifics of the system and on the computational cost.

In the FCM technique a small fixed charge is added to each atom of the electrode layer that is in contact with the electrolyte forming a surface charge density. The charge is balance being one side negative and other positive. At the CPM method the electrode charges are allowed to fluctuate proportionally to both the local environment interface structure and the imposed electrostatic potential⁶⁹⁻⁷¹.

Some studies compared both approaches to verify their ability of mimicking a real device operation. Merlet *et al.*⁷² simulated 1-butyl-3-methylimidazolium hexafluorophosphate (BMIM-PF₆) ionic liquid electrolyte and graphite electrodes. They observed a small difference between the density profiles of cations and anions at positive and negative electrodes. CPM produced a more pronounced intercalation of cation/anion layers close to electrodes were noticed. However, the charge variation obtained using both approaches resulted in similar values for differential capacitance. They concluded that CPM leads to a better description of the system behavior, since FCM may underestimate electrolyte interaction with charged electrodes. The charge constrained in FCM limits the electrolyte to adopt a certain structure.

Wang *et al.*⁷⁰ simulated an electric double-layer capacitor composed of LiClO₄ in acetonitrile/graphite using static charge (FCM) and fluctuation potential (CPM). The authors concluded that there was no significant difference between the approaches can be observed at low potentials. However, at high charges the Li⁺ solvation structure was affected by local potential using CPM approach. Li⁺ was partially solvated on the electrode when applying small charges compared with those where this phenomena was observed using FCM. Based on the overall behavior of the electrolyte structure close to charged electrodes they claim that the CPM is more robust to perform double layer capacitors simulation.

According to Vatamanu *et al.*⁷¹ the FCM leads to good results on simulation of flat electrodes. However, when the shape consists of complex morphologies the CPM may be a better option as the double-layer behavior in this scenario is significantly depended on local environment. Thus, Vatamanu and co-workers^{71,73-75} have developed extensively research on the impact of roughness, electrical potential, electrolyte force field (polarizable versus classical) and composition using CPM approach to simulate electrolyte/electrode interface. A general conclusion is that CPM provides good description of system behavior. Alongside the adoption of polarizable force fields enhances the predictions of double layer capacitance and ions concentrations profiles. Comparison between electrode flat and rough surfaces shows that electrical double-layer shape may differ according to electrode type, leading to conclusion that flat models may be limited to describe experimental behavior.

Although CPM is more precise when simulating interface behavior under electrical

charge, the computational cost associated with its simulation is relatively high. Moreover experiments are typically run at low potentials which enables the use of FCM to simulate this type of systems⁷⁶.

FCM was used to study systems including ionic liquid and water doped with ions confined in electrodes plates under electrical charge⁷⁶⁻⁷⁸. This method was able to represent the system composed by water and ions (Na^+ , Cl^- , OH^- , H_3O^+), since it shows similar findings compared to other simulation models. Also Fang *et al.*⁷⁶ reported good results for electrical double layer capacitance and density profile in ionic liquids systems when in presence of charged electrodes.

One problem of FCM is the failure to describe rough electrodes/electrolyte interface under electrical charge. Zhang *et al.*⁷⁹ have performed MD simulations and experiments in order to better comprehend the double layer formation in decorated electrodes with functional groups. The authors concluded that simulation findings presented correspondence with experimental measurements and both methods were complementary to a better understanding of double-layer formation and dynamic. This corroborates the idea that the FCM approach is robust enough to capture electrochemical interface behavior of even complex electrodes.

This brief literature review evidenced that the CPM is the best method to simulate electrolyte/electrode interface when subjected to an electrical potential, however the computational cost imposes an obstacle to its utilization. In this context the FCM appears to be a suitable option to represent similar systems such as batteries without a high computational cost.

LAMMPS implementation of interface simulation using FCM is presented in Appendix C, alongside with codes to process data from simulation.

Chapter 3

Impact of anion shape on Li^+ solvation and on transport properties for lithium-air batteries: a molecular dynamics study[†]

Juliane Fiates^{a,b}, Yong Zhang^b, Luís F. M. Franco^a, Edward J. Maginn^b and Gustavo Doubek^a

^a *School of Chemical Engineering,
University of Campinas,
Campinas 13083-852, Brazil.*

^b *Department of Chemical and Biomolecular Engineering,
University of Notre Dame,
Notre Dame, Indiana 46556, USA.*

3.1 Abstract

Lithium-air batteries emerge as an interesting alternative for advanced energy storage devices. The complexity of such systems imposes great challenges. One of them resides in the selection of the pair lithium salt/solvent. Many electrolyte properties affect the operation of the batteries. Among these, transport properties and structural features have a special place. *Via* molecular dynamics simulations, we have calculated solution viscosity, ionic diffusivities and conductivities, as well as structural information, for two different salts in dimethyl sulfoxide (DMSO): lithium hexafluorophosphate - LiPF_6 , and lithium pyrrolide - LiPyr , at different temperatures and salt molalities. We show that, despite similar ionic transport properties, Li^+

[†]It have already been published at Physical Chemistry Chemical Physics Journal (PCCP). DOI:<https://doi.org/10.1039/D0CP00853B>. Reproduced by permission of the PCCP Owner Societies.

solvation in the different salts is significantly different. Therefore, solutions with different solvation properties, which impact the overall battery performance, might present analogous ionic dynamics.

3.2 Introduction

Metal-air batteries are getting increasing attention for the position they can occupy as one of the most relevant energy storage devices in the future. When compared to the traditional Li-Ion, metal-air batteries can achieve up to 10 times higher energy density⁴. The complexity in designing and operating such devices, however, presents considerable challenges⁴⁷.

Among all possible metal anodes of a metal-air battery, lithium has always been contemplated as a good candidate⁸⁰. Due to its high reactivity in aqueous solution, an aprotic electrolyte is preferred⁸¹. The aprotic Li-O₂ battery, composed of a lithium anode and a porous oxygen cathode, basically consists of lithium peroxide (Li₂O₂) reactions of formation and decomposition¹⁸. The electrolyte plays a crucial role in the system performance, as it constitutes the medium for reactants transport between cathode and anode during the charge and discharge processes⁸². Therefore, a deep understanding of the ionic transport properties, such as ionic conductivity, diffusivity, and viscosity, in a certain electrolyte, is necessary for an optimum electrolyte selection. Moreover, an ideal electrolyte for lithium-oxygen batteries should have high lithium ion conductivity, but also low volatility, and high oxygen solubility^{17,47}.

DMSO (dimethyl sulfoxide) emerges as a solvent able to fulfill those features. Having a high donor number, DMSO has favorable interactions with cations⁸³. The lithium salt, however, can also have an impact on the electrolyte stability⁸⁴. Even being extensively used in commercial Li-ion batteries, LiPF₆ has several limitations such as chemical and thermal instability. Therefore, the anion selection opens the possibility to tune electrochemical systems^{84,85}.

To characterize the electrolyte behavior, and its transport properties, analysis of transference number and solvation distribution should be used⁸⁴. The solvation shell analysis is extremely important to understand the complex formation between cation, anion, and solvent, making possible the determination of the amount of "free" Li⁺, which has a direct relation with Li-reactions^{83,86}.

Kirshnamoorthy *et al.*⁸⁷ have studied the impact of two anions (TFSI⁻ (bis(trifluoromethane)sulfonimide) and BF₄⁻ (tetrafluoroborate)) on the transport and structural properties of adiponitrile solutions. The authors have observed similar Li⁺ solvation with both anions. The transport properties, however, have shown completely different behavior, which was justified by the solvation shell around the anions.

Burke *et al.*¹⁸ evaluated the relation between anions and the reaction pathway for Li-

air batteries. The authors concluded that the anion donor number impacts the solubility of the intermediate products. This solubility is related to Li^+ solvation, showing that high donor number anions can enhance the battery capacity and rechargeability. These results also depend on the solvent choice. For high donor number solvents, such as DMSO, this effect is less pronounced. The oxygen mobility in high donor number solvents is totally independent of the anion⁴⁷. Despite this, larger anions increase the availability of oxygen, which impacts the reactions; the superoxide intermediate may become less stable because of the large solvation structure caused by superoxide-anion coordination⁴⁷. The synergy between anion concentration and O_2 solubility in DMSO was observed by Lindberg *et al.*¹⁹. Experimental measurements of TFSI⁻ showed that increasing its concentration increases the solubility of O_2 . Nevertheless, higher concentrations of ClO_4^- (perchlorate) and Tf^- (trifluoromethanesulfonate) leads to lower O_2 solubility.

The relation between Li^+ and anion has been also reported in some studies based on molecular simulations. The pair interaction between Li^+ and PF_6^- in propylene carbonate is weaker than between Li^+ and BF_4^- . The interaction also impacts viscosity, which achieves higher values in LiBF_4 solution at higher concentrations, corroborating the connected mobility of cation and anion¹¹. Jones *et al.*²⁸ have investigated LiBF_4 in propylene carbonate/ethylene carbonate. The cation is solvated by propylene carbonate, and the anion by ethylene carbonate. At high salt concentration, the mobility of Li^+ and BF_4^- remains uncorrelated.

In the present study, we seek to investigate, through molecular dynamics simulations, if it is possible to relate the ionic transport properties and the structural aspects of the ionic solvation. We have chosen to study two different lithium salts in DMSO solutions: LiPF_6 and LiPyr . The literature with experimental data for thermophysical properties of DMSO solutions containing LiPF_6 or LiPyr , varying temperature and salt molality values, is rather scarce. Aminabhavi and Gopalakrishna⁸⁸ have experimentally measured density and viscosity of pure DMSO at 25°C as $1096 \text{ kg}\cdot\text{m}^{-3}$ and $1.948 \text{ mPa}\cdot\text{s}$, respectively. Lindberg *et al.*¹⁹ have found a value of $2.14 \text{ mPa}\cdot\text{s}$ for the viscosity of pure DMSO at 22°C. For 0.1 M LiPF_6 in DMSO, Laoire *et al.*²⁰ reported an ionic conductivity of $0.211 \text{ S}\cdot\text{m}^{-1}$. Recently, Elabyouki *et al.*⁸⁹ have calculated, using molecular dynamics simulations, the transport properties of 1.5 M LiPF_6 in DMSO in a hierarchical carbon electrode. They have calculated the Li^+ and the PF_6^- diffusion coefficients in the confinement direction. The values of diffusion coefficients in confinement media are known to be different than the unconfined values^{90,91}.

Electrolyte selection is a critical step for an optimum design of a lithium-air battery. We hope that testing the hypothesis of a possible relation between ionic transport and solution structure might help elucidate how these properties can guide a rational electrolyte selection.

3.3 Computational details

3.3.1 Force fields

The chosen force fields are based on a sum of Lennard-Jones (LJ) and Coulombic potentials for nonbonded interactions. Equation 3.1 shows the total potential energy functional form, adding the bonded interactions:

$$\begin{aligned}
 U_{\text{total}} = & \sum_{\text{bonds}} k_b (b - b_0)^2 + \sum_{\text{angles}} k_\theta (\theta - \theta_0)^2 \\
 & + \sum_{\text{dihedrals}} k_\phi [1 + \cos(n\phi - \delta)] \\
 & + \sum_{\text{improper}} k_\psi [1 + \cos(n\psi - \delta)] \\
 & + \sum_{i>j} \left\{ \frac{q_i q_j}{4\pi\epsilon_0 r_{ij}} + 4\epsilon_{ij} \left[\left(\frac{\sigma_{ij}}{r_{ij}} \right)^{12} - \left(\frac{\sigma_{ij}}{r_{ij}} \right)^6 \right] \right\} \quad (3.1)
 \end{aligned}$$

where the total energy is expressed in terms of bond length, b , bond angle, θ , dihedral torsion angle, ϕ , and improper dihedral torsion angle, ψ ; k is the constant related to each type of intramolecular force, q is the atomic charge related to the Coulombic electrostatic interactions, ϵ_0 is the vacuum permittivity, σ_{ij} and ϵ_{ij} are LJ potential parameters. Crossed LJ parameters were obtained applying Lorentz-Berthelot combining rules.

Atomistic representations of DMSO, Li^+ , PF_6^- , and Pyr^- , are shown in Figure 4.1. The parameters used to simulate dimethyl sulfoxide (DMSO) were taken from a flexible all-atom model developed by Strader and Feller⁹². For LiPF_6 , bond parameters of PF_6^- were taken from Kumar and Seminario⁸, and nonbond parameters from Jorn *et al.*⁹³. For LiPyr , both bond and nonbond parameters were taken from Liu and Maginn⁹⁴.

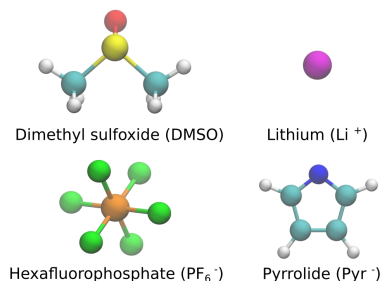


Figure 3.1: All-atom representations of DMSO, Li^+ , PF_6^- , and Pyr^- . Color code: oxygen (red), sulfur (yellow), carbon: (cyan), hydrogen: (white), lithium (magenta), phosphorus (orange), fluorine (green), and nitrogen (blue).

3.3.2 Molecular dynamics simulations

The initial configurations were assembled in a cubic box using the Packmol⁹⁵ package. We investigated four molalities: [0.25, 0.50, 0.75, 1.00] mol·kg⁻¹ for both systems. The number of particles were fixed as $N_{\text{cation}} = N_{\text{anion}}/N_{\text{DMSO}}$: [40/2047, 40/1023, 40/682, 40/512], respectively. The same system size was applied to LiPF₆ and LiPyr in DMSO solutions.

All simulations were performed using LAMMPS²⁹. The equilibration was carried out in the isothermal-isobaric ensemble (NPT) for 2 ns, followed by a production stage in the canonical ensemble (NVT) (for equilibration purposes 1 ns of NVT was run and ignored before the production starts). A Nosé-Hoover thermostat^{96,97} and Parrinello-Rahman barostat⁹⁸ were employed. Electrostatic interactions were computed using the particle-particle particle-mesh scheme (PPPM)⁹⁹. For Lennard-Jones interactions, long-range corrections for energy and pressure were applied beyond a cutoff radius of 12 Å. Periodic boundary conditions were applied in all directions.

The production runs were carried out for 10 ns for the viscosity calculations, and 1 ns for diffusivity and conductivity calculations. Thermodynamic properties, and trajectories, were stored every 5 fs. The simulation length and recording times were selected based on literature recommendations^{61,100} and preliminary tests. Radial distribution functions were obtained from the RDF subroutine implemented in LAMMPS. Densities were extracted directly from LAMMPS, as averages of NPT runs after 1.5 ns of equilibration. The standard deviations were evaluated considering 30 independent trajectories. More details can be found in an example input file provided in the supplementary material.

3.3.3 Transport properties calculation

Shear viscosities were calculated with the following Green-Kubo relation^{101,102}:

$$\eta = \frac{V}{k_B T} \int_0^{+\infty} \langle P_{\alpha\beta}(t_0 + t) \cdot P_{\alpha\beta}(t_0) \rangle dt \quad (3.2)$$

where η is the shear viscosity, V is the system volume, k_B is the Boltzmann constant, T is the absolute temperature, $P_{\alpha\beta}$ is an independent component of the pressure tensor, and t is time. To improve the statistics of the calculation, additional independent components of the pressure tensor were used¹⁰³ $(P_{xx} - P_{yy})/2$, $(P_{yy} - P_{zz})/2$, and $(P_{xx} - P_{zz})/2$.

Due to the large statistical uncertainty in viscosity calculation, the time decomposition method¹⁰⁰ was implemented. Using different velocity seeds, 30 independent trajectories were generated for each temperature and molality. The viscosity was then calculated using Equation 3.2. The averaged viscosity over the 30 trajectories was fitted to an empirical expression (Eq.

3.3^{104,105}) using a weighting function ($1/t_b$) up to a cutoff point.

$$\eta(t) = A\alpha\tau_1 (1 - e^{-t/\tau_1}) + A(1 - \alpha)\tau_2 (1 - e^{-t/\tau_2}) \quad (3.3)$$

where $\eta(t)$ is the shear viscosity, A , α , τ_1 , and τ_2 are fitting parameters. The cutoff point was established as the point for which the standard deviation of the average viscosity ($\sigma_{sd}(t)$ - Eq. 3.4) equals 40% of the viscosity value ($\langle\eta(t)\rangle$)¹⁰⁰. In Equation 3.4, m is the number of trajectories:

$$\sigma_{sd}(t) = \sqrt{\frac{1}{m-1} \sum_{i=1}^m (\eta(t)_i - \langle\eta(t)\rangle)^2} \quad (3.4)$$

The weighting parameter b was obtained fitting the standard deviation to a power law function, as shown in Equation 3.5¹⁰⁰.

$$\sigma_{sd}(t) = Ct^b \quad (3.5)$$

where $\sigma_{sd}(t)$ is the standard deviation and C and b are fitting parameters.

The error was estimated as^{104,105}:

$$\Delta\eta = \sqrt{\frac{2A[\alpha\tau_1 + (1-\alpha)\tau_2]}{t_{\max}}} \quad (3.6)$$

where t_{\max} is the maximum decay time.

Self-diffusion coefficients were calculated using a Green-Kubo relation, which is completely analogous to the Einstein-Smoluchowski approach⁵⁸. Equation 3.6 shows the Green-Kubo relation for self-diffusion coefficient calculation as the time integral of the velocity autocorrelation function (VACF)^{101,102}.

$$D_i = \frac{1}{3N_i} \int_0^{+\infty} \sum_{k=1}^{N_i} \langle \mathbf{v}_k(t_0+t) \cdot \mathbf{v}_k(t_0) \rangle dt \quad (3.7)$$

where D_i is the diffusion coefficient of ionic species i , N_i is the total number of ions i , the angle brackets represent the ensemble average of the velocity correlation over all time origins, and \mathbf{v}_k is the velocity of ion k .

As for viscosity, the diffusivity calculation is also subjected to statistical estimation uncertainty^{61,105}. Thus, ten independent trajectories were used, and the averaged diffusivity was fitted to an exponential function:

$$D(t) = D + a \exp(-bt) \quad (3.8)$$

where D , a , and b are fitting parameters. The standard deviation was obtained from the average of all trajectories. The diffusion is highly affected by the system size^{58,61,106}. Therefore, we

applied in our calculations a correction for system-size effects as follows^{106–108}:

$$D_{\infty} = D_{\text{PBC}} + \frac{2.837297k_B T}{6\pi\eta L} \quad (3.9)$$

where D_{∞} is the diffusion coefficient in an infinite system, D_{PBC} is the diffusion coefficient calculated using periodic boundary condition, and L is the cubic box length.

The ionic conductivity was calculated by the electrical current autocorrelation function as¹⁰⁵:

$$\sigma = \frac{1}{3k_B T V} \int_0^{+\infty} \langle \mathbf{J}(t_0 + t) \cdot \mathbf{J}(t_0) \rangle dt \quad (3.10)$$

where σ is the ionic conductivity, and the electrical current, \mathbf{J} , is obtained by the product between the ionic charge, q_i , and its velocity, \mathbf{v}_i , computed over all the N molecules:

$$\mathbf{J} = \sum_{i=1}^N q_i \mathbf{v}_i \quad (3.11)$$

In the conductivity calculation, the same number of trajectories, and the same fitting procedure described for the diffusivity calculation, were adopted.

3.4 Results and discussion

3.4.1 Density

Figure 4.2 shows the solution density of LiPF_6 and LiPyr in DMSO at 298 K and 1 atm as a function of salt molality. The effect of the salt molality on the solution density is more pronounced for LiPF_6 in DMSO. Since Pyr^- is planar and PF_6^- is spherical, the structural arrangement in each system is different (as shown later in Figs 4.9 and 3.10), which has impacts on the total volume. Also, the mass of PF_6^- is almost twice the mass of Pyr^- . Therefore, the increment in the number of PF_6^- ions has a larger effect on the solution density.

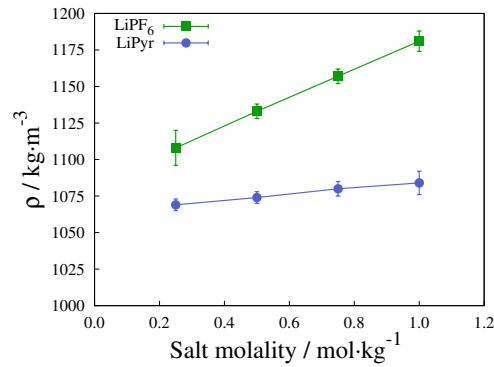


Figure 3.2: Density of LiPF₆ and LiPyr in DMSO solutions as a function of salt molality at 298 K and 1 atm.

The temperature dependence of the density for 1 mol·kg⁻¹ solutions is shown in Table 4.1. As temperature increases, the density slightly decreases for both systems. The thermal expansion coefficient was calculated from its definition^{7,109}:

$$\alpha_P = -\frac{1}{\rho} \left(\frac{\partial \rho}{\partial T} \right)_P \quad (3.12)$$

Both systems have a positive thermal expansion coefficient at these conditions: $8.60 \times 10^{-4} \text{ K}^{-1}$ for LiPF₆, and $9.97 \times 10^{-4} \text{ K}^{-1}$ for LiPyr. Densities of pure DMSO are shown in Figure 4.3. The simulations slightly underestimate the density of pure DMSO. The calculated thermal expansion coefficient at 298 K is $8.60 \times 10^{-4} \text{ K}^{-1}$ and, the experimental value reported in the literature⁷ is $9.13 \times 10^{-4} \text{ K}^{-1}$.

Table 3.1: Density of 1 mol·kg⁻¹ LiPF₆ in DMSO solution, and of 1 mol·kg⁻¹ LiPyr in DMSO solution, as a function of temperature at 1 atm.

Temperature / K	Density / kg·m ⁻³	
	LiPF ₆ in DMSO	LiPyr in DMSO
298	1181 ± 7	1084 ± 8
330	1147 ± 7	1051 ± 7
360	1118 ± 7	1017 ± 8

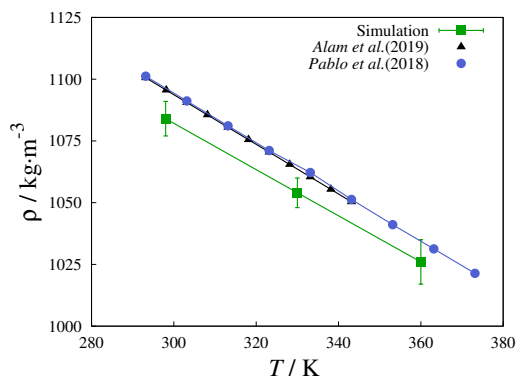


Figure 3.3: Density of pure DMSO as a function of temperature at 1 atm. Experimental measurements were taken from literature^{6,7}.

3.4.2 Transport properties

Figure 4.4 shows the shear viscosity at 1 atm of LiPF_6 and LiPyr in DMSO as a function of salt molality at 298 K and as a function of temperature at a molality of $1 \text{ mol}\cdot\text{kg}^{-1}$ (Figure S1 presents the fitting of shear viscosity for both systems at $1 \text{ mol}\cdot\text{kg}^{-1}$ and 298 K). The shear viscosity increases with salt molality for both salts. A similar behavior has been reported for LiBF_4 in propylene carbonate²⁸. As expected for liquids, the shear viscosity of the solution decreases with increasing temperature for both salts. Being consistently less viscous within the studied range of conditions, LiPyr in DMSO solutions present higher mobility than solutions of LiPF_6 in DMSO. The calculated viscosity values for pure DMSO are in excellent agreement with experimental data, suggesting that the force field for DMSO is adequate to represent the transport properties of such a system.

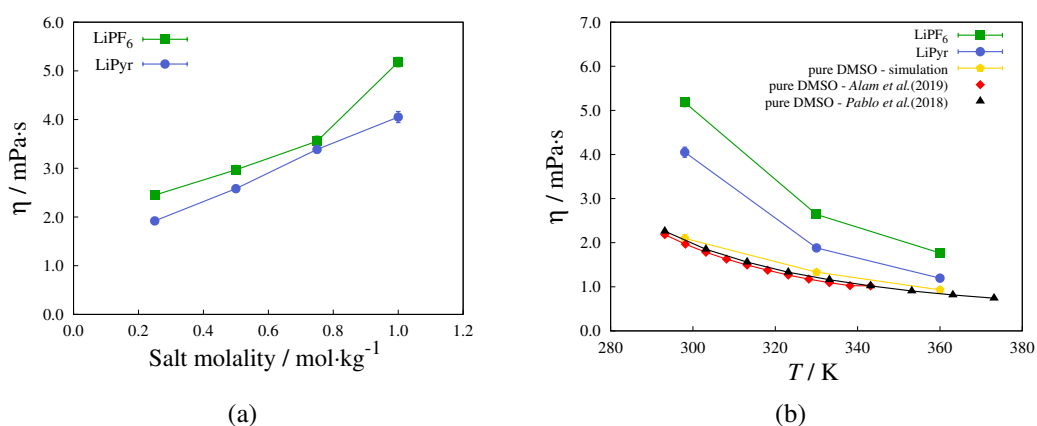


Figure 3.4: Shear viscosity of LiPF_6 and of LiPyr in DMSO solutions at 1 atm as a function of: (a) salt molality at 298 K, and (b) temperature for solutions with $1 \text{ mol}\cdot\text{kg}^{-1}$ (simulation and experimental^{6,7} values for pure DMSO are also shown for comparison purposes). Uncertainties are on the order of $\pm 0.1 \text{ mPa}\cdot\text{s}$ for all simulated results.

The ionic diffusion coefficients for Li^+ , PF_6^- , and Pyr^- in DMSO solutions are shown

in Figure 4.5 (Figure S2 presents the fitting of self-diffusion coefficients for cations and anion of both systems at $1 \text{ mol}\cdot\text{kg}^{-1}$ and 298 K). Diffusion coefficients decrease with increasing salt molality since more crowded systems have less available free space. This behavior has already been noticed in similar systems^{11,28}. On the other hand, diffusion coefficients increase with temperature since the probability of achieving higher velocities is enhanced at higher temperatures. A system size analysis over diffusivity can be found in Section 2 of ESI A.

Within the statistical uncertainty, the anions of both salts have essentially the same diffusion coefficients. Nevertheless, although Li^+ ions are much smaller than the anions, they have lower diffusion coefficients than the anions, and such coefficients remain unaffected by the anion type. Regarding the solvent, DMSO has higher mobility in composition with LiPyr (Fig. 4.5 (b)) agreeing with the viscosity profile showed in Figure 4.4 (b). Moreover, a smaller presence of DMSO in Li^+ solvation shell is observed for LiPyr (Fig. 3.10), which is probably enhancing DMSO mobility.

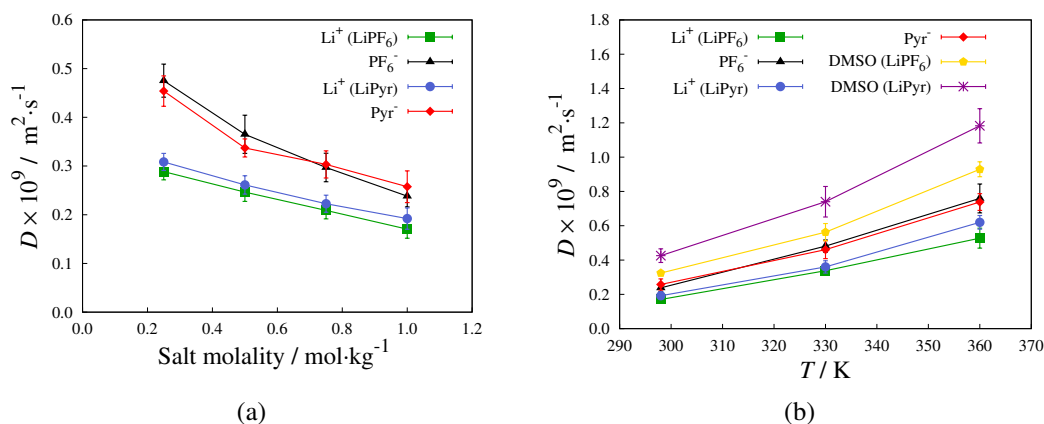


Figure 3.5: Self-diffusion coefficients of Li^+ and PF_6^- in DMSO solution of LiPF_6 , and of Li^+ and Pyr^- in DMSO solution of LiPyr , at 1 atm as a function of: (a) salt molality at 298 K, and (b) temperature for solutions with $1 \text{ mol}\cdot\text{kg}^{-1}$ (The self-diffusion coefficients of DMSO in the salt solutions are also shown). The error bars at the lowest temperature are smaller than the symbol size.

The effects of salt molality and temperature on the ionic conductivity of LiPF_6 and LiPyr in DMSO solutions are shown in Figure 4.6 (Figure S3 illustrates the fitting of conductivity for both systems at $1 \text{ mol}\cdot\text{kg}^{-1}$ and 298 K). A good agreement is observed with experimental data^{9,20} for LiPF_6 at molalities of 0.1 and $1.0 \text{ mol}\cdot\text{kg}^{-1}$ (Fig. 4.7(a)), indicating that the force field is able to capture the behavior of this system. A nonlinear increase of ionic conductivity with increasing salt molality is observed. A similar trend was experimentally observed for DMSO solutions of LiTFSI , LiClO_4 , and LiTf ¹⁹. The salt type seems to have a negligible effect on the computed ionic conductivities presented here, and this result corroborates what was experimentally observed for other lithium salts in DMSO solutions. As with the diffusion coefficients, the ionic conductivity values are higher for higher temperatures and independent of system size effect as shown in Section 2 of ESI A.

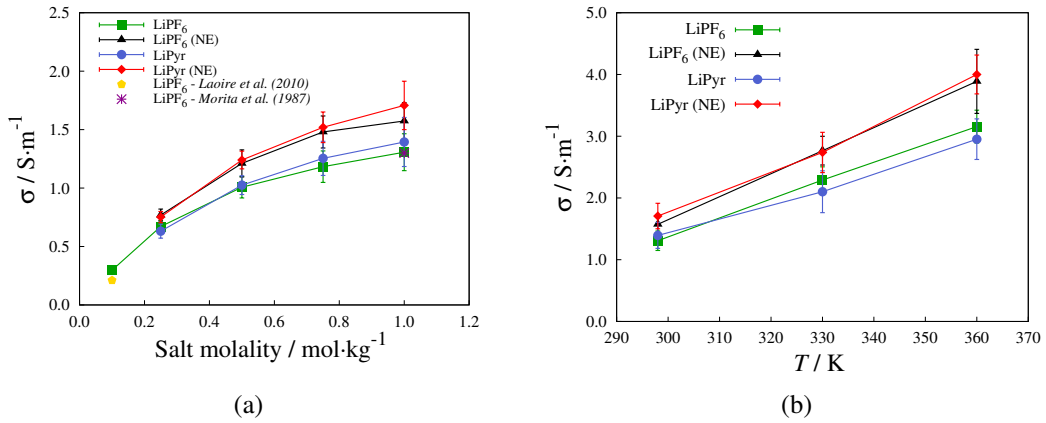


Figure 3.6: Ionic conductivity of LiPF_6 and LiPyr in DMSO solutions at 1 atm as a function of: (a) salt molality at 298 K (experimental data values for concentrations of $0.1 \text{ mol}\cdot\text{kg}^{-1}$ and $1 \text{ mol}\cdot\text{kg}^{-1}$ of LiPF_6 in DMSO are also presented), and (b) temperature for solutions with $1 \text{ mol}\cdot\text{kg}^{-1}$. Nernst-Einstein (NE) ionic conductivities are shown for comparison purposes. The uncertainties for NE ionic conductivities were propagated from the uncertainties of the corresponding diffusion coefficients. The error bars at the lowest temperature are smaller than the symbol size.

At infinite dilution, the ionic conductivity can be estimated from the Nernst-Einstein relation¹¹⁰:

$$\sigma_{\text{NE}} = \frac{1}{k_B T} \sum_{i=1}^N \rho_i q_i^2 D_i \quad (3.13)$$

where σ_{NE} is the Nernst-Einstein ionic conductivity, ρ_i is the number density of ion i , and D_i is the diffusion coefficient of ion i .

The relation between the ionic conductivity calculated by Green-Kubo approach and the Nernst-Einstein ionic conductivity can be expressed as:

$$\sigma = \sigma_{\text{NE}} (1 - \Delta) \quad (3.14)$$

where Δ is the Nernst-Einstein deviation parameter, which can be defined in terms of the time integral of the velocity cross-correlation function for unlike ions¹¹¹. Δ has been shown to be independent of temperature and pressure¹¹². Here, we calculated Δ for different salt molalities and temperatures, as presented in Figure 4.7, and the results show that Δ seems to be independent of salt molality, as well as of temperature at the studied range.

A relation between the limiting molar ionic conductivity and the viscosity was first proposed by Walden¹¹³. The Walden's rule states that the product between these two properties should be constant:

$$\Lambda \eta = \text{constant} \quad (3.15)$$

where Λ is the limiting molar ionic conductivity defined in terms of the Nernst-Einstein ionic

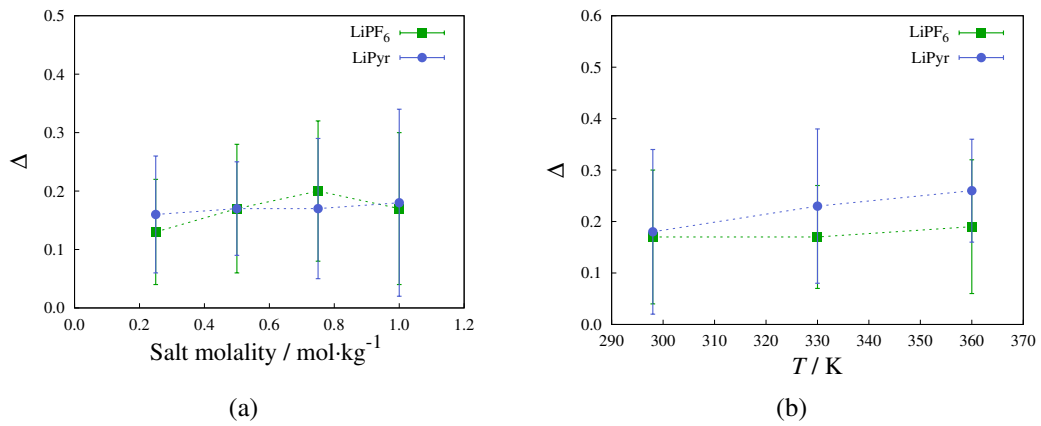


Figure 3.7: The Nernst-Einstein deviation parameter, Δ , for LiPF₆ and LiPyr in DMSO solutions at 1 atm as a function of: (a) salt molality at 298 K, and (b) temperature for solutions with 1 mol·kg⁻¹. The uncertainties were propagated from the uncertainties of the corresponding conduction coefficients.

conductivity for 1:1 electrolytes as:

$$\Lambda = \frac{\sigma_{\text{NE}}}{c} \quad (3.16)$$

where c is the electrolyte molar concentration.

This rule can be derived assuming the validity of Stokes-Einstein relation for the ionic diffusivity:

$$D_i = \frac{k_B T}{6\pi\eta r_i} \quad (3.17)$$

where r_i is the Stokes radius of ion i .

Substituting Equations (3.16) and (3.17) into Equation (3.15), one has that for a 1:1 electrolyte:

$$\Lambda\eta = \frac{e^2 N_A}{6\pi} \left[\frac{1}{r^+} + \frac{1}{r^-} \right] \quad (3.18)$$

where e is the elementary charge, N_A is the Avogadro's number, r^+ is the cation Stokes radius, and r^- is the anion Stokes radius.

Therefore, Walden's rule is satisfied provided Nernst-Einstein and Stokes-Einstein relations are valid.

Although the conclusions on ion-pairing and association exclusively obtained from a direct analysis of the so-called Walden plot ($\log \Lambda$ versus $\log \eta^{-1}$) have been vehemently criticized¹¹⁴ in the case of ionic liquids, especially when compared to the arbitrary reference of the ideal aqueous KCl line¹¹⁵, a simple observation of the Walden plot might help to classify different electrolytes in terms of the combination between the ionic conductivity and the solution viscosity.

Figure 4.8 presents the Walden plot for LiPF₆ and LiPyr in DMSO solutions,

calculated using both the ionic conductivity and the Nernst-Einstein ionic conductivity for different temperatures. As expected, the Nernst-Einstein deviation parameter is independent of temperature. Both solutions have similar transport properties and the only significant difference is in viscosity. DMSO solutions of LiPyr are less viscous, and therefore their data are shifted to the right in the Walden plot in comparison to DMSO solutions of LiPF₆.

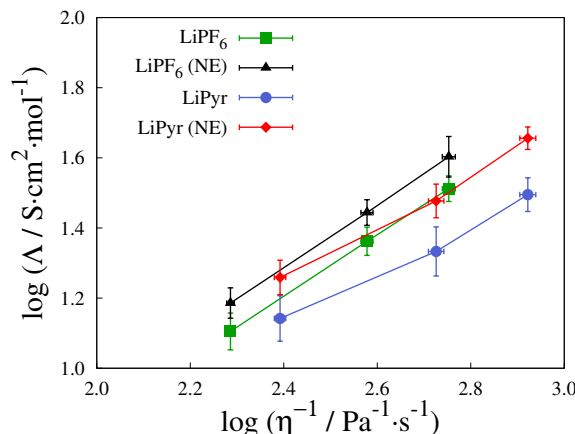


Figure 3.8: Walden plot for LiPF₆ and LiPyr in DMSO solutions, using both calculated ionic conductivity and the calculated Nernst-Einstein (NE) ionic conductivity for different temperatures. Some error bars cannot be seen because they are smaller than the symbol size. Note the different scales in X and Y-axes.

In terms of Walden's rule, the slope of the curves in the Walden plot should be 1. Some systems, however, exhibit a different behavior, which has been treated with the fractional Walden rule¹¹⁶:

$$\Lambda \eta^\alpha = \text{constant} \quad (3.19)$$

where α is the Stokes-Einstein exponent¹¹².

Using Nernst-Einstein ionic conductivities, we found that $\alpha = 0.89$ for DMSO solutions of LiPF₆, and $\alpha = 0.74$ for DMSO solutions of LiPyr. The experimentally determined value for α for an infinitely diluted aqueous KCl solution is 0.87¹¹⁵.

From the transport properties viewpoint, no significant difference between DMSO solutions of LiPF₆ and LiPyr was observed. These solutions differ only in viscosity and in Stokes-Einstein exponents. Despite the differences in shape and composition, the ionic transport seems to be independent of the anion type in the present case.

3.4.3 Structural arrangement

To examine the structural arrangement of the solvated ions in DMSO, the radial distribution function (RDF), and the corresponding coordination number, n , calculated by the running integral of the RDF, are analyzed.

Figures 4.9 and 3.10 present the radial distribution functions between Li^+ and the DMSO oxygens, as well as Li^+ and PF_6^- atoms (Fig. 4.9), and Li^+ with Pyr^- hydrogen and nitrogen atoms (Fig. 3.10), all systems with $1 \text{ mol}\cdot\text{kg}^{-1}$ at 298 K and 1 atm. To understand the influence of molality and temperature on the Li^+ coordination shell behavior, we have determined the first layer, which corresponds to the minimum after the first peak: being 2.35 \AA for O and F in PF_6^- , and 2.6 \AA and 3.0 \AA for O and N in Pyr^- , respectively. Figures S5 and S6 of ESI A present the RDF profiles for different molalities and temperatures for LiPF_6 and LiPyr , respectively. The inset plots of Figures 4.9 and 3.10 illustrate the shell configuration around Li^+ .

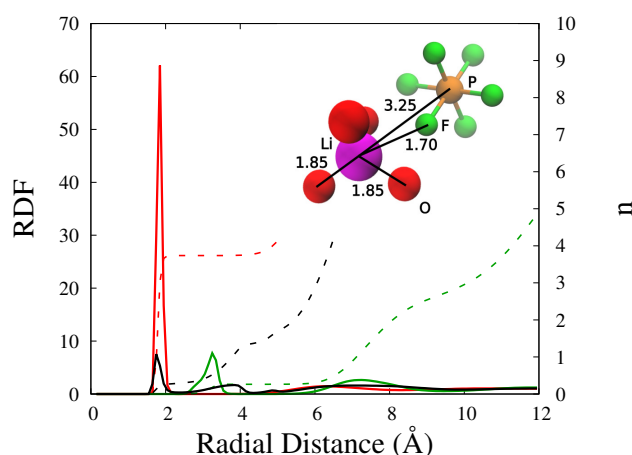


Figure 3.9: Radial distribution functions (RDF) (solid lines, left y axis), and coordination numbers (dashed lines, right y axis) for Li–O (DMSO) - red, Li–F(PF_6) - black, and Li–P(PF_6) - green at 298 K and 1 atm for $1.0 \text{ mol}\cdot\text{kg}^{-1}$ DMSO solution of LiPF_6 . The inset plot shows the solvation structure of Li^+ . The distances are in Angstrom. Atom color code: lithium (magenta), oxygen (red), phosphorus (orange), and fluorine (green).

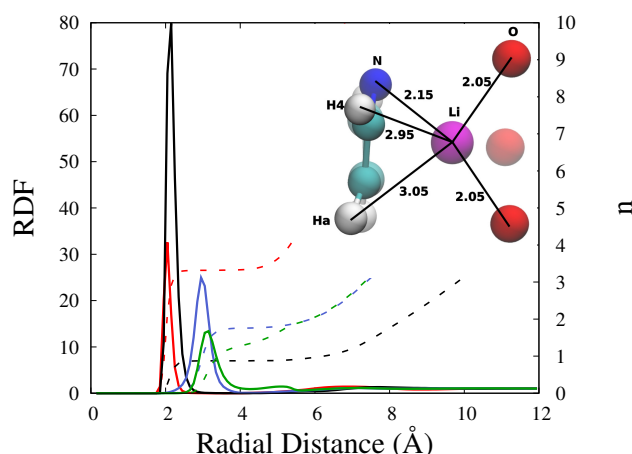


Figure 3.10: Radial distribution functions (RDF) (solid lines, left y axis), and coordination numbers (dashed lines, right y axis) for Li–O (DMSO) - red, Li–N(Pyr) - black, Li–H4(Pyr) - blue, and Li–Ha(Pyr) - green at 298 K and 1 atm for $1.0 \text{ mol}\cdot\text{kg}^{-1}$ DMSO solution of LiPyr . The inset plot shows the solvation structure of Li^+ . The distances are in Angstrom. Atom color code: lithium (magenta), oxygen (red), nitrogen (blue), carbon (cyan), and hydrogen (white).

Figure 3.11 (a) and (b) present the coordination number values as a function of molalities

and temperatures (Table S1 of ESI A presents more information on coordination numbers). Lithium ions are highly coordinated with four oxygens in DMSO solutions of LiPF_6 . This result is in agreement with the observation that lithium ion is solvated by four DMSO molecules forming $\text{Li}^+(\text{DMSO})_4\text{PF}_6^-$ ion pair^{117,118}. Yamada *et al.*¹⁰ have also shown, with Raman spectroscopy, the $\text{Li}^+(\text{DMSO})_4$ coordination in $1 \text{ mol}\cdot\text{kg}^{-1}$ solution, as can be seen in 3.11 (a). The preferential solvation of Li^+ by DMSO, even in acetonitrile-DMSO mixtures with low DMSO mole fractions, has been observed by experimental measurements of ionic conductivity¹¹⁹. Li^+ solvation in DMSO remains constant with increasing salt molality, and an analogous behavior is observed for the influence of temperature.

A different arrangement is found for LiPyr in DMSO solution. As shown in Figure 3.10, lithium ions are much more correlated with the anions. The values of coordination (Fig. 3.11 (a)) reveal higher ion pairing increasing with salt molality. In contrast, the number of DMSO solvating Li^+ decreases at high molalities. A persistent presence of ion contact, even at low molalities of LiPyr in DMSO solutions, is observed.

The negative charge in PF_6^- is more delocalized in comparison with Pyr^- . In PF_6^- , the negative charge is distributed along all fluorine atoms, which weakens the electrostatic interaction between PF_6^- and Li^+ . The molecular arrangement of PF_6^- also contributes to its lower interaction with Li^+ . On the other hand, for Pyr^- the negative charge is positioned mostly at nitrogen and close hydrogens (H4 - Fig. S8 of ESI A), which facilitates the interaction between Li^+ and Pyr^- . At high molalities, the ions are much more packed, increasing the probability of interaction of Li^+ and Pyr^- by the electrostatic forces.

Regarding temperature, we found a slight increase in ion pairing and desolvation for Li^+ of LiPyr in DMSO solution at higher temperatures, as can be seen in Figure 3.11 (b). The opposite behavior happens for Li^+ of LiPF_6 in DMSO, where an increase of solvation decreasing ion pair interaction at higher temperatures is found.

Figure 3.11 (c) shows the probability distribution for the Li^+ solvation for DMSO oxygen and phosphorus from PF_6^- , as well as nitrogen from Pyr^- in solutions with $1.0 \text{ mol}\cdot\text{kg}^{-1}$ at 298 K. Figure S7 (a-e) of ESI A illustrates the environmental distribution for other molalities and at other temperatures. The average coordination profile is the most probable scenario of ion pair distribution, except for $0.25 \text{ mol}\cdot\text{kg}^{-1}$ at 298 K (Fig. S7 (a)), where the systems exhibits a higher probability of no ion pair coordination of Pyr^- with Li^+ , and a solvation shell composed by five DMSO molecules. For LiPF_6 in DMSO, a preference for the full solvation of Li^+ by four molecules of DMSO for all investigated molalities and temperatures is observed. This result highlights the tendency of Li^+ from LiPyr in DMSO to be partially coordinated by three DMSO molecules, and of keeping an ion pair coordination with the negative termini of Pyr , corroborating the theory of the impact of shape and charge distribution on the solvation sphere formation.

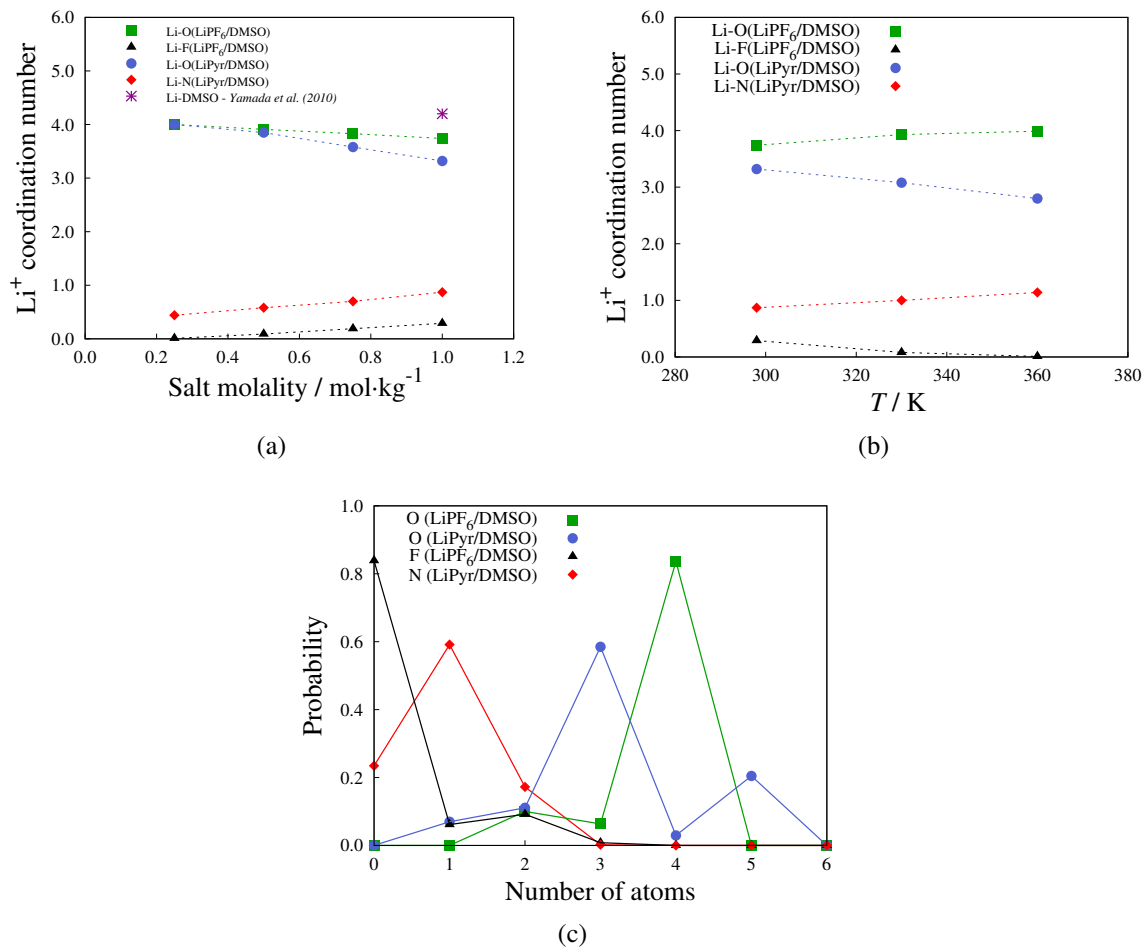


Figure 3.11: Solvation: (a) Li^+ coordination numbers for the first shell shown in Figures 4.9 and 3.10 as function of molality at 298 K (Experimental data taken from¹⁰ are also shown), and (b) as function of temperature for solutions with $1 \text{ mol}\cdot\text{kg}^{-1}$, (c) probability distribution of Li^+ coordination environment in the first solvation shell for O from DMSO, F from PF_6^- , and N for Pyr^- at $1 \text{ mol}\cdot\text{kg}^{-1}$ and 298 K.

Since we have different solvation structures for each system, a question that emerges is how this impacts the mobility, and ultimately the ionic conduction, on these systems. Hence, the transference number of Li^+ (t^+) was calculated by the following expression^{12,86,120} ($t^+ + t^- = 1$):

$$t^+ = \frac{D^+}{D^+ + D^-} \quad (3.20)$$

where D^+ and D^- are the diffusivity of cation and anion, respectively.

Figure 3.12 and Table 3.2 present the results for different molalities and at different temperatures. On both cases, a considerable influence of anion on the total charge transport is seen ($t^+ < 0.5$). This is caused by the packed solvation shell around Li^+ turning it heavier, and hence decreasing the ion mobility.

A closer look to Figure 3.12 shows a slightly higher transference number for LiPyr in comparison with LiPF_6 both in DMSO solvent solution. This result implies that, even though

they have different solvation shell compositions, the size and motion are similar. Our results show good agreement with typical battery electrolytes, such as LiPF_6 and LiBF_4 in propylene carbonate¹¹, as well as for poly(allylglycidyl ether-lithium sulfonate) in DMSO solution¹². Furthermore, in our findings, the transference number is almost independent of molality, but highly influenced by temperature for LiPyr (Table 3.2).

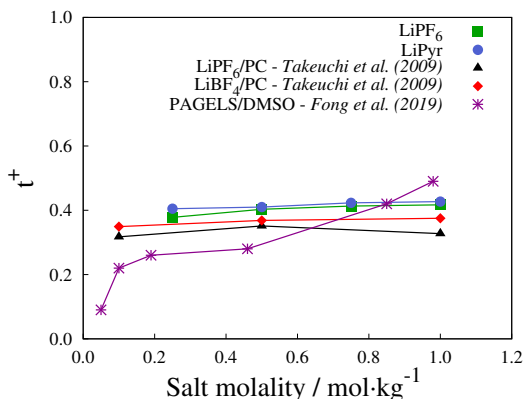


Figure 3.12: The Li^+ transference number (t^+) for LiPF_6 and LiPyr in DMSO solutions at 1 atm and 298 K for different molalities calculated from Green-Kubo diffusivity. Uncertainties are on the order of ± 0.0001 for all results. Experimental measurements for LiPF_6 and LiBF_4 in PC¹¹ and, simulation results for poly(allylglycidyl ether-lithium sulfonate) (PAGELS) in DMSO¹² are also shown for comparison purposes.

Table 3.2: The Li^+ transference number (t^+) for LiPF_6 and LiPyr in DMSO solutions with $1 \text{ mol}\cdot\text{kg}^{-1}$ at different temperatures at 1 atm, calculated from Green-Kubo diffusivity^a.

	Temperature / K		
	298	330	360
t^+ for LiPF_6 in DMSO	0.417	0.412	0.410
t^+ for LiPyr in DMSO	0.427	0.439	0.456

^a Uncertainties are on the order of ± 0.0001 for all results. They were propagated from uncertainties of diffusion coefficients.

3.4.4 Consequences for Li-Air battery

DMSO is a widely used solvent for Li-air batteries^{17,121}. Having a high Donor Number (DN = 29.8), DMSO has the ability to donate free electron pairs to coordinate with acceptor atoms from ions in solution. DMSO also has high oxygen solubility, and high polarity^{83,121,122}. These features confer to DMSO good interaction with positive ions as Li^+ , contributing to the stability of intermediate products on Li-air reactions¹²¹.

Nevertheless, Burke *et al.*¹⁸ have shown that the anion DN can largely affect LiO_2 solubility, due to anion and Li^+ correlation. The authors evaluated two anion types: NO_3^- , which has a planar shape and high DN; and TFSI^- , which has ellipsoidal shape and low DN. The combination of high DN anion and low DN solvent DME (1,2-dimethoxyethane) provided good

capacities and increased the stability of intermediate reaction products. Changing the solvent to DMSO (high DN), no improvement was observed.

In this work, we have analyzed two different salts (LiPF_6 and LiPyr) in DMSO solution. Our results indicate that the anion shape and charge distribution play important roles on the Li^+ solvation. For PF_6^- , which has low DN and a spherical shape¹²³, no impact on solvation of Li^+ was observed, being Li^+ fully solvated by DMSO. On the other hand, for Pyr^- , Li^+ is partially solvated by DMSO and, at same time, participates with Pyr^- in ion pairing. Pyr^- has a planar shape, and based on measures for other nitrogen-based anions¹²⁴, one can speculate Pyr^- has a high DN. In NO_3^- , the negative termini position is at the three oxygens, and, in Pyr^- , it is located largely at the nitrogen and close hydrogens (H4 - Fig. S8 of ESI A). The high DMSO ability to solvate Li^+ decreases the possibility of NO_3^- negative structure to interact with Li^+ , due to oxygen partial charges. In Pyr^- case, even in presence of DMSO solvent, the charge position facilitates Li^+ and Pyr^- coordination.

A direct consequence of the solvation shell is the reaction path in the full cell evaluation. As reported by Gittleston *et al.*⁴⁷, the solvation of Li^+ is the major factor that impacts on the reaction mechanism.¹⁸ The free energies of both Li^+ and LiO_2 are directly related to the Li^+ coordinated species. Their experimental measures show that ion-pairing formation induces the stability of the intermediate anion O_2^- in solution, which increases the Li_2O_2 growth mechanism. The authors demonstrated that no ion-pairing was noticed in DMSO solutions of LiTFSI or LiNO_3 .

Dilimon *et al.*¹²¹ have evaluated the stability of superoxide formation in sodium-air batteries. The authors concluded that stabilization of superoxide formation is conditioned to the softness of Li^+ solvation shell. According to their findings, high DN solvent (DMSO) and high DN anion (SO_3CF_3^-) make the superoxide formation possible, which increases the battery reversibility. Abraham *et al.*¹²³ have shown that cation and anion coordination in the first solvation shell increases the softness on Li^+ . And the co-participation of solvent and anion in solvation structure of cation is essential for superoxide stability¹²¹. Since Li^+ is a hard ion, the same as Na^+ , a similar behavior is expected. The negative termini in SO_3CF_3^- are predominantly at the external oxygens, the same as for nitrogen and its close hydrogens (H4 - Fig. S8 of ESI A) in Pyr^- , which may justify the good interaction of SO_3CF_3^- with Na^+ .

As the solvation shell, the transference number (t^+) elucidates the impact of Li^+ mobility on charge transference process. Lower values of t^+ express a limited Li^+ motion. This limitation promotes concentration gradients that impacts the ion transfer when reaction with adsorbed O_2 in Li-air devices^{86,120}. Our results show slightly higher transference numbers in comparison with typical carbonated solvents (Fig. 3.12). Regarding LiPF_6 and LiPyr in DMSO, LiPyr presented an averaged growth of 3.3% for molality and 6.2% for temperature on t^+ in comparison to LiPF_6 . Higher values of t^+ are beneficial for the overall battery performance¹²⁰.

Despite similar ionic conductivities of the two selected anion shapes our results show that the coordination of them with the respective anion is very distinct. We hope that this information highlighted here might aid future experimental work investigating the stability of dissociated intermediaries such as LiO_2 with important consequences for the reaction pathway.

3.5 Conclusions

LiPF_6 and LiPyr in DMSO solutions constitute possible electrolyte candidates for Li-O_2 battery applications. Carrying out classical molecular dynamics simulations, Li^+ solvation and the transport properties of these solutions have been assessed.

Through the calculation of transport properties, such as viscosity, diffusion coefficient, and ionic conductivity, we concluded that the ionic transport is quite similar regardless of the anion type. The differences in the anion shape and composition, however, are sufficient to affect solution viscosity: LiPyr in DMSO solution is less viscous than LiPF_6 in DMSO.

The structural arrangement of these two solutions presents a completely different scenario. In $\text{LiPF}_6/\text{DMSO}$ system, Li^+ is fully solvated by DMSO, and its coordination number with DMSO oxygen matches exactly what has been claimed in the literature for the formation of $\text{Li}^+(\text{DMSO})_4\text{PF}_6^-$ ion pair¹¹⁷. In LiPyr/DMSO system, however, the Li^+ first solvation shell is partially shared between the solvent and the anion. Despite having different solvation shell, the transference number indicates that their volumes are similar.

The ionic dynamics of these solutions, as manifested in the computed transport properties, are similar, even though the Li^+ solvation in each solution is different. The selection of the pair lithium salt/solvent is essential for an optimum operation of a Li-O_2 battery, and many variables ought to be analyzed. In the present study, we have shown that similar transport behavior can be observed for solutions with different solvation properties, which might have a significant impact on reaction intermediate (LiO_2) solubility and therefore on the overall reaction mechanism. This conclusion might give insights for experimental design and analysis when addressing electrolyte impact over Li-O_2 devices.

Conflicts of interest

There are no conflicts to declare.

Acknowledgments

We thank Guido Costa Souza de Araújo for the CCES availability (Fapesp 2013/08293-7), Leandro Negrini Zanotto for assistance in the computer cluster utilization, the Center for Research Computing (CRC) at the University of Notre Dame for the computational resources, and the Brazilian agencies CNPq (Reference Number 203393/2018-0) and CAPES (Finance Code 001) for the financial support. This work was supported by FAPESP grant 2017/11958-1, and Shell, and the strategic importance of the support given by ANP (Brazil's National Oil, Natural Gas and Biofuels Agency) through the R&D levy regulations. LFMF acknowledges the support from the São Paulo Research Foundation (FAPESP) grant no. 2018/02713-8. YZ and EJM acknowledge the support from the U.S. Department of Energy, Office of Science, Basic Energy Sciences, Joint Center for Energy Storage Research under Contract No. DE-AC02-06CH11357.

3.6 Permission to reproduction

If you are the author of this article you still need to obtain permission to reproduce the whole article in a third party publication with the **exception of reproduction of the whole article in a thesis or dissertation**. Information about reproducing material from RSC articles with different licences is available on our **Permission Requests page**.

Chapter 4

Effect of electrode material and solvent donor number in Li-air battery: insights from Molecular Dynamics simulations[‡]

Juliane Fiates^{a,b}, Yong Zhang^b, Luís F. M. Franco^a, Edward J. Maginn^b and Gustavo Doubek^a

^a *School of Chemical Engineering,
University of Campinas,
Campinas 13083-852, Brazil.*

^b *Department of Chemical and Biomolecular Engineering,
University of Notre Dame,
Notre Dame, Indiana 46556, USA.*

4.1 Abstract

Lithium-air battery is getting attention as a good technology for energy storage. Nevertheless, the design of such a device still faces some crucial limitations. The most challenging one concerns the selection of electrode and solvents to provide good performance during the cell operation. Based on literature evidences, we have selected three system configurations of electrode/electrolyte to be evaluated via molecular dynamics simulation: gold/DMSO, graphene/DMSO, and graphene/TEGDME using lithium hexafluorophosphate-LiPF₆, considering the discharging process of the battery. We show that the local concentration distributions of Li⁺ are highly influenced by the electrode-solvent pair. Furthermore, Li⁺

[‡]It will be submitted for publication at The Journal of Physical Chemistry C.

solvation depends on the electrode material, and its mobility and electrical double layer capacitance are strongly correlated with the solvent. The electrode material and the solvent donor number play an important role over reaction rates and mechanisms. Therefore the findings presented here can help to elucidate experimental behavior of typical Li-air materials.

4.2 Introduction

Lithium-air (Li–O₂) batteries entail a promising energy storage technology, achieving energy density levels comparable to the ones from fossil fuels^{4,16}. Even though in recent years Li-air battery is receiving considerable attention, some challenges to improve the performance of such a device remain^{4,16,125}.

Much effort has been put in developing electrodes, selecting electrolytes, and understanding reactions pathways. Concerning electrodes, two important features that must be considered are porosity and morphology. Li-air battery electrode needs to accommodate the discharge products, promote O₂ diffusivity, and contribute the recharging process^{16,126}. Carbon-based electrodes are widely used as porous media for Li-air batteries due to their good conductivity and low production cost. Nevertheless, these materials suffer from oxidation at high voltages and chemical instability^{16,127–129}. Metal electrodes, such as gold, have good electron transport and high oxidation stability, therefore appear as alternatives to carbon materials¹²⁷. Peng *et al.*²¹ have achieved good cyclability (over 100 cycles) with small amount of by-products using gold electrode.²¹ They were also able to operate the system at high overpotentials. Nonetheless, the high potentials required to keep the reversibility at the gold electrode limit their use because of the degradation of the solvent²².

The electrolyte, which is composed by a solvent and a lithium salt, must exhibit good O₂ solubility and diffusivity, low volatility, and high lithium conductivity^{16,17,47}. High donor-number (DN) solvents such as dimethyl sulfoxide (DMSO)^{83,122} is a popular choice for lithium-air battery applications. Several authors have shown that DMSO has a positive impact over battery operation (reversibility, reaction pathway, Li⁺ conductivity)^{5,17,47,130}. DMSO, however, is unstable¹²⁹ and leads to side product formation and lower cyclability^{23,24}. This electrolyte also deteriorates at high potentials²². Tetraglyme (TEGDME) is another important solvent for Li-air batteries. Even though TEGDME is a low DN solvent^{83,122}, and exhibits high volatility and lower Li⁺ conductivity, TEGDME is known to have high stability and good O₂ solubility^{17,47,129}. DMSO has a better performance in charge capacitance, but TEGDME increases the stability of cycling at long-life operation. TEGDME also improves reaction reversibility, and lowers the impact of side products on the porous electrode^{23,24}.

The selection of the electrode and the solvent plays a crucial role in Li-air system, and the effect of multiple variables over this system has already been addressed in literature. Jung *et al.*²⁵

reported good capacity and cycle performance when cell design is based on a combination of electrolyte and electrode characteristics. According to Gittleston *et al.*¹⁷, paring effect between electrode catalyst and solvent type was observed. The authors claimed that a careful selection of catalyst and solvent materials are necessary to achieve good reaction reversibility. Dutta *et al.*²⁶ showed that carbon electrode thickness and the selection of the coupled electrolyte can affect the energy density and power capacity of Li-air batteries. Marchini *et al.*²⁷ presented that synergy between solvent and anion is also important. The authors showed that a certain combination of anion and solvent leads to lower decomposition of electrolyte when gold electrode is under high potential, which is a beneficial factor for reaction reversibility of this material.

Most discussion in the literature on the coupled effect of materials/components of Li-air batteries has been motivated by experimental evidences over the device operation performance (cyclability, charge density, capacity). A deeper look at the variables and their effects at a molecular scale can help to understand the mechanisms behind the macroscopic experimental findings. Molecular dynamics simulations have been widely applied to electrochemical systems.¹³¹ Several authors reported findings on systems subjected to electric potentials^{13,71,79,89,132,133}, temperature⁷¹, and solvent composition^{75,78}. In the current work, we evaluate two electrode materials, gold and graphene, and two solvents (DMSO and TEGDME) under various electrical potentials using molecular dynamics simulations.

4.3 Simulation details

Classical equilibrium molecular dynamics simulations were carried out considering two types of electrodes: gold (111) surface and graphene. Each electrode (anode or cathode) was simulated with a flat wall made of four layers of gold or graphene, and each layer contains 120 gold or 336 carbon atoms, respectively. The setup of these systems are demonstrated in Figure 4.1. Two electrolyte compositions were evaluated: 1 mol·kg⁻¹ of lithium hexafluorophosphate (LiPF₆) in DMSO, and 1 mol·kg⁻¹ of LiPF₆ in TEGDME. The solutions were composed of 512 DMSO and 40 LiPF₆ molecules, and 180 TEGDME and 40 LiPF₆ molecules, respectively. The initial configurations were assembled using Packmol package⁹⁵. For all cases, the inner layer of each electrode was set 80 Å apart to achieve a bulk-like behavior in the center region of system¹³. It was characterized by the achievement of NPT density in a region of 20 Å thickness in center of system.

All simulations were performed using LAMMPS package²⁹. Force field parameters for electrodes and electrolytes were taken from the literature^{8,14,92,93,134,135}, and are presented in Tables S1 and S2. The charges designated for TEGDME atom are shown in Figure S1¹⁴. Lennard-Jones parameters for cross interactions were obtained using the Lorentz-Berthelot combining rules. Periodic boundary conditions were applied in the *x* and *y* directions. A vacuum

space of 440 Å was added in z direction to prevent any spurious interaction. Long range electrostatic interactions were calculated by particle-particle particle-mesh scheme (PPPM)⁹⁹, and the unwanted slab-slab interactions in z direction were corrected^{136,137}. Electrode atoms were kept fixed. In the cases of charged electrode, a small charge was added to each atom of the inner layers. Negative charges were balanced by positive charges on the opposite wall to guarantee electroneutrality of the system. All simulations were carried out in the canonical ensemble (NVT) at 298 K, applying Nosé-Hoover thermostat^{96,97}.

The simulations were run for 90 ns for TEGDME system, and for 50 ns for DMSO systems. The first 50 ns for TEGDME system and 40 ns for DMSO systems were discarded as equilibration steps. Block-averaging was applied at the production stage, fixing blocks of 4 ns and 2 ns for TEGDME and DMSO systems, respectively.

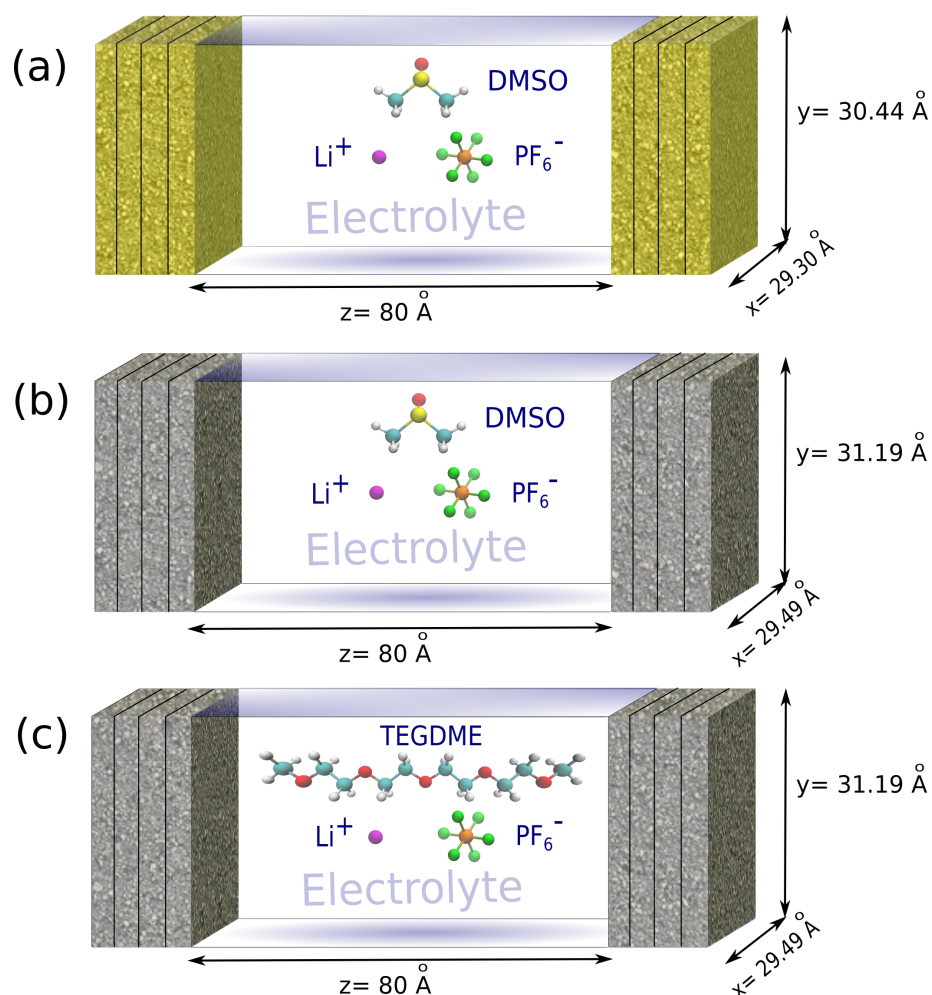


Figure 4.1: Schematic representation of the simulated systems: (a) gold electrodes and DMSO/LiPF₆ electrolyte, (b) graphene electrodes and DMSO/LiPF₆ electrolyte, and (c) graphene electrodes and TEGDME/LiPF₆ electrolyte. Electrolyte atom color code: oxygen (red), hydrogen (white), carbon (cyan), sulfur (yellow), lithium (magenta), phosphorus (orange), and fluorine (green).

4.4 Results and discussion

4.4.1 Electrolyte local concentration

Figures 4.2, 4.3, and 4.4 show the local concentration profiles according to the center-of-mass position of each molecule along z direction for the following electrode/electrolyte compositions: gold/LiPF₆ in DMSO, graphene/LiPF₆ in DMSO, and graphene/LiPF₆ in TEGDME, respectively. The solvent concentration was normalized by its bulk value.

DMSO and TEGDME are densely packed near the uncharged electrodes in comparison with the center of the pore. At least four layers of DMSO are adsorbed on both electrodes, as characterized by the oscillatory profile observed in Figures 4.2 (a) and 4.3 (a). Similar behavior was also reported by other researchers for the solvent at the solid/liquid interface^{13,75,132}. On the other hand, only one layer of TEGDME adsorption can be identified unambiguously (Figure 4.4 (a)). For all systems, the first solvent peak appears at around 3 Å, which is due to the van der Waals repulsion force between the electrolytes and electrode^{13,138}. Close to the graphene electrode, both DMSO and TEGDME present similar concentrations in the first peak. On the other hand, DMSO shows half concentration at the Au (111) surface relative to that at graphene surface, and a smoother peak shape. A quite uniform concentration profile with a small intercalation of anion and cation is observed for Li⁺ and PF₆⁻ ions in the three systems near neutral surface. The layering of ions is caused by the electrostatic attraction as reported in the literature¹³⁸. The insets of Figures 4.2 (a), 4.3 (a), and 4.4 (a) show the ions randomly distributed in systems with neutral electrodes.

Adding a surface charge of $-4.85 \mu\text{C}\cdot\text{cm}^{-2}$ at the left electrode (balanced with the opposite charge on the right electrode), the formation of a Li⁺ peak around $z=6$ Å for all systems is observed, as shown in Figures 4.2 (b), 4.3 (b), and 4.4 (b). Comparing the gold and graphene systems is possible to see that concentration in the first peak is roughly the same. However a second adsorbed layer is only noticed in graphene (~ 10 Å). Regarding the TEGDME solvent, the Li⁺ peak presents a broader shape in comparison with DMSO systems. Considering PF₆⁻ no evidence of peak formation is observed in all systems. Evaluating the solvent behavior, DMSO shoulders are present in gold and graphene first peak. In TEGDME the peak formed in the neutral system decomposes in an almost constant distribution. It can be caused for the solvation of Li⁺ present in this region. Moreover, the size of this solvent with 37 atoms being 5 of them oxygens, may lead to this distribution along z . The insets of Figures 4.2 (b), 4.3 (b), and 4.4 (b) show the visualization of those systems when applied this surface charge.

Increasing the charge to $-9.7 \mu\text{C}\cdot\text{cm}^{-2}$, different evolution is observed for each system (Figures 4.2 (c), 4.3 (c), and 4.4 (c)). For Li⁺ in gold an decrease of first adsorbed peak and a formation of a second is noticed. In graphene the Li⁺ concentration doubles ($\sim 10 \text{ mol}\cdot\ell^{-1}$) in

comparison to the $-4.85 \mu\text{C}\cdot\text{cm}^{-2}$ charge concentration. For the TEGDME system, Li^+ has a second peak larger than the first, which might emerge because of the solvent-cation interaction. The oxygen atoms of this solvent strongly interact with Li^+ creating an opposite force against the electrical field attraction at the wall. The PF_6^- behavior is independent of the surface charge increasement for DMSO composition in gold and graphene. However, the presence of two adsorbed layers of TEGDME close to the two Li^+ peaks creates a crowded area that keeps PF_6^- out of this region, as can be seen in Figure 4.4 (c). Regarding DMSO in gold an increase of concentration of the first adsorbed layer is notice. On the other hand in graphene, DMSO concentration is kept constant with charge increase. In both scenarios the shoulders presented in the lower charge are more prominent. The insets of Figures 4.2 (b), 4.3 (b), and 4.4 (b) show the Li^+ preference to the negative wall (left), and the PF_6^- preference to the positive wall (right), as expected.

In Figure 4.2 (a) and (c), we also compare our results with those reported by Sergeev *et al.*¹³. For zero charge electrode system, excellent agreement is observed for Li^+ and PF_6^- in DMSO with our simulation slightly underestimates the first peak. For the charged electrode system, although the intensities differ from the values reported in Sergeev *et al.*¹³ work, the profile peak positions are in reasonable agreement for both Li^+ and PF_6^- .

As can be noticed in Figure 4.4, the simulation of TEGDME as solvent is related with high noise in the concentration profiles. To provide more reliability to data presented in this study, a statistical analysis of all concentrations distributions are shown in Figures S2, S3, and S4. The calculations presented in the Supplementary Information were developed using multi-blocking method. We can see that higher standard deviations are observed for TEGDME results in comparison with those from DMSO simulations. However, the average measure is able capture the behavior of this system. The large variation on TEGDME data may be associated to its high viscosity, and the difficulty to predict data from this solvent by MD simulation. The value calculated for its viscosity based on MD simulation, according to a correlation taken from Barbosa *et al.*¹⁴ is 66.5 cP. The experimental measure at the same temperature is 3.40 cP¹³⁹. Comparing experimental and simulated data for DMSO viscosity, we found the values of 2.098 cP calculated by MD simulation¹⁴⁰, and 1.967 cP as experimental measure⁷. Those data corroborate the difficulty to simulate systems composed by TEGDME compared to DMSO, as well as it justifies the higher standard deviation associated with its results.

The findings presented in this section evidences the impact of electrode material in Li^+ and DMSO behavior. Comparing DMSO and TEGDME a similar peak shape is noticed for neutral and $-9.7 \mu\text{C}\cdot\text{cm}^{-2}$ charged systems. However, completely different Li^+ profiles are observed. An important aspect of these results regard their impact over reactions and overall battery operation. One Li^+ can be the a limiting factor and its solvation shell is a key aspect of reaction mechanism (see further discussion).

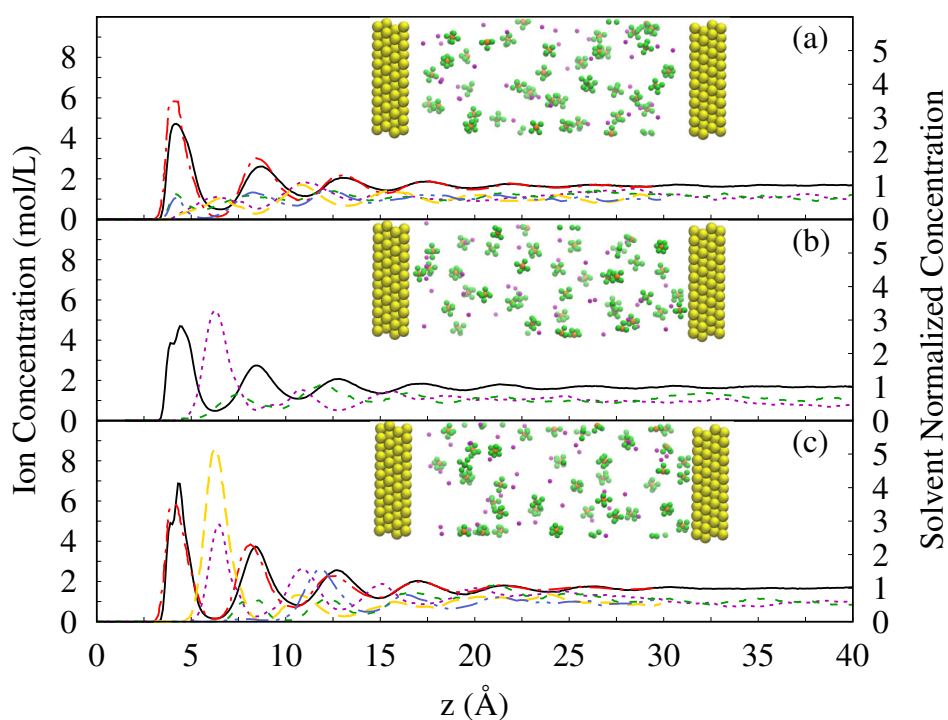


Figure 4.2: Local concentration profiles of: ions (left y axis) and DMSO solvent (right y axis). DMSO (this work) - black solid line, DMSO (Sergeev *et al.*¹³) - red dot dashed line; Li^+ (this work) - magenta dotted line, Li^+ (Sergeev *et al.*¹³) - yellow long dashed line; PF_6^- (this work) - green dashed line, PF_6^- (Sergeev *et al.*¹³) - blue dot dot dashed line. Surface charges applied: (a) zero, (b) $-4.85 \mu\text{C}\cdot\text{cm}^{-2}$, and (c) $-9.7 \mu\text{C}\cdot\text{cm}^{-2}$. The insets show the visualization of ions and electrodes (left-negative and right-positive). Atom color code: gold (yellow), lithium (magenta), phosphorus (orange), and fluorine (green).

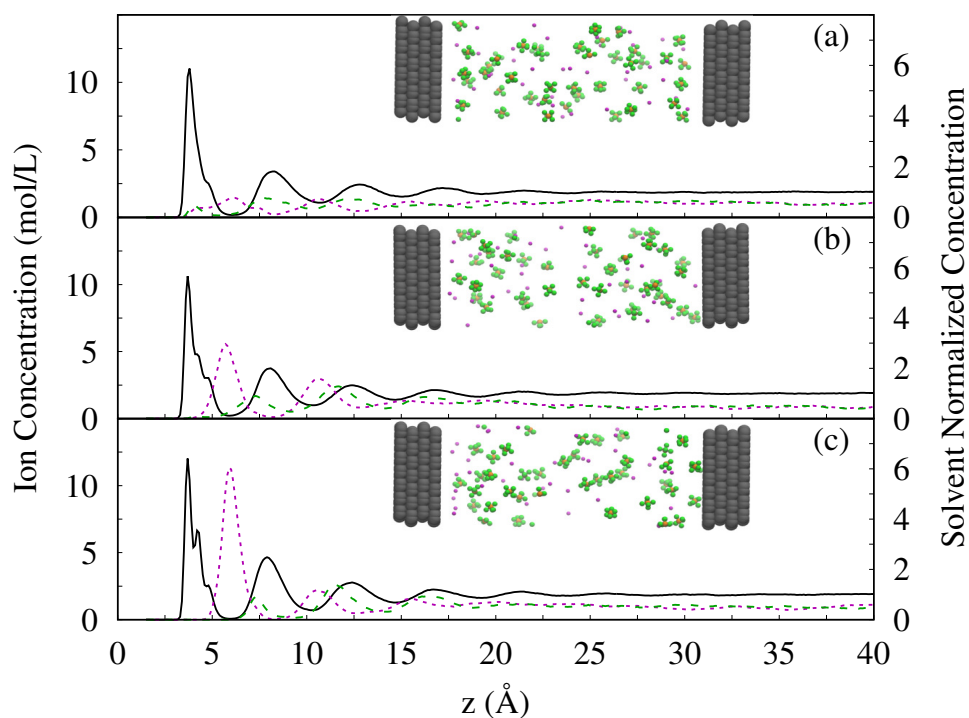


Figure 4.3: Local concentration profiles of: ions (left y axis) and DMSO solvent (right y axis). DMSO - black solid line; Li^+ - magenta dotted line; PF_6^- - green dashed line. Surface charges applied: (a) zero, (b) $-4.85 \mu\text{C}\cdot\text{cm}^{-2}$, and (c) $-9.7 \mu\text{C}\cdot\text{cm}^{-2}$. The insets show the visualization of ions and electrodes (left-negative and right-positive). Atom color code: graphene (gray), lithium (magenta), phosphorus (orange), and fluorine (green).

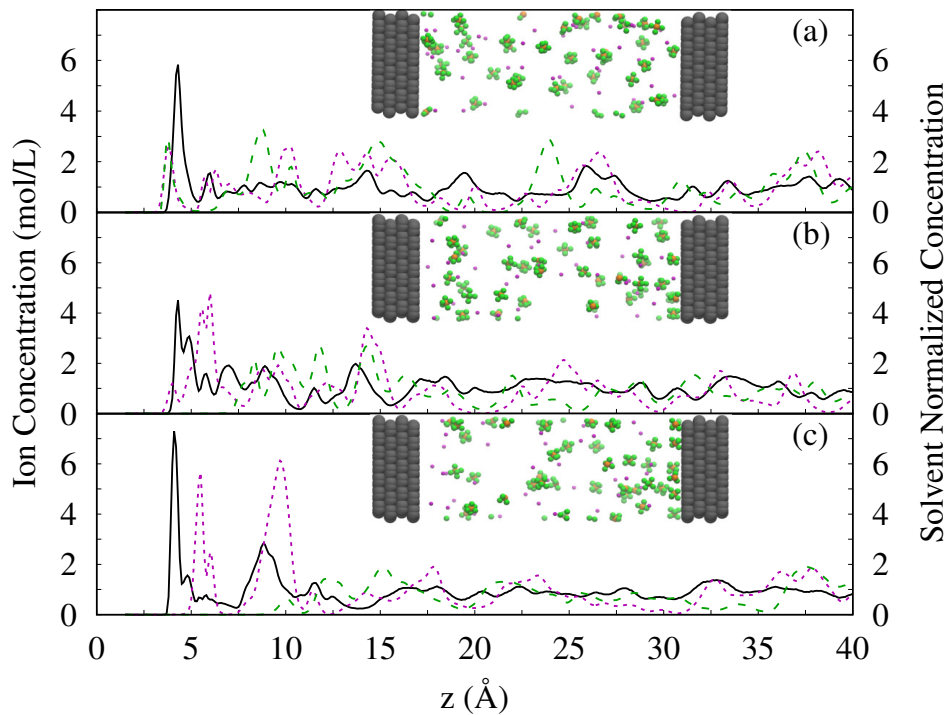


Figure 4.4: Local concentration profiles of: ions (left y axis) and TEGDME solvent (right y axis). TEGDME - black solid line; Li^+ - magenta dotted line; PF_6^- - green dashed line. Surface charges applied: (a) zero, (b) $-4.85 \mu\text{C}\cdot\text{cm}^{-2}$, and (c) $-9.7 \mu\text{C}\cdot\text{cm}^{-2}$. The insets show the visualization of ions and electrodes (left-negative and right-positive). Atom color code: graphene (gray), lithium (magenta), phosphorus (orange), and fluorine (green).

4.4.2 DMSO ordering and Li^+ solvation

To further study the DMSO behavior presented in Figures 4.2 and 4.3, the DMSO ordering close to the electrode was analyzed by calculating the order parameter:

$$P_2(\cos \theta) = \left\langle \frac{3}{2} \cos^2 \theta - \frac{1}{2} \right\rangle \quad (4.1)$$

The results are shown in Figure 4.5, where θ is the angle between S-O bond and the surface normal to the electrode (z). The order parameter ranges from -0.5 to 1. A value of -0.5 means that S-O is parallel to the electrode (Figure 4.6 (a)), whereas 1 means S-O is perpendicular to the surface (Figure 4.6 (b)), and a value of 0 indicates a uniform distribution.

Figure 4.5 presents the order parameter calculated for DMSO confined in gold and graphene electrode systems under different electric fields (a) at zero charge, (b) at $4.85 \mu\text{C}\cdot\text{cm}^{-2}$, and (c) at $9.7 \mu\text{C}\cdot\text{cm}^{-2}$. Figure 4.6 (a) indicates that DMSO has no preferential orientation, from which one can infer that the sole presence of an uncharged wall is insufficient to impose any specific orientational arrangement of DMSO molecules. This result is in accordance with Sergeev *et al.*¹³ ordering data presented for DMSO in gold¹³. However, it is

somehow different to what has been observed for united-atom alkanes (with uncharged beads) close to calcite crystals, where a preferential ordering has been indeed observed¹⁴¹. This was expected, regarding the difference between DMSO and an alkane chain as well as the electrodes, gold and graphene in this work, and calcite in Santos *et al.*¹⁴¹ study.

With imposing electric fields, however, some ordering of DMSO molecules close to the electrodes is observed. Charging the surfaces with $-4.85 \mu\text{C}\cdot\text{cm}^{-2}$, the S-O vector predominantly points towards the electrolyte solution (perpendicular to the electrode surface), although in graphene system the first layer shows a slight reordering. It is probably caused by the shoulder as shown in Figure 4.3 (b).

Increasing the electric field, a stronger ordering becomes more pronounced, as can be seen by the second adsorbed layer in both systems (Figures 4.5 (c)), as well as the reordering of S-O vector in graphene electrode system in its first layer (shoulder). Therefore, DMSO ordering at the electrode surface is mainly driven by Coulombic interactions between solvent atoms and the electrified electrode¹³. Additionally, in graphene electrode systems, the presence of a higher concentration of Li^+ right next the DMSO may affect its ordering. The Coulombic force leads the DMSO oxygen to interact and to solvate Li^+ . Figure 4.6 (b) exemplifies the DMSO ordering in the presence of an electric field.

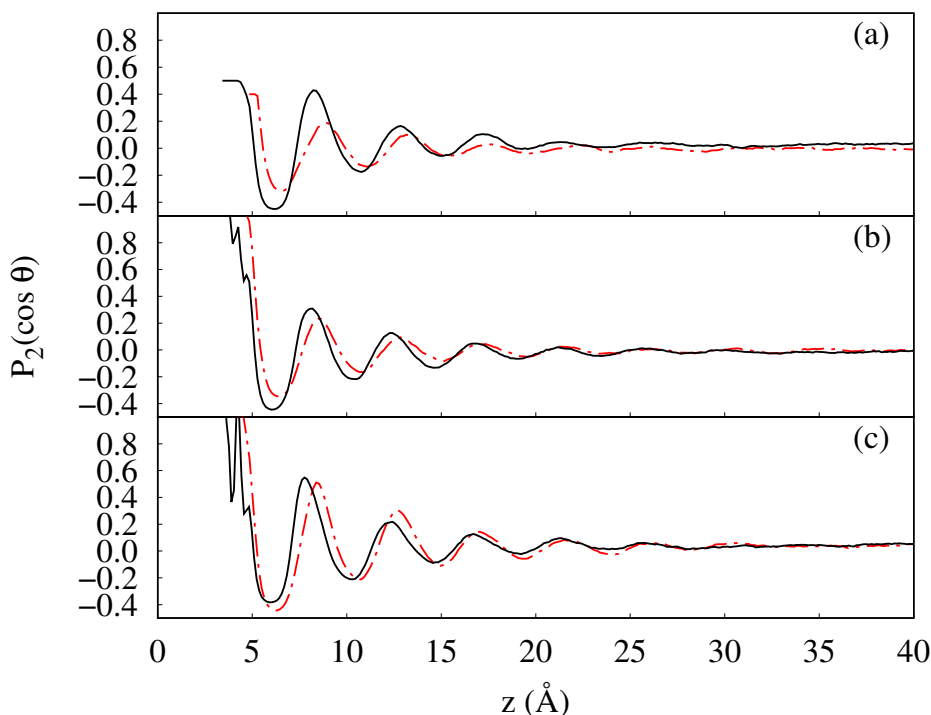


Figure 4.5: Order parameter ($P_2(\cos \theta)$) for DMSO in gold (red dot-dashed line) and graphene (black solid line) electrode systems subjected to different surface charges: (a) zero, (b) $-4.85 \mu\text{C}\cdot\text{cm}^{-2}$, and (c) $-9.7 \mu\text{C}\cdot\text{cm}^{-2}$.

An important question that arises from DMSO ordering is related to its ability to solvate

Li⁺ ions. To answer this question, the coordination number (n_{ij}) was evaluated by the running integral of the radial distribution function (RDF - g_{ij}) as shown in Equations 4.2 and 4.3⁵⁷. For the RDF calculation, the data from atoms position were sampled into a layer with a thickness of 10 Å from the electrode to the electrolyte.

$$g_{ij}(r) = \frac{V}{N_i N_j} \sum_{i=1}^{N_i} \sum_{j=1}^{N_j} \delta(r - r_{ij}) \quad (4.2)$$

$$n_{ij}(r) = \frac{N_j}{V} \int_0^{r_{\min}} 4\pi g_{ij}(r) r^2 dr \quad (4.3)$$

where g_{ij} is the RDF between atoms types i and j , V is the volume, N_i and N_j are the numbers of i and j atoms, respectively, r_{ij} is the Euclidean distance between these atoms, δ equals 0 or 1 according to the absence or the presence of atoms within the analyzed shell, n_{ij} is the number of coordinated j atoms around i atom, and r_{\min} is the cut-off distance to evaluate the coordination number. In the current study the first minimum between the first two peaks in g_{ij} was established as the cut-off distance.

Table 4.1 shows the calculated coordination numbers in each solvent/electrode system. According to the literature¹⁴⁰, in a system composed by LiPF₆ in DMSO at 1 mol·kg⁻¹ and 298 K, the Li⁺ solvation shell is composed by four molecules of DMSO. Based on this, we notice that the electrode presence close to electrolyte decrease the capacity of DMSO to solvate Li⁺ in gold and graphene. However, a low impact of electric field is observed in Li⁺ solvation shell in these systems. Furthermore, the DMSO order unaffected the Li⁺ shell composition even increasing the surface charge in gold. For graphene, the slighter increase of Li⁺ solvation at the higher charge may be correlated to the shoulder formation. In this scenario the intensity of the DMSO reordering may increase its ability to solvate Li⁺. Comparing graphene and gold, we note a higher overall ability of DMSO to solvate Li⁺ in graphene.

Considering TEGDME with graphene electrode, as such in DMSO/gold system, the electric field was unable to change significantly the Li⁺ solvation structure. Comparing TEGDME and DMSO/graphene systems, Li⁺ is solvated by five atoms of oxygen in TEGDME. One molecule of this solvent is composed by five atoms of oxygen, it leads us to believe that each molecule creates a ring around Li⁺ as exemplified in Figure 4.6 (d). On the other hand, in DMSO the solvation is composed roughly by three molecules of DMSO as illustrate in Figure 4.6 (c).

These findings may be crucial to determine reactions mechanisms based on solvent characteristics, as well as to understand the role of electrode material over it (see further discussion).

Table 4.1: Coordination number calculated from running integrals of the radial distribution functions of Li^+ and O (from the solvent)

Charge ($\mu\text{C}\cdot\text{cm}^{-2}$)	Solvent		
	DMSO	DMSO	TEGDME
	Electrode		
	Gold	Graphene	Graphene
0.00	3.39	3.55	5.00
-4.85	3.34	3.55	4.92
-9.70	3.34	3.69	4.93

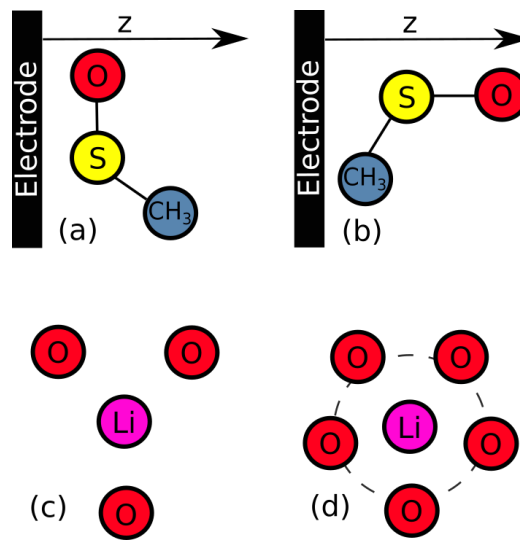


Figure 4.6: DMSO ordering: (a) $P_2(\cos \theta) = -0.5$, and (b) $P_2(\cos \theta) = 1$. Li^+ solvation by O from solvent: (c) in DMSO (the oxygen atoms came from three different molecules), and (d) in TEGME (the dashed line represents that the oxygen atoms came from only one molecule).

To elucidate the process of Li^+ transport across the system, *i.e.*, the desolvation from the bulk ($\sim 15 \text{ \AA}$) and the adsorption on the electrode ($\sim 5 \text{ \AA}$), the free energy profile ($W(z)$) was calculated as follows^{74,78}:

$$W(z) = -k_B T \ln \left(\frac{\rho_{\text{Li}}(z)}{\rho_{\text{Li}}(\text{bulk})} \right) \quad (4.4)$$

where $W(z)$ is the position dependent free energy, k_B is the Boltzmann constant, T is the absolute temperature, and $\rho_{\text{Li}}(z)$ is the Li^+ density at a distance z from the electrode, and $\rho_{\text{Li}}(\text{bulk})$ is the bulk Li^+ density.

Figure 4.7 shows the $W(z)$ profile for the three systems, subjected to three different electric fields. Figures 4.7 (a), (b), and (c) present results for gold/DMSO, graphene/DMSO, and graphene/TEGDME systems, respectively. The energy barrier for Li^+ partially adsorption at electrode increases with an increase of surface charge in all systems (see the black arrows at $\sim 4 \text{ \AA}$). This can be caused by the increase of densely packed solvent close to the electrode at higher potentials. Moreover, the more pronounced evolution presented in DMSO

systems comparing to TEGDME may be correlated to the DMSO ordering when subjected to electric charges. Comparing the three systems, a shift towards the electrode is noticed in graphene/TEGDME in comparison with gold/DMSO and graphene/DMSO. One we noticed a lower concentration of DMSO solvent (Figs. 4.2 and 4.3) compared to TEGDME (Fig. 4.4), hence the proximity of Li^+ to the electrode may be due to the smaller volume of the Li^+ [TEGDME] solvation shell in comparison with those of Li^+ [DMSO].

A second arrow at distance of $\sim 6\text{-}5 \text{ \AA}$ shows the decrease of energy barrier for the adsorption of Li^+ in the electrode as electric field increases. After this region, and moving forward to bulk area ($\sim 15 \text{ \AA}$) insignificant energy barriers are noticed. Except for graphene/TEGDME system at surface charge of $-9.7 \mu\text{C}\cdot\text{cm}^{-2}$ where two more energy penalties are present at distances of ~ 7 and 12 \AA .

Both DMSO-based systems present similar free energy profiles along z , leading us to believe that free energy barrier for Li^+ to transport to the surface is only impacted by solvent type. As discussed previously, the higher TEGDME viscosity compared to DMSO imposes restrictions to the Li^+ mobility. It increases the energy barriers that Li^+ has to overcome in order to approach the surface, agreeing with the profile presented here.

Our results are in agreement with Vatamanu *et al.*⁷⁴ observations for LiPF_6 in carbonated solvents at graphite surface. Moreover, the Li^+ solvation structure and its interaction with electrode surface can impact on the Li^+ and O_2 reaction mechanism, as discussed further in more details.

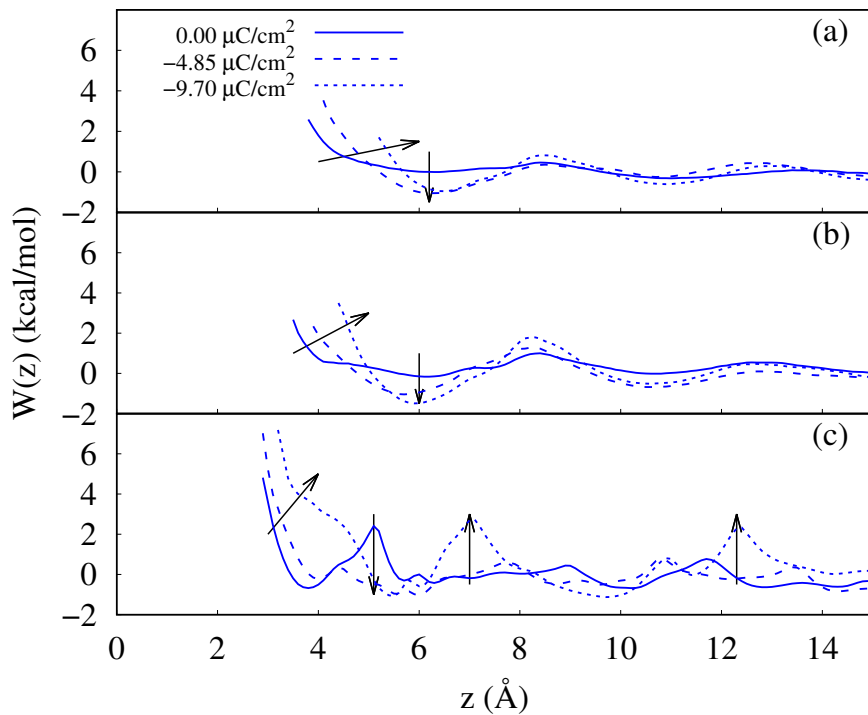


Figure 4.7: Free energy profile ($W(z)$) for lithium near the electrodes for (a) gold/DMSO, (b) graphene/DMSO, and (c) graphene/TEGDME.

4.4.3 Voltage drop between electrode and electrolyte

In this study we used the Fixed Charge Method (FCM) to mimic the battery discharge process. Although, the Constant Potential Method (CPM) being more precise when simulating interface behavior under electrical charge, the computational cost associated with its simulation is relatively high. Wang *et al.*⁷⁰ extensively compared both methods and they concluded that similar results can be obtained with both of them at low potentials (≤ 2 V). However, these authors claim that significant differences were noticed above 4 V.

Battery experiments are typically run at low potentials (~ 3 V^{5,142}) which enables the use of FCM to simulate this type of systems. Furthermore, in our simulations the electrodes structure are flat. According to Vatamanu *et al.*⁷¹ the FCM leads to good results on simulation of flat electrodes.

The interaction between electrode and electrolyte creates a rearrangement of ions around the surface. This reordering is caused by electrostatic interactions, and is known as the electrical double layer (EDL)¹⁴³. The electrostatic potential of the EDL can be calculated by integrating the 1-D Poisson equation of the charge density along z-direction¹⁴⁴:

$$\frac{\partial^2 \phi(z)}{\partial z^2} = -\frac{\rho_q(z)}{\epsilon_0} \quad (4.5)$$

where ϕ is the electrostatic potential, ϵ_0 is the vacuum permittivity, and $\rho_q(z)$ is the charge density perpendicular to electrode (z-cross section).

We applied the same charge densities on the electrode surface for all systems. Figure 4.8 presents the potential profiles close to the negative electrode relative to the bulk potential, which is set to 0 V. The answer of each system to the electric field results in different potentials, however all of them are below the limit value where the fixed charge method gives reliable data (≤ 4 V)⁷⁰. The details of the charge density ($\rho_q(z)$) and the electric field ($E(z)$) profile are provided in the Supporting Information.

Figure 4.8 (a), (b), and (c) shows the oscillatory potential across the EDL (≤ 15 Å) for gold/DMSO, graphene/DMSO, and graphene/TEGDME systems, respectively. The electrolyte rearrangement when it is interacting to the electrode in presence or absence of an electrical charge creates this potential profile. This oscillation near the electrode surface is due to the electrolyte/electrode Coulombic interactions.

Similar potential profiles are observed for systems with DMSO solvent using both electrodes (Fig. 4.8 (a) and (b)). Regarding TEGDME, higher potentials are noticed (Fig. 4.8 (c)). These results indicate that solvent has a major role on the potential profile. Additionally, only for TEGDME we see the presence of oscillation at bulk region (≥ 15 Å). The main reason for this is the higher viscosity of this solvent which imposes higher standard deviations associated with these results (see previous discussion).

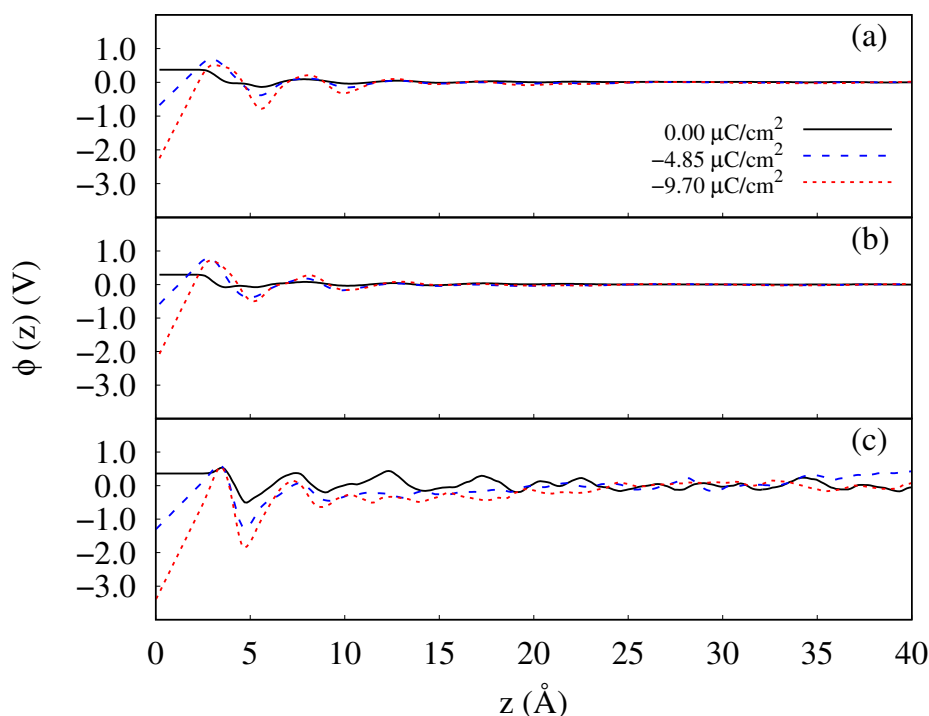


Figure 4.8: Potential profiles near the left electrode (negative) increasing the charge density (the bulk was set to 0 V): (a) at DMSO solvent and gold electrode, (b) at DMSO solvent and graphene electrode, and (c) at TEGDME solvent and graphene electrode.

From results of electrostatic potential profiles, we calculated the voltage drop variation ($\phi - \phi_z$) as a function of surface charge (σ), considering neutral surface case as a reference (the potential of zero charge or PZC (ϕ_z)). The PZC for DMSO/gold, DMSO/graphene, and TEGDME/graphene are 0.29 V, 0.27 V, and 0.44 V, respectively. These results express the higher affinity of the surface with positively charged atoms of solvents and with Li^{+74} . As comparison, the PZC of LiPF_6 in carbonated solvents using graphene electrode ranges from -0.28 to -0.10 V^{74,93,138}.

Figure 4.9 displays the voltage drop as a function of surface charge density (left y axis). It also shows the amount of Li^+ adsorbed in the first layer with the increase of surface charge density (right y axis). The percentage of Li^+ adsorbed was calculated integrating the first Li^+ layer, considering as cutoff distance the minimum of this peak. The analogous potential drop of DMSO systems corroborates the idea that electrostatic potential is only impacted by the solvent characteristics. Considering the Li^+ behavior in all systems, we see similar profiles on gold/DMSO and graphene/TEGDME compositions. Moreover, in graphene/DMSO system the amount of Li^+ adsorbed presents a monotonic increase with the charge increases. It suggests that EDL charge distribution is not contributing to Li^+ adsorption on the electrode. Boyer *et al*¹³⁸ also reported an increase of the Li^+ adsorbed to the electrode with an increase of surface charge density in carbonated solvent system at graphite electrode.

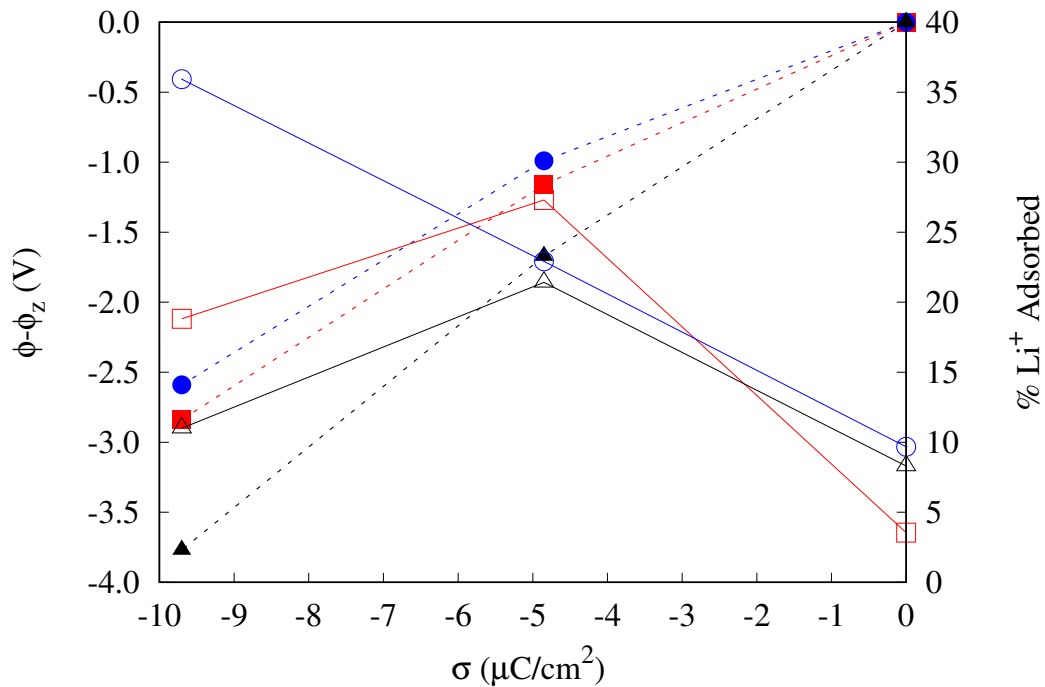


Figure 4.9: Voltage drop ($\phi - \phi_z$) between electrode and electrolyte as a function of the electrode surface charge density (σ) (left y axis). The amount of Li^+ adsorbed (%) in the first layer at electrode surface as a function of the electrode surface charge density (σ) (right y axis). Filled symbols and dashed lines represent the voltage drop. Opened symbols and solid lines represent the % of Li^+ adsorbed. Red square - DMSO solvent and gold electrode; blue circle - DMSO solvent and graphene electrode; black triangle - TEGDME solvent and graphene electrode.

The results of potential drop shown in Figure 4.9 appears to have a linear trend. The linear fitting of results shown in Figure 4.9 to Equation 4.6 gives the differential capacitance of the electrical double layer formed at the interface:

$$C_{\text{EDL}} = \frac{d\sigma}{d(\phi - \phi_z)} \quad (4.6)$$

where C_{EDL} is differential capacitance, σ is the surface charge density, and $(\phi - \phi_z)$ is the voltage drop. Capacitance is a measure of the storage capacity of the EDL in a non-Faradaic system^{131,138}. Even though redox reactions are present in a Li-air battery, the analysis of EDL capacitance without considering the redox reactions may still enhance our understanding about impedance caused by the electrolyte at the electrode.

The results of capacitance are presented in Table 4.2. Similar capacitance is observed for DMSO in gold electrode and graphene electrode systems. The slight difference noticed between them can be explained by DMSO reordering in graphene (Fig. 4.5 (c)). TEGDME system presents the lower capacity, indicating that the electrode surface is overcrowded and saturated by the solvent due its high viscosity. This can lead to a poor charge/discharge performance on a real system. For LiPF_6 in composition with EC/DMC in graphite electrode the C_{EDL} ranges

from 4-7 $\mu\text{F}\cdot\text{cm}^{-2}$ ^{274,138}.

Table 4.2: Differential capacitance of each electrical double layer

Solvent		
DMSO	DMSO	TEGDME
Electrode		
Gold	Graphene	Graphene
$C_{\text{EDL}} (\mu\text{F}\cdot\text{cm}^{-2})$		
3.41	3.74	2.57

4.4.4 Final remarks

According to the experimental findings of Bondue *et al.*¹⁴⁵, the oxygen reduction reaction (ORR) in Li-air battery is highly affected by the electrode material in presence of DMSO solvent. The authors observed that ORR takes place at inner sphere, close to the electrode, and the rate of ORR evolution changes according to electrode material, suggesting a relation between electrical double layer formation and ORR reaction pathway and rate. Our calculations have shown that local concentration profiles and Li^+ adsorption at the electrode surface are both influenced by the electrode material when DMSO is the solvent. The DMSO ordering at different electrode materials was also impacted. Even having insignificant influence of electrode material over the EDL in our calculations, the amount of Li^+ at the interface and the solvent behavior may be correlated to the different ORR mechanisms suggested by Bondue *et al.*¹⁴⁵.

Furthermore, Laoire *et al.*²⁰ claim that solvent impacts the by-products formation and reversibility of Li-air batteries. According to them, the complex formed by $[\text{Li}^+(\text{solvent})_n\text{-O}_2^-]$ is more stable in high donor number (DN) solvents (such as DMSO) than in low DN solvents (like TEGDME). This means that in DMSO the high complex stability leads to a reversible oxygen reduction (O_2/O_2^-), whereas in TEGDME it rapidly reduces from O_2 to O_2^{2-} . Our calculations have shown that solvation structures close to the electrode surface are different in DMSO and TEGDME solvents with graphene electrode. This may impact the $[\text{Li}^+(\text{solvent})_n\text{-O}_2^-]$ complex stability. Since five TEGDME oxygens are coordinated with Li^+ , the coordination of O_2^- can be difficult to maintain, making it unstable. Additionally, TEGDME shields the electrode and increases the impedance of the system, which can contribute to the lower stability of the intermediate products. The free energy profiles also corroborate the higher energy barriers for Li^+ to be adsorbed on the electrode surface in this solvent compared to DMSO solvent.

Johnson *et al.*⁵ concluded that reaction can take place at the electrolyte solution or at electrode surface depends on the applied potential and the DN of the solvent. The dominance of Li_2O_2 species in high DN solvent solution is attributed to the high solubility of LiO_2 intermediate in this solution when applying high potentials on the electrode (~ 3 V). Our results

have shown that the increase of surface charge density leads to a higher Li^+ concentration near the electrode when DMSO is the solvent compared to TEGDME. The high Li^+ availability in conjunction with its solvation complex structure in DMSO may contribute to the intermediate stability, which impacts the reactions reversibility. Nevertheless, according to the authors of the experimental study⁵, in low DN solvents, even applying high potentials, the cell had products accumulation at the surface, leading to a rapid battery failure. Our results presented a smaller distance between the first adsorbed layer of Li^+ and the electrode in TEGDME compared to DMSO (Fig. 4.7). It may explain the preference for the surface reaction pathway described by Johnson *et al.*⁵ for low DN solvents such as TEGDME. In addition to this, our calculations have shown that an increase of the electric field in TEGDME system creates a high concentration of solvent close to the electrode, which increases its impedance, as shown by C_{DL} values. This behavior can cause a low mobility of O_2 and Li^+ in the electrolyte. It decreases the mass flux that reaches the electrode, therefore directly influences the reaction rates and pathways.

Trahan *et al.*¹⁴⁶ also observed that ORR reaction takes place close to electrode (inner Helmholtz) or beyond the double layer (outer Helmholtz), which is determined by the catalyst (electrode composition) and solvent type. In carbon electrodes, with high DN solvents, the reaction occurs out of the electrical double layer, and it is independent of catalyst. On the other hand, with low DN solvents, the reaction befalls in the inner Helmholtz and it is only possible in presence of catalysts. In our simulations, regarding DMSO (a high DN solvent), the distance to Li^+ approach the surface is higher than in TEGDME (a low DN solvent). Furthermore, the energy penalties associate to TEGDME are higher than to DMSO (Fig. 4.7). Those findings agree with the theory of an inner/outer Helmholtz pathway being a function of solvent DN. For TEGDME, the adsorption of O_2 and its reduction products at electrode surface is possible in presence of catalyst. This adsorption contributes to the $[\text{Li}^+(\text{TEGDME})_n-\text{O}_2^-]$ complex formation, which increases the battery stability, protects the oxygen from reacting with the solvent and generates side products¹⁴⁶. Our calculations have shown that Li^+ solvation shell in TEGDME is composed roughly by five oxygen. Hence, the $[\text{Li}^+(\text{TEGDME})_5-\text{O}_2^-]$ stability may be difficult to achieve. The catalysts creates active areas where this process can be facilitated.

4.5 Conclusion

Molecular dynamics simulations were used to investigate the behavior at the electrode/electrolyte interface of three systems subjected to different surface charge densities. The studied electrode/electrolyte pairs were: gold electrode with LiPF_6 in DMSO, graphene electrode with LiPF_6 in DMSO, and graphene electrode with LiPF_6 in TEGDME. All electrolyte solutions are $1 \text{ mol}\cdot\text{kg}^{-1}$ for the salt. From the interfacial electrolyte structure with respect

of surface charge, we evaluated the local molecule/ion number density distributions, the Li^+ solvation and its relation with DMSO ordering, the voltage drop across the system, the capacitance of the electrical double layer, and the free energy penalties associated with Li^+ motion from the bulk to the interface region.

Our results have shown that Li^+ local concentration distribution at interface depends on the electrode material and solvent type. Its solvation, in case of DMSO being the solvent, is mainly influenced by the electrode type, which in turn is connected with the DMSO interfacial ordering. When TEGDME is the solvent, a high shield effect over the electrode is observed, characterized by the low capacitance of the electrical double layer, as well as the higher penalties for Li^+ mobility across the system. Hence, the electrical double layer is highly impacted by the solvent's nature. The amount of Li^+ adsorbed at the electrode surface suggests that electrode and solvent may have a coupled effect, since the results have shown similar behaviors between gold/DMSO and graphene/TEGDME pairs.

The comparison of our findings with experimental data from the literature for Li-air systems shows that a deeper understanding of interfacial structures at molecular level may provide auxiliary information to elucidate reaction pathways and system behavior under the discharging process of typical Li-air systems.

4.6 Acknowledgement

We thank the Center for Research Computing (CRC) at the University of Notre Dame for the computational resources, and the Brazilian agencies CNPq (Reference Number 203393/2018-0) and CAPES (Finance Code 001) for the financial support. This work was supported by FAPESP grant 2017/11958-1, and Shell, and the strategic importance of the support given by ANP (Brazil's National Oil, Natural Gas and Biofuels Agency) through the R&D levy regulations. LFMF acknowledges the support from the São Paulo Research Foundation (FAPESP) grant no. 2018/02713-8. YZ and EJM acknowledge the support from the U.S. Department of Energy, Office of Science, Basic Energy Sciences, Joint Center for Energy Storage Research under Contract No. DE-AC02-06CH11357.

Chapter 5

Discussion

As evidenced in the literature review (Chap. 2), there are several issues that need to be solved to project a viable commercial device. In order to overcome those questions the experimental approach have already been extensively applied as presented in Chapters 2, 3, and 4. Furthermore, the molecular simulation appears as a good tool to improve the understanding of battery, one it permits to study the system variables and their interplay in more details. Using simulation we can study the role of each battery part such as solvent, salt, electrode material, electric field etc. The system's complexity imposes a barrier to develop experimentally this type of study.

In this thesis two projects were developed. Both tried to bring some light on how the reaction mechanics can be affected by variables such as: anion, solvent, electrode material, and electric charge.

To gain deeper understanding of anion impact on electrolyte properties in a DMSO-based electrolyte, equilibrium molecular simulation (EMD) were employed. The EMD method was a suitable option because of the low viscosity of simulated systems as presented in Chapter 3. To calculate the transport properties was applied Green-Kubo which presented good performance. A carefully design of the EMD simulation and sampling data was used (Chap. 2). Similar motion with different solvation of Li^+ were noticed. Based on experimental data from literature concerning anion's impact on reaction mechanisms a great discussion was proposed. The findings presented in Chapter 3 enhances the literature around the impact of anion shape in the battery operation.

Moving a step forward in the study of the lithium-air battery, we performed confined simulation. To mimic the real device we simulate two parallel plates filled with electrolyte such as double-layer capacitors. The approach used to simulate this system was the fixed charge method. Even though, the constant potential method being more robust to this type of simulation, the high computational cost along with particular characteristics of our system led

us to believe that FCM was a better fit. Since the experimental set is run at low potentials and in our model we considered flat plates, the FCM technique was able to capture the electrolyte behavior (Chap. 2). Additionally, in lithium-air system unlike double-layer capacitors, reactions take place at the electrode/electrolyte interface. Hence, we were not properly simulating the real device, leading us to consider that this method was sturdy enough to give insights about the battery nature during discharge. Our simulation findings alongside with experimental data from literature showed the impact of electrode material and solvent donor number over the system. The Li^+ behavior was associated with the interaction of aforementioned variables and their impact over reaction mechanisms.

The findings reached out in both projects developed in this thesis pave a way for optimize the selection of materials for li-air battery. Applying MD simulation of bulk and confined systems it is possible to test a great amount of materials and these techniques can work as a first scan of materials suitable to this application.

Chapter 6

Conclusions and future work

6.1 Conclusions

The reactions mechanics appears to be affected by the selection of solvent, lithium salt, electrode material and its morphology, and the operational conditions. The increase of current and the decrease of overpotential between discharge/charge cycles are related with the formed reaction products and their decomposition. The literature has shown that an optimized selection of electrolyte composition (solvent and anion) along with the design of porous materials for electrode are main factors that need to be elucidated to achieve high capacities and capabilities during battery operation.

Aiming to study the impact of anion shape over transport and structural behavior of the electrolyte we developed EMD simulations of two lithium salts: LiPF_6 and LiPyr both dissolved in DMSO. We analysed different molalities and temperatures. The calculation of density, viscosity, self-diffusivity and conductivity were developed, from these results the Walden plot was done. Besides the dynamics analysis of the systems the solvation structure of Li^+ was also evaluated. Surprisingly, similar transport was observed for Li^+ in both systems, however different solvation structures were revealed. Even presenting analogous transference number, the structure of the solvation shell has a strong impact on the stabilization of intermediate reaction product (LiO_2) directly impacting over the discharge reaction mechanism.

With the goal of comprehending the electrolyte behavior close to the electrode surface during discharge we also run confined simulations. In this research step we evaluated two electrodes: gold and graphene; and two solvents: DMSO and TEGDME, which were combined in three different systems: gold/ LiPF_6 in DMSO, graphene/ LiPF_6 in DMSO, and graphene/ LiPF_6 in TEGDME. Surface charge densities were applied in all simulations mimicking the battery discharge process. Variables including concentration distribution profiles, DMSO organization, Li^+ solvation and free energy, and double layer capacitance were

calculated. The main conclusion of this work is that both variables play an important role on the system behavior. Based on the analysis of experimental findings from literature and the results presented in this work it seems that a synergistic effect of those variables might be considered in the battery project. Therefore, this result can help to improve the reaction cycling performance.

As a general conclusion this doctoral contributed to a better understanding of the role of fundamental variables in Li-air batteries. Macroscopic scale experiments suffer with the device complex operation and it is impossible to account for the impact of each variable on the system. The molecular dynamics simulation appears as a good tool to deeply comprehend the molecular phenomena in order to provide answers to experimentalists improve the real battery. The results acquired in this doctoral contributed as an auxiliary guidance to our group in the construction of novel Li-air cells configurations.

6.2 Future work

The complexity and hurdles of this promising technology opens several opportunities to the continuity of this work. Below it is summarized some suggestions for future enthusiasts of Li-air battery and MD simulation:

- Increasing the research around bulk simulation with inclusion of more types of solvents, anions, and mixture of them.
- Designing of electrodes with functional groups and/or decorated with catalysts to create a better representation of real electrodes.
- Implementation of the potential charge method (PCM) to evaluate its performance in Li-air typical systems.
- Parametrization of polarizable force fields for utilization in bulk and confined simulation approaches. It may give the opportunity to simulate systems with high concentration.

References

- [1] U. S. E. P. Agency, “Greenhouse Gas Inventory Data Explorer.” <https://cfpub.epa.gov/ghgdata/inventoryexplorer/>. Accessed 27 May 2020.
- [2] E. Parliament, “CO₂ emissions from cars: facts and figures (infographics).” <https://www.europarl.europa.eu/news/en/headlines/society/20190313STO31218/co2-emissions-from-cars-facts-and-figures-infographics>. Accessed 27 May 2020.
- [3] Nissan, “NOVO NISSAN LEAF.” <https://www.nissan.com.br/veiculos/modelos/leaf/autonomia-recarga.html>. Accessed 10 June 2020.
- [4] G. Girishkumar, B. McCloskey, A. C. Luntz, S. Swanson, and W. Wilcke, “Lithium-air battery: Promise and challenges,” *J. Phys. Chem. Lett.*, vol. 1, no. 14, pp. 2193–2203, 2010.
- [5] L. Johnson, C. Li, Z. Liu, Y. Chen, S. A. Freunberger, P. C. Ashok, B. B. Praveen, K. Dholakia, J. M. Tarascon, and P. G. Bruce, “The role of LiO₂ solubility in O₂ reduction in aprotic solvents and its consequences for Li-O₂ batteries,” *Nat. Chem.*, vol. 6, no. 12, pp. 1091–1099, 2014.
- [6] L. de Pablo, J. J. Segovia, A. Martín, M. C. Martín, and M. D. Bermejo, “Determination of density, viscosity and vapor pressures of mixtures of dimethyl sulfoxide + 1-allyl-3-methylimidazolium chloride at atmospheric pressure,” *J. Chem. Thermodyn.*, vol. 123, pp. 185–194, 2018.
- [7] M. S. Alam, B. Ashokkumar, and A. M. Siddiq, “The density, dynamic viscosity and kinematic viscosity of protic and aprotic polar solvent (pure and mixed) systems: An experimental and theoretical insight of thermophysical properties,” *J. Mol. Liq.*, vol. 281, pp. 584–597, 2019.
- [8] N. Kumar and J. M. Seminario, “Lithium-ion model behavior in an ethylene carbonate electrolyte using molecular dynamics,” *J. Phys. Chem. C*, vol. 120, no. 30, pp. 16322–16332, 2016.

- [9] M. Morita, F. Tachihara, and Y. Matsuda, "Dimethyl sulfoxide-based electrolytes for rechargeable lithium batteries," *Electrochim. Acta*, vol. 32, no. 2, pp. 299–305, 1987.
- [10] Y. Yamada, Y. Takazawa, K. Miyazaki, and T. Abe, "Electrochemical lithium intercalation into graphite in dimethyl sulfoxide-based electrolytes: Effect of solvation structure of lithium ion," *J. Phys. Chem. C*, vol. 114, no. 26, pp. 11680–11685, 2010.
- [11] M. Takeuchi, Y. Kameda, Y. Umebayashi, S. Ogawa, T. Sonoda, S. ichi Ishiguro, M. Fujita, and M. Sano, "Ion-ion interactions of LiPF_6 and LiBF_4 in propylene carbonate solutions," *J. Mol. Liq.*, vol. 148, no. 2-3, pp. 99–108, 2009.
- [12] K. D. Fong, J. Self, K. M. Diederichsen, B. M. Wood, B. D. McCloskey, and K. A. Persson, "Ion Transport and the True Transference Number in Nonaqueous Polyelectrolyte Solutions for Lithium Ion Batteries," *ACS Cent. Sci.*, vol. 5, no. 7, pp. 1250–1260, 2019.
- [13] A. V. Sergeev, A. V. Chertovich, D. M. Itkis, A. Sen, A. Gross, and A. R. Khokhlov, "Electrode/Electrolyte Interface in the Li-O_2 Battery: Insight from Molecular Dynamics Study," *J. Phys. Chem. C*, vol. 121, no. 27, pp. 14463–14469, 2017.
- [14] N. S. Barbosa, Y. Zhang, E. R. Lima, F. W. Tavares, and E. J. Maginn, "Development of an AMBER-compatible transferable force field for poly(ethylene glycol) ethers (glymes)," *J. Mol. Model.*, vol. 23, no. 6, 2017.
- [15] J. Poliscanova and Z. Kovács, "The end of the fossil fuel car is on the eu agenda." <https://www.transportenvironment.org/news/end-fossil-fuel-car-eu-agenda>. Accessed 10 June 2020.
- [16] P. G. Bruce, S. A. Freunberger, L. J. Hardwick, and J. M. Tarascon, "Li- O_2 and Li-S batteries with high energy storage," *Nat. Mater.*, vol. 11, no. 1, pp. 19–29, 2012.
- [17] F. S. Gittleson, R. C. Sekol, G. Doubek, M. Linardi, and A. D. Taylor, "Catalyst and electrolyte synergy in Li-O_2 batteries," *Phys. Chem. Chem. Phys.*, vol. 16, no. 7, p. 3230, 2014.
- [18] C. M. Burke, V. Pande, A. Khetan, V. Viswanathan, and B. D. McCloskey, "Enhancing electrochemical intermediate solvation through electrolyte anion selection to increase nonaqueous Li-O_2 battery capacity," *Proc. Natl. Acad. Sci. U.S.A.*, vol. 112, no. 30, pp. 9293–9298, 2015.
- [19] J. Lindberg, B. Endródi, G. Åvall, P. Johansson, A. Cornell, and G. Lindbergh, "Li Salt Anion Effect on O_2 Solubility in an Li-O_2 Battery," *J. Phys. Chem. C*, vol. 122, no. 4, pp. 1913–1920, 2018.

- [20] C. Laoire, S. Mukerjee, K. M. Abraham, E. J. Plichta, and M. A. Hendrickson, "Influence of Nonaqueous Solvents on the Electrochemistry of Oxygen in the Rechargeable Lithium-Air Battery," *J. Phys. Chem. C*, vol. 114, pp. 9178–9186, 2010.
- [21] Z. Peng, S. A. Freunberger, Y. Chen, and P. G. Bruce, "A reversible and higher-rate Li-O₂ battery," *Science*, vol. 337, no. 6094, pp. 563–566, 2012.
- [22] C. Liu and S. Ye, "In Situ Atomic Force Microscopy (AFM) Study of Oxygen Reduction Reaction on a Gold Electrode Surface in a Dimethyl Sulfoxide (DMSO)-Based Electrolyte Solution," *J. Phys. Chem. C*, vol. 120, no. 44, pp. 25246–25255, 2016.
- [23] M. Christy, A. Arul, A. Zahoor, K. U. Moon, M. Y. Oh, A. M. Stephan, and K. S. Nahm, "Role of solvents on the oxygen reduction and evolution of rechargeable Li-O₂ battery," *J. Power Sources*, vol. 342, pp. 825–835, 2017.
- [24] M. Augustin, P. E. Vullum, F. Vullum-Bruer, and A. M. Svensson, "Inside the electrode: Looking at cycling products in Li/O₂ batteries," *J. Power Sources*, vol. 414, no. December 2018, pp. 130–140, 2019.
- [25] H. G. Jung, J. Hassoun, J. B. Park, Y. K. Sun, and B. Scrosati, "An improved high-performance lithium-air battery," *Nat. Chem.*, vol. 4, no. 7, pp. 579–585, 2012.
- [26] A. Dutta, K. Ito, and Y. Kubo, "Establishing the criteria and strategies to achieve high power during discharge of a Li-air battery," *J. Mater. Chem. A*, vol. 7, no. 40, pp. 23199–23207, 2019.
- [27] F. Marchini, S. Herrera, W. Torres, A. Y. Tesio, F. J. Williams, and E. J. Calvo, "Surface Study of Lithium-Air Battery Oxygen Cathodes in Different Solvent-Electrolyte pairs," *Langmuir*, vol. 31, no. 33, pp. 9236–9245, 2015.
- [28] R. E. Jones, D. K. Ward, F. S. Gittleson, and M. E. Foster, "Assessing electrolyte transport properties with molecular dynamics," *J. Electrochem. Soc.*, vol. 164, no. 6, pp. A1258–A1267, 2017.
- [29] S. Plimpton, "Fast Parallel Algorithms for Short-Range Molecular Dynamics," *J. Comput. Phys.*, vol. 117, no. 1, pp. 1–19, 1995.
- [30] W. Humphrey, A. Dalke, and K. Schulten, "Vmd: Visual molecular dynamics," *J. Mol. Graph.*, vol. 14, no. 1, pp. 33–38, 1996.
- [31] T. Williams, C. Kelley, and many others, "Gnuplot 5.2: an interactive plotting program." <http://gnuplot.sourceforge.net/>, November 2017.
- [32] "Inkscape 1.0: draw freely." <https://inkscape.org/>, May 2020.
- [33] B. van der Zander, J. Sundermeyer, D. Braun, T. Hoffmann, and many others, "Texstudio: Latex made comfortable." <https://www.texstudio.org/>, May 2020.

- [34] L. E. L. and T. K. C., “Anodic behavior of lithium in aqueous electrolytes: I. transient passivation,” *J. Electrochem. Soc.*, vol. 123, pp. 771–776, 1976.
- [35] L. E. L. and T. K. C., “Corrosion of lithium in aqueous electrolytes,” *J. Electrochem. Soc.*, vol. 124, pp. 850–855, 1977.
- [36] P. Tan, M. Liu, Z. Shao, and M. Ni, “Recent advances in perovskite oxides as electrode materials for nonaqueous lithium-oxygen batteries,” *Adv. Energy Mater.*, vol. 7, no. 13, p. 1602674, 2017.
- [37] E. A. Ticianelli and E. R. Gonzalez, *Eletroquímica: Princípios e Aplicações*. São Paulo: Edusp, 2013.
- [38] A. Cohen, “Tesla’s new lithium-ion patent brings company closer to promised 1 million-mile battery.” <https://www.forbes.com/sites/arielcohen/2020/12/30/teslas-new-lithium-ion-patent-brings-company-closer-to-promised-1-#41e53ab533e3>. Accessed 23 September 2020.
- [39] O. Yamamoto, “Introduction,” in *The Lithium Air Battery: Fundamentals* (N. Imanishi, A. C. Luntz, and P. Bruce, eds.), ch. 1, pp. 1–22, London: Springer, 2014.
- [40] J. S. Hummelshøj, J. Blomqvist, S. Datta, T. Vegge, J. Rossmeisl, K. S. Thygesen, A. C. Luntz, K. W. Jacobsen, and J. K. Nørskov, “Communications: Elementary oxygen electrode reactions in the aprotic Li-air battery,” *J. Chem. Phys.*, vol. 132, p. 71101, feb 2010.
- [41] J. S. Hummelshøj, A. C. Luntz, and J. K. Nørskov, “Theoretical evidence for low kinetic overpotentials in li-o₂ electrochemistry,” *J. Chem. Phys.*, vol. 138, no. 3, p. 034703, 2013.
- [42] A. Luntz, B. McCloskey, H. H. S. Gowda, and V. Viswanathan, “Cathode electrochemistry in nonaqueous lithium air batteries,” in *The Lithium Air Battery: Fundamentals* (N. Imanishi, A. C. Luntz, and P. Bruce, eds.), ch. 3, pp. 59–120, London: Springer, 2014.
- [43] C. O. Laoire, S. Mukerjee, K. M. Abraham, E. J. Plichta, and M. A. Hendrickson, “Elucidating the mechanism of oxygen reduction for lithium-air battery applications,” *J. Phys. Chem. C*, vol. 113, no. 46, pp. 20127–20134, 2009.
- [44] Z. Peng, S. A. Freunberger, L. J. Hardwick, Y. Chen, V. Giordani, F. Bardé, P. Novák, D. Graham, J. M. Tarascon, and P. G. Bruce, “Oxygen reactions in a non-aqueous Li⁺ electrolyte,” *Angew. Chem. Int. Ed.*, vol. 50, no. 28, pp. 6351–6355, 2011.

- [45] S. A. Freunberger, Y. Chen, F. Bardé, K. Takechi, F. Mizuno, and P. G. Bruce, "Nonaqueous electrolytes," in *The Lithium Air Battery: Fundamentals* (N. Imanishi, A. C. Luntz, and P. Bruce, eds.), ch. 2, pp. 23–58, London: Springer, 2014.
- [46] M. Balaish, A. Kraysberg, and Y. Ein-Eli, "A critical review on lithium-air battery electrolytes," *Phys. Chem. Chem. Phys.*, vol. 16, no. 7, pp. 2801–2822, 2014.
- [47] F. S. Gittleson, R. E. Jones, D. K. Ward, and M. E. Foster, "Oxygen solubility and transport in Li-air battery electrolytes: Establishing criteria and strategies for electrolyte design," *Energ. Environ. Sci.*, vol. 10, no. 5, pp. 1167–1179, 2017.
- [48] M. M. Ottakam Thotiyl, S. A. Freunberger, Z. Peng, Y. Chen, Z. Liu, and P. G. Bruce, "A stable cathode for the aprotic Li-O₂ battery," *Nat. Mater.*, vol. 12, no. 11, pp. 1050–1056, 2013.
- [49] M. M. Ottakam Thotiyl, S. A. Freunberger, Z. Peng, and P. G. Bruce, "The carbon electrode in nonaqueous Li-O₂ cells," *J. Am. Chem. Soc.*, vol. 135, no. 1, pp. 494–500, 2013.
- [50] M. Park, H. Sun, H. Lee, J. Lee, and J. Cho, "Lithium-air batteries: Survey on the current status and perspectives towards automotive applications from a Battery Industry Standpoint," *Adv. Energy Mater.*, vol. 2, no. 7, pp. 780–800, 2012.
- [51] N. Ding, S. W. Chien, T. S. Hor, R. Lum, Y. Zong, and Z. Liu, "Influence of carbon pore size on the discharge capacity of Li-O₂ batteries," *J. Mater. Chem. A*, vol. 2, no. 31, pp. 12433–12441, 2014.
- [52] S. R. Younesi, S. Urbonaitė, F. Björefors, and K. Edström, "Influence of the cathode porosity on the discharge performance of the lithium-oxygen battery," *J. Power Sources*, vol. 196, no. 22, pp. 9835–9838, 2011.
- [53] J. Read, "Characterization of the Lithium/Oxygen Organic Electrolyte Battery," *J. Electrochem. Soc.*, vol. 149, no. 9, p. A1190, 2002.
- [54] C. Tran, X. Q. Yang, and D. Qu, "Investigation of the gas-diffusion-electrode used as lithium/air cathode in non-aqueous electrolyte and the importance of carbon material porosity," *J. Power Sources*, vol. 195, no. 7, pp. 2057–2063, 2010.
- [55] S. B. Ma, D. J. Lee, V. Roev, D. Im, and S. G. Doo, "Effect of porosity on electrochemical properties of carbon materials as cathode for lithium-oxygen battery," *J. Power Sources*, vol. 244, pp. 494–498, 2013.
- [56] K. N. Jung, J. Kim, Y. Yamauchi, M. S. Park, J. W. Lee, and J. H. Kim, "Rechargeable lithium-air batteries: A perspective on the development of oxygen electrodes," *J. Mater. Chem. A*, vol. 4, no. 37, pp. 14050–14068, 2016.

- [57] M. P. Allen and D. J. Tildesley, *Computer Simulation of Liquids*. USA: Oxford University Press, Inc., 2nd ed., 2017.
- [58] D. Frenkel and B. Smit, *Understanding Molecular Simulation: From Algorithms to Applications*, vol. 1. San Diego: Academic Press, second ed., 2002.
- [59] D. McQuarrie, *Statistical mechanics*. Harper's chemistry series, Harper & Row, 1975.
- [60] P. T. Cummings and D. J. Evans, "Nonequilibrium Molecular Dynamics Approaches to Transport Properties and Non-Newtonian Fluid Rheology," *Ind. Eng. Chem. Res.*, vol. 31, no. 5, pp. 1237–1252, 1992.
- [61] E. J. Maginn, R. A. Messerly, D. J. Carlson, D. R. Roe, and J. R. Elliott, "Best Practices for Computing Transport Properties 1. Self-Diffusivity and Viscosity from Equilibrium Molecular Dynamics," *LiveCoMS*, vol. 1, no. 1, pp. 1–20, 2019.
- [62] E. Helfand, "Transport coefficients from dissipation in a canonical ensemble," *Phys. Rev.*, vol. 119, pp. 1–9, Jul 1960.
- [63] J. Ma, Z. Zhang, Y. Xiang, F. Cao, and H. Sun, "On the prediction of transport properties of ionic liquid using 1-n-butylmethylpyridinium tetrafluoroborate as an example," *Mol. Simulat.*, vol. 43, no. 18, pp. 1502–1512, 2017.
- [64] S. H. Lee and J. Kim, "Transport properties of bulk water at 243-550 K: a Comparative molecular dynamics simulation study using SPC/E, TIP4P, and TIP4P/2005 water models," *Mol. Phys.*, vol. 117, no. 14, pp. 1926–1933, 2019.
- [65] M. Brehm and B. Kirchner, "Travis - a free analyzer and visualizer for monte carlo and molecular dynamics trajectories," *J. Chem. Inf. Model.*, vol. 51, pp. 2007–2023, aug 2011.
- [66] N. Michaud-Agrawal, E. J. Denning, T. B. Woolf, and O. Beckstein, "Mdanalysis: a toolkit for the analysis of molecular dynamics simulations.," *J. Comput. Chem.*, vol. 32, pp. 2319–2327, jul 2011.
- [67] R. T. McGibbon, K. A. Beauchamp, M. P. Harrigan, C. Klein, J. M. Swails, C. X. Hernández, C. R. Schwantes, L.-P. Wang, T. J. Lane, and V. S. Pande, "Mdtraj: A modern open library for the analysis of molecular dynamics trajectories.," *Biophys. J.*, vol. 109, pp. 1528–1532, oct 2015.
- [68] M. T. Humbert, Y. Zhang, and E. J. Maginn, "PyLAT: Python LAMMPS Analysis Tools," *J. Chem. Inf. Model.*, vol. 59, no. 4, pp. 1301–1305, 2019.
- [69] S. K. Reed, P. A. Madden, and A. Papadopoulos, "Electrochemical charge transfer at a metallic electrode: A simulation study," *J. Chem. Phys.*, vol. 128, no. 12, 2008.

- [70] Z. Wang, Y. Yang, D. L. Olmsted, M. Asta, and B. B. Laird, "Evaluation of the constant potential method in simulating electric double-layer capacitors," *J. Chem. Phys.*, vol. 141, no. 18, 2014.
- [71] J. Vatamanu, O. Borodin, and G. D. Smith, "Molecular insights into the potential and temperature dependences of the differential capacitance of a room-temperature ionic liquid at graphite electrodes," *J. Am. Chem. Soc.*, vol. 132, no. 42, pp. 14825–14833, 2010.
- [72] C. Merlet, C. Péan, B. Rotenberg, P. A. Madden, P. Simon, and M. Salanne, "Simulating supercapacitors: Can we model electrodes as constant charge surfaces?," *J. Phys. Chem. Lett.*, vol. 4, no. 2, pp. 264–268, 2013.
- [73] J. Vatamanu, L. Cao, O. Borodin, D. Bedrov, and G. D. Smith, "On the influence of surface topography on the electric double layer structure and differential capacitance of graphite/ionic liquid interfaces," *J. Phys. Chem. Lett.*, vol. 2, no. 17, pp. 2267–2272, 2011.
- [74] J. Vatamanu, O. Borodin, and G. D. Smith, "Molecular dynamics simulation studies of the structure of a mixed carbonate/LiPF₆ electrolyte near graphite surface as a function of electrode potential," *J. Phys. Chem. C*, vol. 116, no. 1, pp. 1114–1121, 2012.
- [75] L. Xing, J. Vatamanu, O. Borodin, G. D. Smith, and D. Bedrov, "Electrode/electrolyte interface in sulfolane-based electrolytes for Li ion batteries: A molecular dynamics simulation study," *J. Phys. Chem. C*, vol. 116, no. 45, pp. 23871–23881, 2012.
- [76] A. Fang and A. Smolyanitsky, "Simulation Study of the Capacitance and Charging Mechanisms of Ionic Liquid Mixtures near Carbon Electrodes," *J. Phys. Chem. C*, vol. 123, no. 3, pp. 1610–1618, 2019.
- [77] D. J. Cole, P. K. Ang, and K. P. Loh, "Ion adsorption at the graphene/electrolyte interface," *J. Phys. Chem. Lett.*, vol. 2, no. 14, pp. 1799–1803, 2011.
- [78] T. Méndez-Morales, J. Carrete, M. Pérez-Rodríguez, Ó. Cabeza, L. J. Gallego, R. M. Lynden-Bell, and L. M. Varela, "Molecular dynamics simulations of the structure of the graphene-ionic liquid/alkali salt mixtures interface," *Phys. Chem. Chem. Phys.*, vol. 16, no. 26, pp. 13271–13278, 2014.
- [79] Y. Zhang, B. Dyatkin, and P. T. Cummings, "Molecular Investigation of Oxidized Graphene: Anatomy of the Double-Layer Structure and Ion Dynamics," *J. Phys. Chem. C*, vol. 123, no. 20, pp. 12583–12591, 2019.
- [80] K. M. Abraham and Z. Jiang, "A Polymer Electrolyte-Based Rechargeable Lithium/Oxygen Battery," *J. Electrochem. Soc.*, vol. 143, pp. 1–5, 1996.

- [81] Y. Li and J. Lu, “Metal-Air Batteries: will they be the future electrochemical energy storage device of choice?,” *ACS Energy Lett.*, vol. 2, pp. 1370–1377, 2017.
- [82] S. Han, “Structure and dynamics in the lithium solvation shell of nonaqueous electrolytes,” *Sci. Rep.*, vol. 9, no. 1, pp. 1–10, 2019.
- [83] J. Smiatek, A. Heuer, and M. Winter, “Properties of ion complexes and their impact on charge transport in organic solvent-based electrolyte solutions for lithium batteries: Insights from a theoretical perspective,” *Batteries*, vol. 4, no. 4, 2018.
- [84] K. Xu, “Electrolytes and interphases in Li-ion batteries and beyond,” *Chem. Rev.*, vol. 114, no. 23, pp. 11503–11618, 2014.
- [85] K. Xu, “Nonaqueous liquid electrolytes for lithium-based rechargeable batteries,” *Chem. Rev.*, vol. 104, no. 10, pp. 4303–4417, 2004.
- [86] O. Borodin, L. Suo, M. Gobet, X. Ren, F. Wang, A. Faraone, J. Peng, M. Olguin, M. Schroeder, M. S. Ding, E. Gobrogge, A. Von Wald Cresce, S. Munoz, J. A. Dura, S. Greenbaum, C. Wang, and K. Xu, “Liquid Structure with Nano-Heterogeneity Promotes Cationic Transport in Concentrated Electrolytes,” *ACS Nano*, vol. 11, no. 10, pp. 10462–10471, 2017.
- [87] A. Narayanan Kirshnamoorthy, K. Oldiges, M. Winter, A. Heuer, I. Cekic-Laskovic, C. Holm, and J. Smiatek, “Electrolyte solvents for high voltage lithium ion batteries: Ion correlation and specific anion effects in adiponitrile,” *Phys. Chem. Chem. Phys.*, vol. 20, no. 40, pp. 25701–25715, 2018.
- [88] T. M. Aminabhavi and B. Gopalakrishna, “Density, Viscosity, Refractive Index, and Speed of Sound in Aqueous Mixtures of *N,N*-Dimethylformamide, Dimethyl Sulfoxide, *N,N*-Dimethylacetamide, Acetonitrile, Ethylene Glycol, Diethylene Glycol, 1,4-Dioxane, Tetrahydrofuran, 2-Methoxyethanol, and 2-Ethoxyethanol at 298.15 K,” *J. Chem. Eng. Data*, vol. 40, pp. 856–861, 1995.
- [89] M. Elabyouki, D. Bahamon, M. Khaleel, and L. F. Vega, “Insights into the Transport Properties of Electrolyte Solutions in a Hierarchical Carbon Electrode by Molecular Dynamics Simulations,” *J. Phys. Chem. C*, vol. 123, pp. 27273–27285, 2019.
- [90] L. F. M. Franco, M. Castier, and I. G. Economou, “Diffusion in homogeneous and in inhomogeneous media: a new unified approach,” *J. Chem. Theory Comput.*, vol. 12, pp. 5247–5255, 2016.
- [91] I. N. Tsimpanogiannis, O. A. Moulton, L. F. M. Franco, M. B. M. Spera, M. Erdős, and I. G. Economou, “Self-diffusion coefficient of bulk and confined water: a critical review of classical molecular simulation studies,” *Mol. Sim.*, vol. 45, pp. 425–453, 2016.

- [92] M. L. Strader and S. E. Feller, "A flexible all-atom model of dimethyl sulfoxide for molecular dynamics simulations," *J. Phys. Chem. A*, vol. 106, no. 6, pp. 1074–1080, 2002.
- [93] R. Jorn, R. Kumar, D. P. Abraham, and G. A. Voth, "Atomistic modeling of the electrode-electrolyte interface in li-ion energy storage systems: Electrolyte structuring," *J. Phys. Chem. C*, vol. 117, no. 8, pp. 3747–3761, 2013.
- [94] H. Liu and E. Maginn, "Effect of ion structure on conductivity in lithium-doped ionic liquid electrolytes: A molecular dynamics study," *J. Chem. Phys.*, vol. 139, no. 11, p. 114508, 2013.
- [95] L. Martínez, R. Andrade, E. G. Birgin, and J. M. Martínez, "Packmol: A package for building initial configurations for molecular dynamics simulations.," *J. Comput. Chem.*, vol. 30, no. 13, pp. 2157–2164, 2009.
- [96] G. J. Martyna, D. J. Tobias, and M. L. Klein, "Constant pressure molecular dynamics algorithms," *J. Chem. Phys.*, vol. 101, no. 5, pp. 4177–4189, 1994.
- [97] W. Shinoda, M. Shiga, and M. Mikami, "Rapid estimation of elastic constants by molecular dynamics simulation under constant stress," *Phys. Rev. B*, vol. 69, p. 134103, Apr 2004.
- [98] M. Parrinello and A. Rahman, "Polymorphic transitions in single crystals: A new molecular dynamics method," *J. App. Phys.*, vol. 52, no. 12, pp. 7182–7190, 1981.
- [99] R. Hockney, *Computer simulation using particles*. Bristol England Philadelphia: A. Hilger, 1988.
- [100] Y. Zhang, A. Otani, and E. J. Maginn, "Reliable Viscosity Calculation from Equilibrium Molecular Dynamics Simulations: A Time Decomposition Method," *J. Chem. Theory Comput.*, vol. 11, no. 8, pp. 3537–3546, 2015.
- [101] M. S. Green, "Markoff Random Processes and the Statistical Mechanics of Time-Dependent Phenomena. II. Irreversible Processes in Fluids," *J. Chem. Phys.*, vol. 22, pp. 398–413, 1953.
- [102] R. Kubo, "Statistical-Mechanical Theory of Irreversible Processes. I. General Theory and Simple Applications to Magnetic and Conduction Problems," *J. Phys. Soc. Jpn.*, vol. 12, pp. 570–586, 1957.
- [103] B. L. Holian and D. J. Evans, "Shear viscosities away from the melting line: A comparison of equilibrium and nonequilibrium molecular dynamics," *J. Chem. Phys.*, vol. 78, no. 8, pp. 5147–5150, 1983.

- [104] B. Hess, "Determining the shear viscosity of model liquids from molecular dynamics simulations," *J. Chem. Phys.*, vol. 116, no. 1, pp. 209–217, 2002.
- [105] C. Rey-Castro and L. F. Vega, "Transport Properties of the Ionic Liquid 1-Ethyl-3-Methylimidazolium Chloride from Equilibrium Molecular Dynamics Simulation. The Effect of Temperature," *J. Phys. Chem. B*, vol. 110, pp. 14426–14435, jul 2006.
- [106] I. C. Yeh and G. Hummer, "System-size dependence of diffusion coefficients and viscosities from molecular dynamics simulations with periodic boundary conditions," *J. Phys. Chem. B*, vol. 108, no. 40, pp. 15873–15879, 2004.
- [107] B. Dünweg, "Molecular dynamics algorithms and hydrodynamic screening," *J. Chem. Phys.*, vol. 99, no. 9, pp. 6977–6982, 1993.
- [108] B. Dünweg and K. Kremer, "Molecular dynamics simulation of a polymer chain in solution," *J. Chem. Phys.*, vol. 99, no. 9, pp. 6983–6997, 1993.
- [109] H. Liu and E. Maginn, "A molecular dynamics investigation of the structural and dynamic properties of the ionic liquid 1-n-butyl-3-methylimidazolium bis(trifluoromethanesulfonyl) imide," *J. Chem. Phys.*, vol. 135, no. 12, pp. 1–16, 2011.
- [110] U. Weinert and E. A. Mason, "Generalized Nernst-Einstein relations for nonlinear transport coefficients," *Phys. Rev. A*, vol. 21, pp. 681–690, 1980.
- [111] J. A. Padró, J. Trullàs, and G. Sesé, "Computer simulation study of the dynamic cross-correlations in liquids," *Mol. Phys.*, vol. 72, pp. 1035–1049, 1991.
- [112] K. Harris, "Relations between the Fractional Stokes-Einstein and Nernst-Einstein Equations and Velocity Correlation Coefficients in Ionic Liquids and Molten Salts," *J. Phys. Chem. B*, vol. 114, pp. 9572–9577, 2010.
- [113] P. Walden, "Organic solutions- and ionisation means. iii. chapter: Internal friction and its connection with conductivity.," *Z. Phys. Chem.*, no. 55, pp. 207–249, 1906.
- [114] K. Harris, "On the Use of the Angell-Walden Equation To Determine the "Ionicity" of Molten Salts and Ionic Liquids," *J. Phys. Chem. B*, vol. 123, pp. 7014–7023, 2019.
- [115] C. Schreiner, S. Zugmann, R. Hartl, and H. J. Gores, "Fractional walden rule for ionic liquids: Examples from recent measurements and a critique of the so-called ideal KCl line for the walden plot," *J. Chem. Eng. Data*, vol. 55, no. 5, pp. 1784–1788, 2010.
- [116] W. Xu, E. I. Cooper, and C. A. Angell, "Ionic liquids: Ion mobilities, glass temperatures, and fragilities," *J. Phys. Chem. B*, vol. 107, no. 25, pp. 6170–6178, 2003.

- [117] I. Gunasekara, S. Mukerjee, E. J. Plichta, M. A. Hendrickson, and K. M. Abraham, "Microelectrode diagnostics of lithium-air batteries," *J. Electrochem. Soc.*, vol. 161, no. 3, pp. A381–A392, 2014.
- [118] A. Alsudairi, A. Lajami, I. Kendrick, S. Mukerjee, and A. K. M., "Correlating Ionic Conductivity, Oxygen Transport and ORR with Structure of Dialkylacetamide-Based Electrolytes for Lithium-Air Batteries," *J. Electrochem. Soc.*, vol. 166, pp. A305–A317, 2019.
- [119] N. Mozhzhukhina, M. P. Longinotti, H. R. Corti, and E. J. Calvo, "A conductivity study of preferential solvation of lithium ion in acetonitrile-dimethyl sulfoxide mixtures," *Electrochim. Acta*, vol. 154, pp. 456–461, 2015.
- [120] K. M. Diederichsen, E. J. McShane, and B. D. McCloskey, "Promising Routes to a High Li⁺ Transference Number Electrolyte for Lithium Ion Batteries," *ACS Energy Lett.*, vol. 2, no. 11, pp. 2563–2575, 2017.
- [121] V. S. Dilimon, C. Hwang, Y. G. Cho, J. Yang, H. D. Lim, K. Kang, S. J. Kang, and H. K. Song, "Superoxide stability for reversible Na-O₂ electrochemistry," *Sci. Rep.*, vol. 7, no. 1, pp. 1–10, 2017.
- [122] Y. Marcus, *Ions in Solution and their Solvation*. Hoboken: Wiley, 2015.
- [123] K. M. Abraham, "Electrolyte-Directed Reactions of the Oxygen Electrode in Lithium-Air Batteries," *J. Electrochem. Soc.*, vol. 162, no. 2, pp. A3021–A3031, 2015.
- [124] M. Schmeisser, P. Illner, R. Puchta, A. Zahl, and R. Van Eldik, "Gutmann donor and acceptor numbers for ionic liquids," *Chem. Eur. J.*, vol. 18, no. 35, pp. 10969–10982, 2012.
- [125] A. Kraytsberg and Y. Ein-Eli, "Review on Li-air batteries - Opportunities, limitations and perspective," *J. Power Sources*, vol. 196, no. 3, pp. 886–893, 2011.
- [126] J. Xiao, D. Wang, W. Xu, D. Wang, R. E. Williford, J. Liu, and J.-G. Zhang, "Optimization of Air Electrode for Li/Air Batteries," *J. Electrochem. Soc.*, vol. 157, no. 4, p. A487, 2010.
- [127] M. Balaish, J. W. Jung, I. D. Kim, and Y. Ein-Eli, "A Critical Review on Functionalization of Air-Cathodes for Nonaqueous Li-O₂ Batteries," *Adv. Funct. Mater.*, vol. 1808303, pp. 1–34, 2019.
- [128] J. W. Jung, S. H. Cho, J. S. Nam, and I. D. Kim, "Current and future cathode materials for non-aqueous Li-air (O₂) battery technology - A focused review," *Energy Storage Mater.*, vol. 24, no. June 2019, pp. 512–528, 2020.

- [129] S. Yang, P. He, and H. Zhou, "Research progresses on materials and electrode design towards key challenges of Li-air batteries," *Energy Storage Mater.*, vol. 13, no. August 2017, pp. 29–48, 2018.
- [130] D. Xu, Z. L. Wang, J. J. Xu, L. L. Zhang, and X. B. Zhang, "Novel DMSO-based electrolyte for high performance rechargeable Li-O₂ batteries," *ChemComm*, vol. 48, no. 55, pp. 6948–6950, 2012.
- [131] J. Vatamanu, O. Borodin, M. Olguin, G. Yushin, and D. Bedrov, "Charge storage at the nanoscale: Understanding the trends from the molecular scale perspective," *J. Phys. Chem. A*, vol. 5, no. 40, pp. 21049–21076, 2017.
- [132] S. A. Kislenco, I. S. Samoylov, and R. H. Amirov, "Molecular dynamics simulation of the electrochemical interface between a graphite surface and the ionic liquid [BMIM][PF₆]," *Phys. Chem. Chem. Phys.*, vol. 11, no. 27, pp. 5584–5590, 2009.
- [133] E. Paek, A. J. Pak, and G. S. Hwang, "A Computational Study of the Interfacial Structure and Capacitance of Graphene in [BMIM][PF₆] Ionic Liquid," *J. Electrochem. Soc.*, vol. 160, no. 1, pp. A1–A10, 2013.
- [134] L. B. Wright, P. M. Rodger, S. Corni, and T. R. Walsh, "GoIP-CHARMM: First-principles based force fields for the interaction of proteins with Au(111) and Au(100)," *J. Chem. Theory Comput.*, vol. 9, no. 3, pp. 1616–1630, 2013.
- [135] O. S. Lee and M. A. Carignano, "Exfoliation of Electrolyte-Intercalated Graphene: Molecular Dynamics Simulation Study," *J. Phys. Chem. C*, vol. 119, no. 33, pp. 19415–19422, 2015.
- [136] I. C. Yeh and M. L. Berkowitz, "Ewald summation for systems with slab geometry," *J. Chem. Phys.*, vol. 111, no. 7, pp. 3155–3162, 1999.
- [137] V. Ballenegger, A. Arnold, and J. J. Cerdà, "Simulations of non-neutral slab systems with long-range electrostatic interactions in two-dimensional periodic boundary conditions," *J. Chem. Phys.*, vol. 131, no. 9, 2009.
- [138] M. J. Boyer, L. Vilčiauskas, and G. S. Hwang, "Structure and Li⁺ ion transport in a mixed carbonate/LiPF₆ electrolyte near graphite electrode surfaces: A molecular dynamics study," *Phys. Chem. Chem. Phys.*, vol. 18, no. 40, pp. 27868–27876, 2016.
- [139] D. Kodama, M. Kanakubo, M. Kokubo, S. Hashimoto, H. Nanjo, and M. Kato, "Density, viscosity, and solubility of carbon dioxide in glymes," *Fluid Phase Equilibria*, vol. 302, no. 1, pp. 103 – 108, 2011.

- [140] J. Fiates, Y. Zhang, L. F. M. Franco, E. J. Maginn, and G. Doubek, "Impact of anion shape on Li^+ solvation and on transport properties for lithium–air batteries: a molecular dynamics study," *Phys. Chem. Chem. Phys.*, vol. 22, pp. 15842–15852, 2020.
- [141] M. S. Santos, L. F. M. Franco, M. Castier, and I. G. Economou, "Molecular dynamics simulation of n-alkanes and CO_2 confined by calcite nanopores," *Energy Fuels*, vol. 32, pp. 1934–1941, 2018.
- [142] Y. C. Lu, H. A. Gasteiger, M. C. Parent, V. Chiloyan, and Y. Shao-Horn, "The influence of catalysts on discharge and charge voltages of rechargeable Li-oxygen batteries," *Electrochem. Solid St.*, vol. 13, no. 6, 2010.
- [143] L. L. Zhang and X. S. Zhao, "Carbon-based materials as supercapacitor electrodes," *Chem. Soc. Rev.*, vol. 38, no. 9, pp. 2520–2531, 2009.
- [144] E. Spohr, "Molecular simulation of the electrochemical double layer," *Electrochim. Acta*, vol. 44, no. 11, pp. 1697–1705, 1999.
- [145] C. J. Bondue, P. Reinsberg, A. A. Abd-El-Latif, and H. Baltruschat, "Oxygen reduction and oxygen evolution in DMSO based electrolytes: The role of the electrocatalyst," *Phys. Chem. Chem. Phys.*, vol. 17, no. 38, pp. 25593–25606, 2015.
- [146] M. J. Trahan, I. Gunasekara, S. Mukerjee, E. J. Plichta, M. A. Hendrickson, and K. M. Abraham, "Solvent-Coupled Catalysis of the Oxygen Electrode Reactions in Lithium-Air Batteries," *J. Electrochem. Soc.*, vol. 161, no. 10, pp. A1706–A1715, 2014.
- [147] D. Alfè and M. J. Gillan, "First-principles calculation of transport coefficients," *Phys. Rev. Lett.*, vol. 81, no. 23, pp. 5161–5164, 1998.
- [148] O. Andreussi and N. Marzari, "Transport properties of room-temperature ionic liquids from classical molecular dynamics," *J. Chem. Phys.*, vol. 137, no. 4, p. 044508, 2012.
- [149] J. A. Templeton, R. E. Jones, J. W. Lee, J. A. Zimmerman, and B. M. Wong, "A long-range electric field solver for molecular dynamics based on atomistic-to-continuum modeling," *J. Chem. Theory Comput.*, vol. 7, no. 6, pp. 1736–1749, 2011.

Appendix A

Electronic supplementary information (ESI) for: Impact of anion shape on Li^+ solvation and on transport properties for lithium-air batteries: a molecular dynamics study[†]

Juliane Fiates^{a,b}, Yong Zhang^b, Luís F. M. Franco^a, Edward J. Maginn^b and Gustavo Doubek^a

^a *School of Chemical Engineering,
University of Campinas,
Campinas 13083-852, Brazil.*

^b *Department of Chemical and Biomolecular Engineering,
University of Notre Dame,
Notre Dame, Indiana 46556, USA.*

Dated: May 4, 2020

[†]It have already been published at Physical Chemistry Chemical Physics Journal (PCCP).
DOI:<https://doi.org/10.1039/D0CP00853B>. Reproduced by permission of the PCCP Owner Societies.

The information contained in this material is described as:

- Section A.1 comprises the time correlation functions for shear viscosity, self-diffusivity and ionic conductivity.
- Section A.2 presents the system size effect analyses on transport properties.
- Section A.3 has the information of structural arrangement for different molalities and temperatures.
- Section A.4 consists on simulation details of initial configurations, force fields and LAMMPS running files.

A.1 Time correlation functions

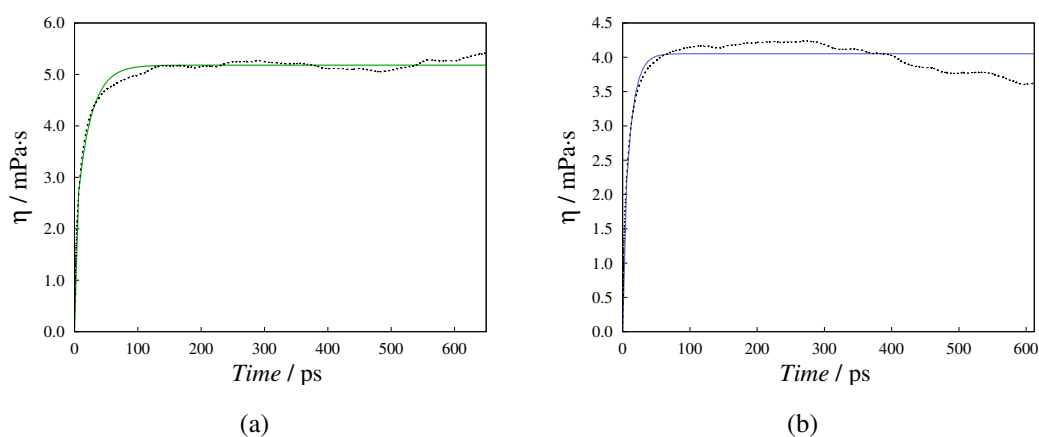


Figure A.1: The shear viscosity corresponding to the running integral (Eq. 2) averaged over 30 trajectories (dashed line) and the fitting empirical function (Eq. 3) (solid line) at $1 \text{ mol}\cdot\text{kg}^{-1}$ and 298 K for: (a) LiPF_6 , and (b) LiPyr .

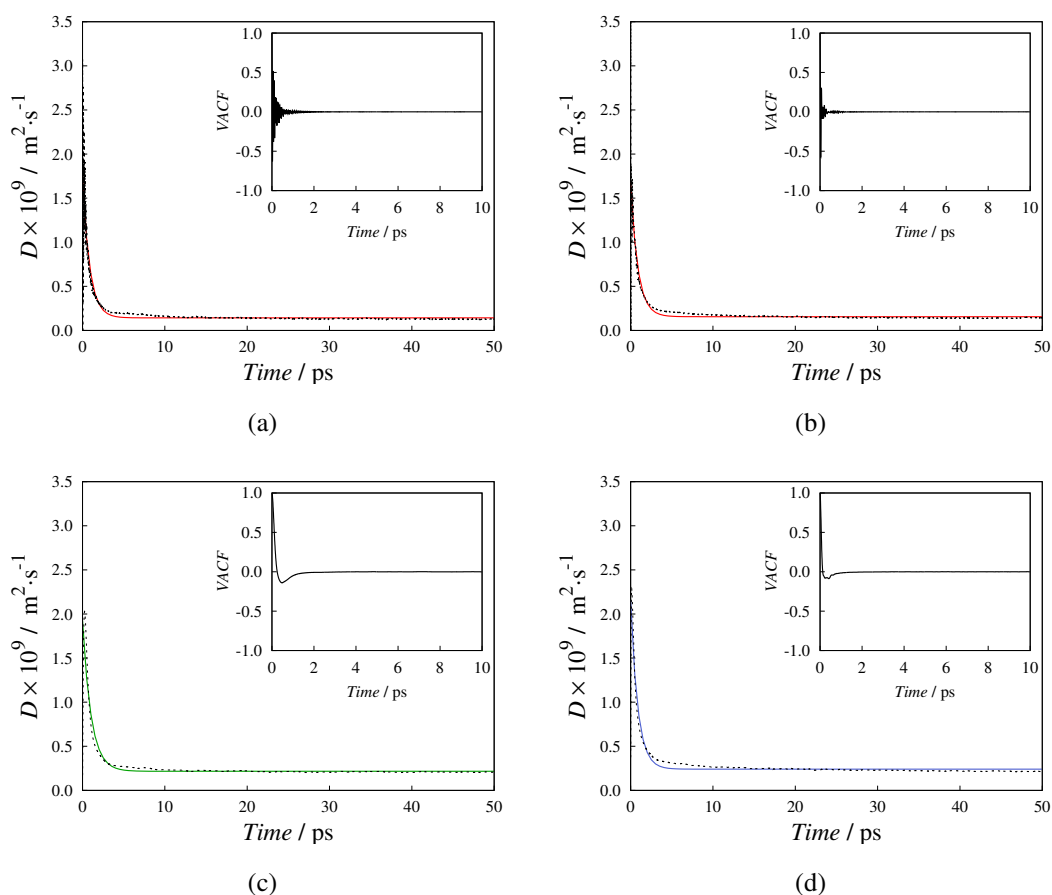


Figure A.2: Self-diffusion corresponding to the running integral (Eq. 6) averaged over 10 trajectories (dashed line) and the fitting empirical function (Eq. 7) (solid line) at $1 \text{ mol}\cdot\text{kg}^{-1}$ and 298 K for: (a) Li^+ in solution with PF_6^- , (b) Li^+ in solution with Pyr^- , (c) PF_6^- , and (d) Pyr^- . The insets show the normalized velocity autocorrelation function (VACF).

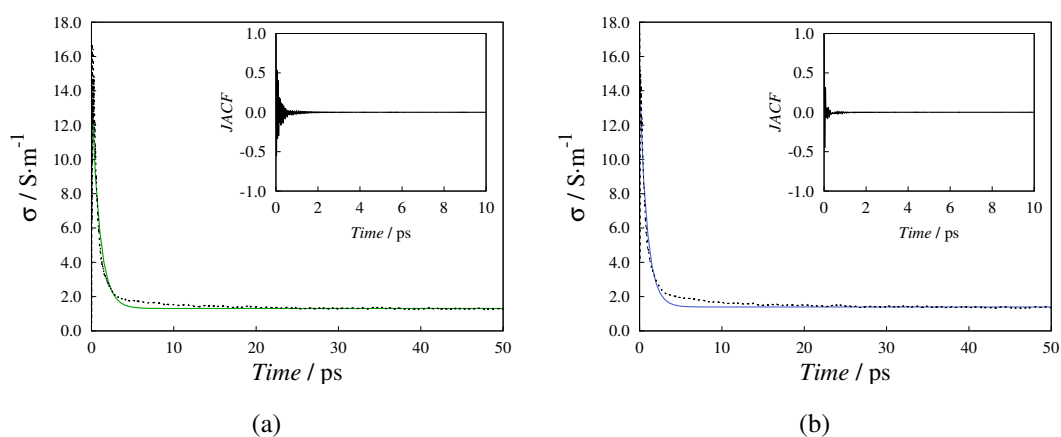


Figure A.3: Ionic conductivity corresponding to the running integral (Eq. 9) averaged over 10 trajectories (dashed line) and the fitting empirical function (analogous to Eq. 7) (solid line) at $1 \text{ mol}\cdot\text{kg}^{-1}$ and 298 K for: (a) LiPF_6 , and (b) LiPyr . The insets show the normalized electrical current autocorrelation function (JACF).

A.2 System size analysis

System size effect at collective properties must be taken into account in molecular simulations. Several authors have discussed such an effect considering error propagation and poor statistics caused by the influence of periodic boundary conditions in small box size and limited number of molecules^{58,106–108,147,148}.

Although larger system sizes improve the accuracy, they also increase the computational cost. To counterbalance computation cost and good accuracy of results, three set of systems were considered. We evaluated the system size effect on the self-diffusion coefficients and the ionic conductivities; viscosity seems to be unaffected by the system size^{100,105,106,147,148}. LiPF_6 and LiPyr in DMSO solutions with $1 \text{ mol}\cdot\text{kg}^{-1}$ at 298 K were simulated with the following number of lithium ions and number of DMSO molecules: 40/512, 60/768, and 80/1024 (the number of anions is equal to the number of lithium ions).

Figure C.4 (a) and (c) presents results of transport coefficients as a function of the inverse of number of cations. Even though we notice decrease of uncertainties for larger systems, almost the same average trend is observed for the value of each property. However, in order to increase the accuracy of self-diffusivity coefficient, we implemented the system-size correction (Eq. 9). Figure C.4 (b) illustrates the improvement on this property with correction when compared with larger systems.

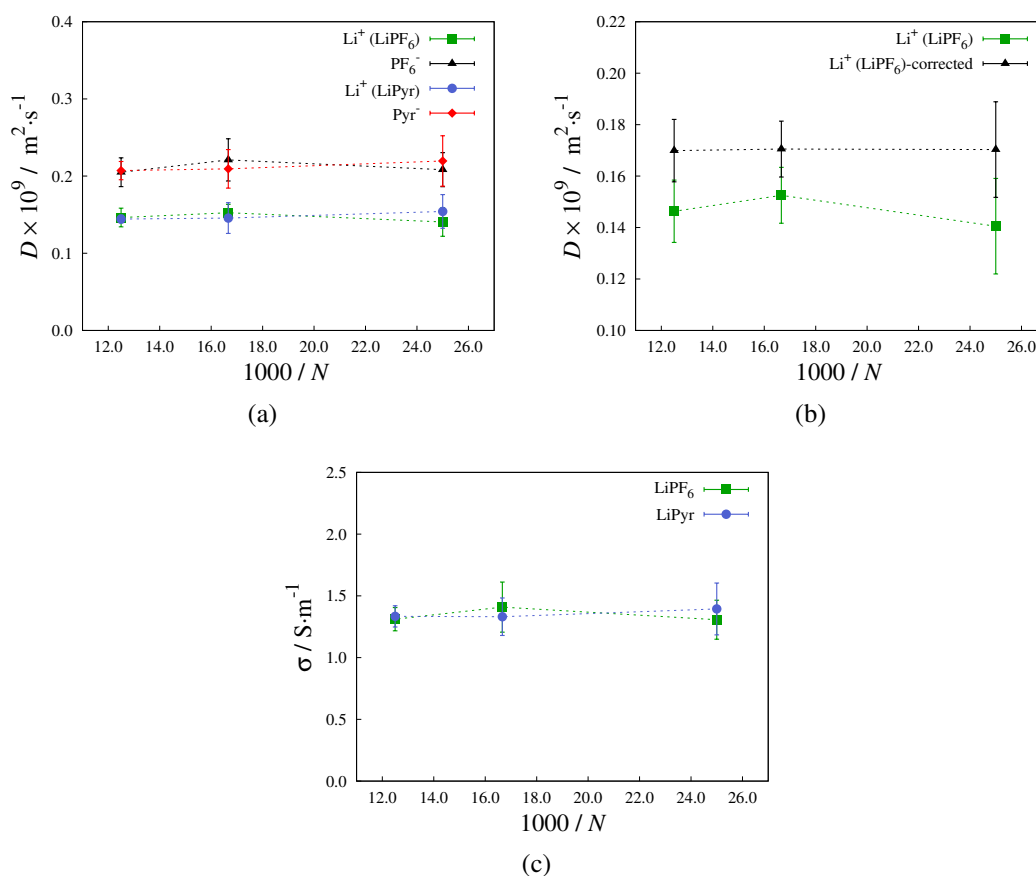


Figure A.4: System size effect on the transport properties of LiPF_6 in DMSO and LiPyr in DMSO both at $1 \text{ mol} \cdot \text{kg}^{-1}$ and 298 K: (a) Self-diffusion coefficients without size effect correction, (b) Self-diffusion coefficients of Li^+ of LiPF_6 in DMSO without correction and corrected, and (c) Ionic conductivity coefficients.

A.3 Structural arrangement

Table A.1: Coordination numbers of the first solvation shell for Li–O (DMSO), Li–F(PF₆) and Li–N(Pyr) at 1 atm for different salt molalities and at different temperatures.

Salt molality / mol·kg ⁻¹	Temperature / K			
	298			
$n_{\text{Li-O}}$ for LiPF ₆ in DMSO	4.00	3.91	3.83	3.74
$n_{\text{Li-F}}$ for LiPF ₆ in DMSO	0.01	0.09	0.19	0.29
$n_{\text{Li-O}}$ for LiPyr in DMSO	4.00	3.85	3.58	3.32
$n_{\text{Li-N}}$ for LiPyr in DMSO	0.44	0.58	0.70	0.87

Temperature / K	Salt molality / mol·kg ⁻¹		
	1.00		
$n_{\text{Li-O}}$ for LiPF ₆ in DMSO	298	330	360
$n_{\text{Li-O}}$ for LiPF ₆ in DMSO	3.74	3.93	3.99
$n_{\text{Li-F}}$ for LiPF ₆ in DMSO	0.29	0.08	0.01
$n_{\text{Li-O}}$ for LiPyr in DMSO	3.32	3.08	2.80
$n_{\text{Li-N}}$ for LiPyr in DMSO	0.87	1.00	1.14

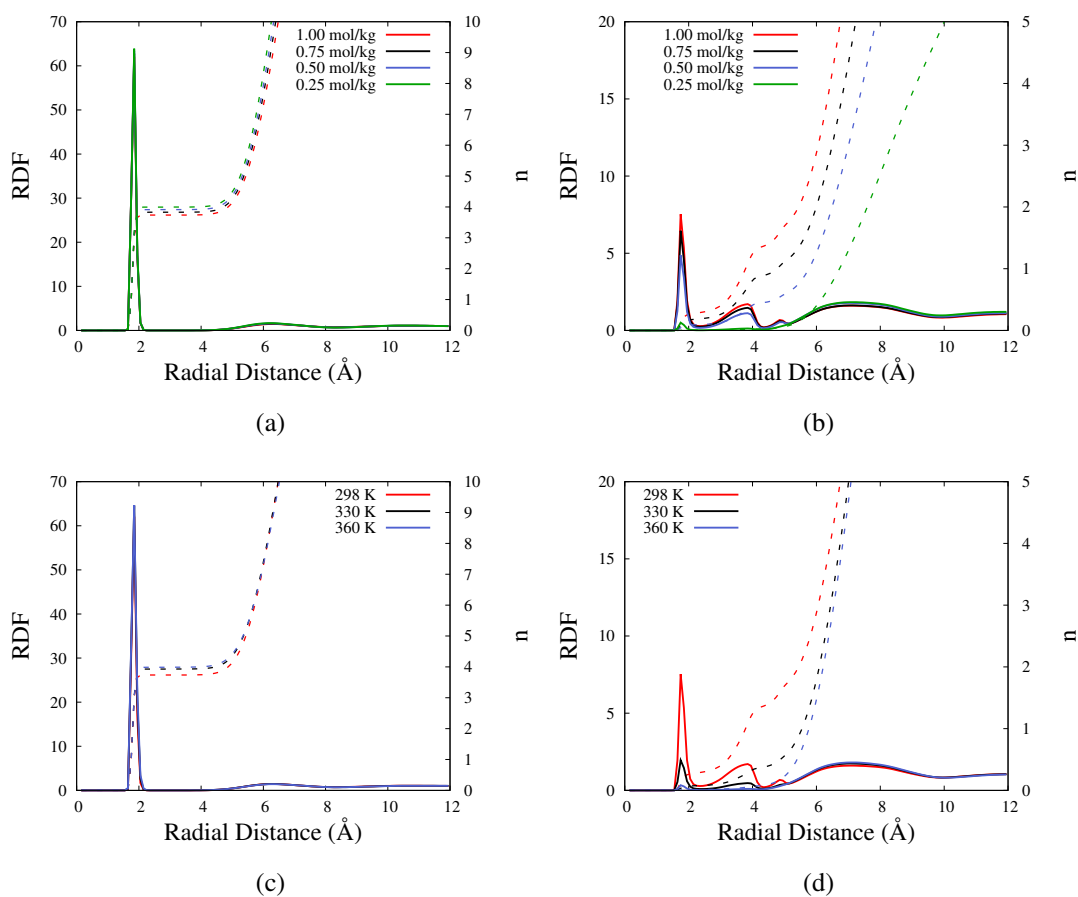


Figure A.5: Radial distribution functions (RDF) (solid lines, left y axis), and coordination numbers (dashed lines, right y axis) for LiPF_6 in solution with DMSO as function of: (a) concentration at 298 K for Li-O (DMSO), (b) concentration at 298 K for Li-F (PF_6), (c) temperature at $1.0 \text{ mol}\cdot\text{kg}^{-1}$ for Li-O (DMSO), and (d) temperature at $1.0 \text{ mol}\cdot\text{kg}^{-1}$ for Li-F (PF_6).

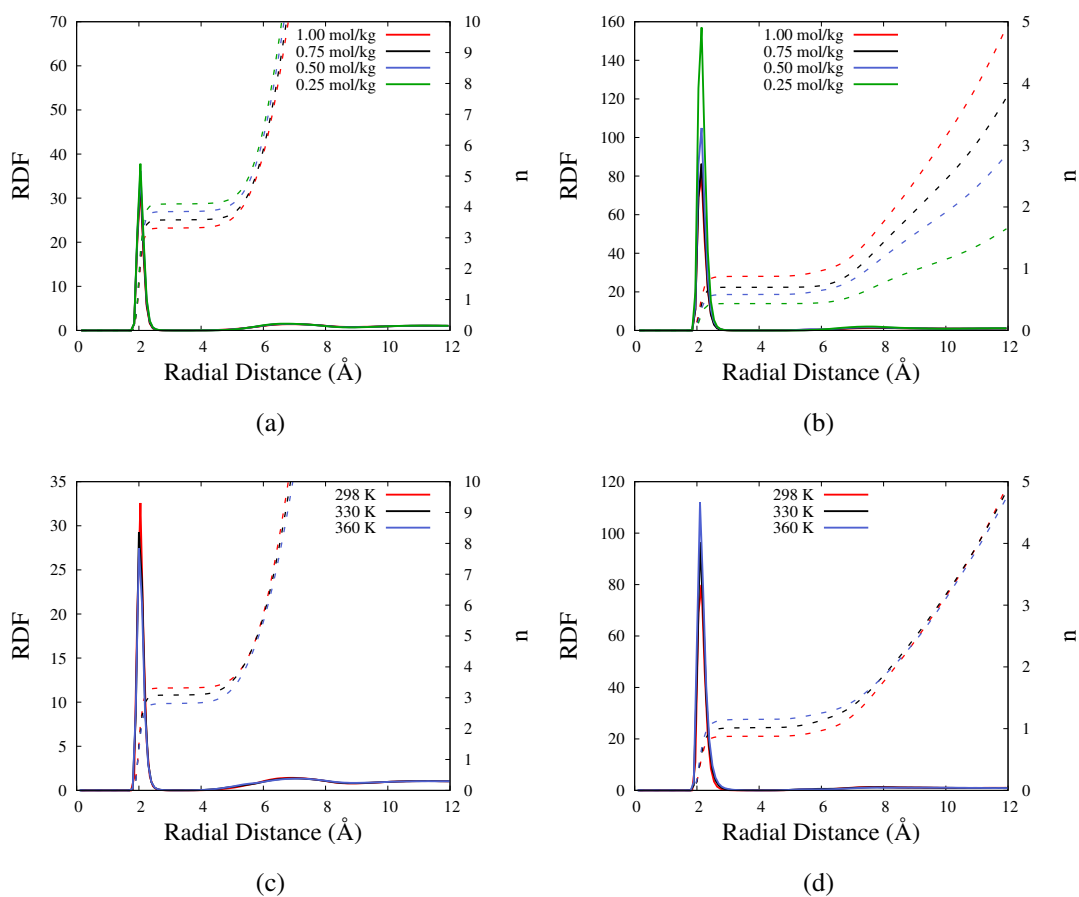


Figure A.6: Radial distribution functions (RDF) (solid lines, left y axis), and coordination numbers (dashed lines, right y axis) for LiPyr in solution with DMSO as function of: (a) concentration at 298 K for Li-O (DMSO), (b) concentration at 298 K for Li-N (Pyr), (c) temperature at 1.0 mol·kg⁻¹ for Li-O (DMSO), and (d) temperature at 1.0 mol·kg⁻¹ for Li-N (Pyr).

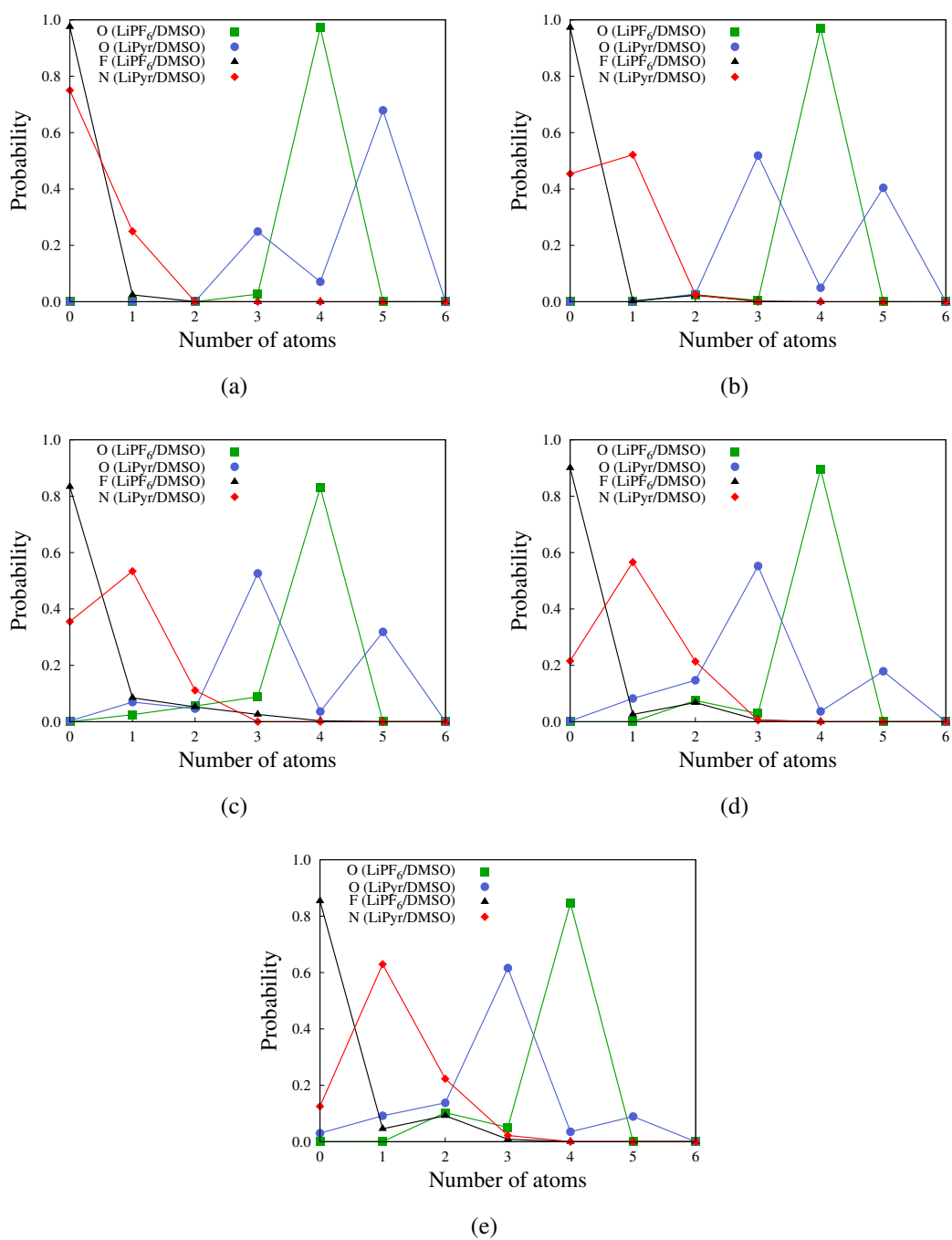


Figure A.7: Solvation probability distribution of the first shell layer at: (a) 0.25 mol·kg⁻¹ and 298 K, (b) 0.50 mol·kg⁻¹ and 298 K, (c) 0.75 mol·kg⁻¹ and 298 K, (d) 1.00 mol·kg⁻¹ and 330 K, (e) 1.00 mol·kg⁻¹ and 360 K,

A.4 Simulation details

A.4.1 Molecular sketches

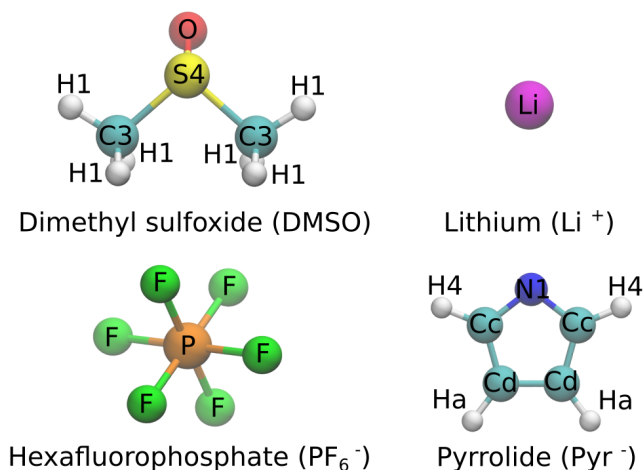


Figure A.8: Schematic illustrations of molecular structures for DMSO, PF₆⁻, Li⁺, and Pyr⁻ with assignment of atom types.

A.4.2 Dimethyl sulfoxide molecule

```

! ATOM:
!! index (int): atom index
!! name (str): atom name (required)
!! type (str): atomtype name
!! charge (float, e): partial atomic charge
!! x (float, angstrom): atom coordinate
!! y (float, angstrom): atom coordinate
!! z (float, angstrom): atom coordinate
ATOM name type charge x y z ! 10
S1 s4 0.359151 0.03900 0.26600 0.62000 ! 1
O1 o -0.485225 0.55900 1.49000 -0.10400 ! 2
C1 c3 -0.498374 -1.71300 0.05400 0.11500 ! 3
H1 h1 0.187137 -1.77400 0.06600 -0.97400 ! 4
H2 h1 0.187137 -2.10400 -0.87800 0.52700 ! 5
H3 h1 0.187137 -2.26000 0.90200 0.52700 ! 6
C2 c3 -0.498374 0.69300 -1.19800 -0.27200 ! 7
H4 h1 0.187137 0.25900 -2.10800 0.14700 ! 8
H5 h1 0.187137 0.46500 -1.09900 -1.33400 ! 9
H6 h1 0.187137 1.77200 -1.19600 -0.12100 ! 10

! BOND:
BOND ! 9
O1 S1 ! 1 1.514
  
```

```

C1  S1  ! 2   1.836
C2  S1  ! 3   1.835
C1  H1  ! 4   1.091
C1  H2  ! 5   1.091
C1  H3  ! 6   1.090
C2  H4  ! 7   1.092
C2  H5  ! 8   1.091
C2  H6  ! 9   1.090

```

! ANGLE:

```

ANGLE  ! 15
H1  C1  S1  ! 1  109.073
H2  C1  S1  ! 2  109.676
H3  C1  S1  ! 3  106.567
H4  C2  S1  ! 4  109.681
H5  C2  S1  ! 5  109.052
H6  C2  S1  ! 6  106.508
C1  S1  O1  ! 7  106.834
C2  S1  O1  ! 8  106.865
C1  S1  C2  ! 9   96.563
H1  C1  H2  ! 10 111.483
H1  C1  H3  ! 11 109.923
H2  C1  H3  ! 12 109.991
H4  C2  H5  ! 13 111.483
H4  C2  H6  ! 14 110.000
H5  C2  H6  ! 15 109.987

```

! DIHEDRAL:

```

DIHEDRAL  ! 12
H1  C1  S1  O1  ! 1   51.617
H1  C1  S1  C2  ! 2  -58.255
H2  C1  S1  O1  ! 3  173.971
H2  C1  S1  C2  ! 4   64.099
H3  C1  S1  O1  ! 5  -67.004
H3  C1  S1  C2  ! 6 -176.877
H4  C2  S1  O1  ! 7 -173.946
H4  C2  S1  C1  ! 8  -64.101
H5  C2  S1  O1  ! 9  -51.602
H5  C2  S1  C1  ! 10  58.244
H6  C2  S1  O1  ! 11  67.051
H6  C2  S1  C1  ! 12 176.897

```

A.4.3 Hexafluorophosphate molecule

! ATOM:

!! index (int): atom index

!! name (str): atom name (required)

```

!! type (str): atomtype name
!! charge (float, e): partial atomic charge
!! x (float, angstrom): atom coordinate
!! y (float, angstrom): atom coordinate
!! z (float, angstrom): atom coordinate
ATOM name type charge x y z ! 7
P1    p  1.07    0.18051    0.87394    0.02384    ! 1
F1    f -0.345    0.16559    0.88898    1.66961    ! 2
F2    f -0.345    0.19542    0.85891   -1.62194    ! 3
F3    f -0.345    1.35402    2.02802    0.02393    ! 4
F4    f -0.345   -0.99301   -0.28013    0.02374    ! 5
F5    f -0.345   -0.97348    2.04736    0.00265    ! 6
F6    f -0.345    1.33449   -0.29947    0.04502    ! 7

! BOND:
BOND ! 6
P1   F1   ! 1
P1   F2   ! 2
P1   F3   ! 3
P1   F4   ! 4
P1   F5   ! 5
P1   F6   ! 6

! ANGLE:
ANGLE ! 12
F1   P1   F3   ! 1
F1   P1   F4   ! 1
F1   P1   F5   ! 1
F1   P1   F6   ! 1
F2   P1   F3   ! 1
F2   P1   F4   ! 1
F2   P1   F5   ! 1
F2   P1   F6   ! 1
F3   P1   F5   ! 1
F3   P1   F6   ! 1
F4   P1   F5   ! 1

```

A.4.4 Lithium molecule

```

! ATOM:
!! index (int): atom index
!! name (str): atom name (required)
!! type (str): atomtype name
!! charge (float, e): partial atomic charge
!! x (float, angstrom): atom coordinate
!! y (float, angstrom): atom coordinate
!! z (float, angstrom): atom coordinate

```

```

ATOM name type charge x y z ! 1
Li1 li 1.000000 0.00000 0.00000 0.00000 ! 1

```

A.4.5 Pyrrolide molecule

```

! ATOM:
!! index (int): atom index
!! name (str): atom name (required)
!! type (str): atomtype name
!! charge (float, e): partial atomic charge
!! x (float, angstrom): atom coordinate
!! y (float, angstrom): atom coordinate
!! z (float, angstrom): atom coordinate
ATOM name type charge x y z ! 9
C1 cc 0.102030 -14.18600 7.64900 -0.31800 ! 1
C2 cc -0.328829 -12.77900 7.60400 -0.31800 ! 2
C3 cd -0.328829 -12.35800 8.96400 -0.31800 ! 3
C4 cd 0.102030 -13.54500 9.72200 -0.31800 ! 4
N1 n1 -0.672421 -14.65900 8.93000 -0.31800 ! 5
H1 h4 -0.004135 -14.87600 6.80100 -0.31800 ! 6
H2 ha 0.067145 -12.14700 6.71400 -0.31800 ! 7
H3 ha 0.067145 -11.33400 9.34200 -0.31800 ! 8
H4 h4 -0.004135 -13.63600 10.81100 -0.31800 ! 9

```

```

! BOND:
BOND ! 9
C1 C2 ! 1 1.408
C1 N1 ! 2 1.366
C1 H1 ! 3 1.093
C2 C3 ! 4 1.424
C2 H2 ! 5 1.092
C3 C4 ! 6 1.408
C3 H3 ! 7 1.092
C4 N1 ! 8 1.367
C4 H4 ! 9 1.093

```

```

! ANGLE:
ANGLE ! 13
C1 C2 C3 ! 1 105.369
C1 C2 H2 ! 2 127.211
C1 N1 C4 ! 3 105.145
C2 C1 N1 ! 4 112.098
C2 C1 H1 ! 5 127.303
C2 C3 C4 ! 6 105.361
C2 C3 H3 ! 7 127.462
C3 C2 H2 ! 8 127.421
C3 C4 N1 ! 9 112.027

```

```

C3  C4  H4  ! 10  127.338
C4  C3  H3  ! 11  127.177
H1  C1  N1  ! 12  120.599
H4  C4  N1  ! 13  120.634

```

! DIHEDRAL:

```

DIHEDRAL  ! 16
N1  C1  C2  C3  ! 1
H1  C1  C2  C3  ! 2  180.000
N1  C1  C2  H2  ! 3  180.000
H1  C1  C2  H2  ! 4
C2  C1  N1  C4  ! 5
H1  C1  N1  C4  ! 6  180.000
C1  C2  C3  C4  ! 7
H2  C2  C3  C4  ! 8 -180.000
C1  C2  C3  H3  ! 9  180.000
H2  C2  C3  H3  ! 10
C2  C3  C4  N1  ! 11
H3  C3  C4  N1  ! 12  180.000
C2  C3  C4  H4  ! 13  180.000
H3  C3  C4  H4  ! 14
C3  C4  N1  C1  ! 15
H4  C4  N1  C1  ! 16  180.000

```

! IMPROPER:

```

IMPROPER  ! 4
C2  H1  C1  N1  ! 1 -180.000
C1  C3  C2  H2  ! 2  180.000
C2  C4  C3  H3  ! 3  180.000
C3  H4  C4  N1  ! 4  180.000

```

A.4.6 Force field for DMSO/LiPF₆

Masses

```

1  32.060 # s4 DMS
2  16.000 # o DMS
3  12.010 # c3 DMS
4   1.008 # h1 DMS
5   6.941 # li LI
6  31.000 # p PF6
7  19.000 # f PF6

```

Pair Coeffs # lj/charmm/coul/long

```

1  0.35  3.564  0.35  3.564
2  0.12  3.029  0.12  3.029

```

3 0.078 3.635 0.078 3.635
 4 0.024 2.388 0.024 2.388
 5 0.10314 1.4424 0.10314 1.4424
 6 0.13169 3.695 0.13169 3.695
 7 0.028716 2.9347 0.028716 2.9347

Bond Coeffs # harmonic

1 540 1.53
 2 240 1.8
 3 322 1.11
 4 370.8 1.606

Angle Coeffs # harmonic

1 46.1 111.3
 2 79 106.75
 3 34 95
 4 35.5 108.4
 5 139.4 90

Dihedral Coeffs # charmm

1 0.2 3 0 0
 2 0.2 3 0 0

A.4.7 Force field for DMSO/LiPyr

Masses

1 32.060 # s4 DMS
 2 16.000 # o DMS
 3 12.010 # c3 DMS
 4 1.008 # h1 DMS
 5 6.941 # li LI
 6 12.010 # cc PYR
 7 12.010 # cd PYR
 8 14.010 # n1 PYR
 9 1.008 # h4 PYR
 10 1.008 # ha PYR

Pair Coeffs

1 0.350 3.564 # s4 DMS
 2 0.120 3.029 # o DMS
 3 0.078 3.635 # c3 DMS
 4 0.024 2.388 # h1 DMS

5 0.0182660800896 2.126 # li LI
 6 0.0859427210304 3.400 # cc PYR
 7 0.0859427210304 3.400 # cd PYR
 8 0.169885665734 3.250 # n1 PYR
 9 0.0149893860096 2.511 # h4 PYR
 10 0.0149893860096 2.600 # ha PYR

Bond Coeffs

1 540 1.53 # harmonic DMS o s4
 2 240 1.80 # harmonic DMS c3 s4
 3 322 1.11 # harmonic DMS c3 h1
 4 418.018786099 1.429 # harmonic PYR cc cc
 5 539.937622253 1.309 # harmonic PYR cc n1
 6 349.86553511 1.083 # harmonic PYR cc h4
 7 503.661639974 1.371 # harmonic PYR cc cd
 8 346.968143194 1.085 # harmonic PYR cc ha
 9 418.018786099 1.429 # harmonic PYR cd cd
 10 346.968143194 1.085 # harmonic PYR cd ha
 11 539.937622253 1.309 # harmonic PYR cd n1
 12 349.86553511 1.083 # harmonic PYR cd h4

Angle Coeffs

1 46.1 111.3 # harmonic DMS h1 c3 s4
 2 79.0 106.75 # harmonic DMS c3 s4 o
 3 34.0 95.0 # harmonic DMS c3 s4 c3
 4 35.5 108.4 # harmonic DMS h1 c3 h1
 5 68.1135334848 114.19 # harmonic PYR cc cc cd
 6 47.4286574016 119.26 # harmonic PYR cc cc ha
 7 0.0 0.00 # harmonic PYR cc n1 cd
 8 71.6424337152 122.98 # harmonic PYR cc cc n1
 9 45.5301607104 129.47 # harmonic PYR cc cc h4
 10 68.1135334848 114.19 # harmonic PYR cc cd cd
 11 48.3183294912 122.89 # harmonic PYR cc cd ha
 12 48.3183294912 122.89 # harmonic PYR cd cc ha
 13 71.6424337152 122.98 # harmonic PYR cd cd n1
 14 45.5301607104 129.47 # harmonic PYR cd cd h4
 15 46.9877931072 121.51 # harmonic PYR cd cd ha
 16 52.6137775488 116.36 # harmonic PYR h4 cc n1
 17 52.6137775488 116.36 # harmonic PYR h4 cd n1

Dihedral Coeffs

1 0.2 3 0 0.0 # charmm DMS h1 c3 s4 o
 2 0.2 3 0 0.0 # charmm DMS h1 c3 s4 c3
 3 3.99732847258 2 180 0.0 # charmm PYR cd cc cc n1

```

4 3.99732847258 2 180 0.0 # charmm PYR cd cc cc h4
5 3.99732847258 2 180 0.0 # charmm PYR ha cc cc n1
6 3.99732847258 2 180 0.0 # charmm PYR h4 cc cc ha
7 0.0 2 180 0.0 # charmm PYR cc cc n1 cd
8 0.0 2 180 0.0 # charmm PYR h4 cc n1 cd
9 3.99732847258 2 180 0.0 # charmm PYR cc cc cd cd
10 3.99732847258 2 180 0.0 # charmm PYR ha cc cd cd
11 3.99732847258 2 180 0.0 # charmm PYR cc cc cd ha
12 3.99732847258 2 180 0.0 # charmm PYR ha cc cd ha
13 3.99732847258 2 180 0.0 # charmm PYR cc cd cd n1
14 3.99732847258 2 180 0.0 # charmm PYR ha cd cd n1
15 3.99732847258 2 180 0.0 # charmm PYR cc cd cd h4
16 3.99732847258 2 180 0.0 # charmm PYR h4 cd cd ha
17 0.0 2 180 0.0 # charmm PYR cd cd n1 cc
18 0.0 2 180 0.0 # charmm PYR h4 cd n1 cc

```

Improper Coeffs

```

1 1.09926135821 -1 2 # cvff PYR cc h4 cc n1
2 1.09926135821 -1 2 # cvff PYR cc cd cc ha
3 1.09926135821 -1 2 # cvff PYR cc cd cd ha
4 1.09926135821 -1 2 # cvff PYR cd h4 cd n1

```

A.4.8 LAMMPS initialization file for DMSO/LiPF₆

```
#OPLS DMSO/LiPF6
```

```
# Intialization
```

```

units          real
dimension      3
boundary       p p p
atom_style     full

variable       NRUNP equal 2E6
variable       NRUNE equal 1E6
variable       NRUNV equal 10E6
variable       NRUND equal 1E6
variable       VTEMP equal 298
variable       VPRES equal 1.0
pair_style     lj/charmm/coul/long 10.0 12.0
pair_modify    tail yes
pair_modify    mix arithmetic
bond_style     harmonic
angle_style    harmonic
dihedral_style charmm
kspace_style   ppm 1.0E-4

```

```

read_data      electrolyte.data

group          dmso type 1 2 3 4
group          li type 5
group          pf6 type 6 7

# Setup atoms
velocity      all create ${VTEMP} 118647 mom yes rot yes dist gaussian

# Settings
timestep      1.0
neighbor      2.0 bin
neigh_modify  delay 0 every 1 check yes

# Operations
fix           1 all npt temp ${VTEMP} ${VTEMP} 100 iso ${VPRES} ${VPRES}
             1000

# Output
thermo        5
thermo_style  custom time temp press pe ke etotal density vol
log           npt.lammps

# Actions
run           ${NRUNP}

# Operations
unfix         1
fix           2 all nvt temp ${VTEMP} ${VTEMP} 100

run           ${NRUNE}

# Output
thermo        5
thermo_style  custom time pxx pxy pxz pyy pyz pzz density vol
log           nvt.lammps

# Actions
run           ${NRUNV}

reset_timestep 0
# Output
thermo        5
thermo_style  custom time temp etotal density vol
log           nvt.lammps
dump          myDump1 li custom 5 li.data id type mass vx vy vz
dump          myDump2 pf6 custom 5 pf6.data id type mass vx vy vz

```

```

compute      myRDF all rdf 120 5 2 5 4 5 6 5 7
fix          RDF all ave/time 1 1E6 1E6 c_myRDF[*] file rdf.data mode
           vector

```

```

# Actions
run          ${NRUND}

```

A.4.9 LAMMPS initialization file for DMSO/LiPyr

```

#OPLS DMSO/LiPYR

# Intialization
units        real
dimension    3
boundary     p p p
atom_style   full

variable     NRUNP equal 2E6
variable     NRUNE equal 1E6
variable     NRUNV equal 10E6
variable     NRUND equal 1E6
variable     VTEMP equal 298
variable     VPRES equal 1.0
pair_style   lj/charmm/coul/long 10.0 12.0
pair_modify  tail yes
pair_modify  mix arithmetic
bond_style   harmonic
angle_style  harmonic
dihedral_style charmm
improper_style cvff
kpace_style  ppm 1.0E-4

read_data    electrolyte.data

group        dmso type 1 2 3 4
group        li type 5
group        pyr type 6 7 8 9 10

# Setup atoms
velocity     all create ${VTEMP} 432393 mom yes rot yes dist gaussian

# Settings
timestep     1.0
neighbor     2.0 bin
neigh_modify delay 0 every 1 check yes

# Operations

```

```

fix                1 all npt temp ${VTEMP} ${VTEMP} 100 iso ${VPRES} ${VPRES}
    1000

# Output
thermo             5
thermo_style      custom time press pe ke etotal density vol
log               npt.lammps

# Actions
run               ${NRUNP}

# Operations
unfix             1
fix              2 all nvt temp ${VTEMP} ${VTEMP} 100

run               ${NRUNE}

# Output
thermo            5
thermo_style      custom time pxx pxy pxz pyy pyz pzz density vol
log              nvt.lammps

# Actions
run               ${NRUNV}

reset_timestep    0
# Output
thermo            5
thermo_style      custom time temp etotal density vol
log              nvt.lammps
dump              myDump1 li custom 5 li.data id type mass vx vy vz
dump              myDump2 pyr custom 5 pyr.data id type mass vx vy vz
compute           myRDF all rdf 120 5 2 5 4 5 8 5 9 5 10
fix               RDF all ave/time 1 1E6 1E6 c_myRDF[*] file rdf.data mode
    vector

# Actions
run               ${NRUND}

```

Appendix B

Codes to calculate transport and structural properties

All the codes presented here were written in C language. The instructions below explain how to run the code and they can be used with any of them:

1. To compile:

```
gcc name.c -lm -o name.exe
```

2. To run:

```
echo input_file | ./name.exe
```

All codes need an input file with specific information that must be provided by the user following the description of section *Reading input file* of the code, the format is shown in the follow example:

```
name_of_information data
```

B.1 Viscosity code

```
/* ***** */
/* School of Chemical Engineering, University of Campinas, Brazil */
/* Code to calculate viscosity using Green-Kubo equation */
/* Developer: Prof. Dr. Luis Fernando Mercier Franco */
/* Adaptation for LAMMPS: Juliane Fiates */
/* ***** */
#include <stdio.h>
#include <stdlib.h>
#include <math.h>
#include <time.h>
```

```

int main(){
    /* ***** */
    /* Variables declaration */
    /* ***** */
    /* Counter */
    int k;
    /* Counter for data points */
    int step;
    /* Total number of steps */
    int n_steps;
    /* Maximum number of steps for integration */
    int n_max;
    /* Counter for pressure tensor components */
    int p;
    /* Boltzmann constant in m2.kg/(s2.K) */
    float kb;
    /* Box volume in m3 */
    float vol, volume, density;
    /* Absolute temperature in K */
    float t;
    /* CONST = V/kB/T */
    float cons;
    /* Stress correlation functions */
    float sxy, sxz, syz, sx1, sy1, sz1;
    /* Viscosity in cP = mPa.s */
    float vis;
    /* Sum of each pressure tensor component */
    float sum[6];
    /* Average of each pressure tensor component */
    float avg[6];
    /* Input file */
    char infile[400];
    /* Auxiliary string for comments in the input file */
    char com[1000];
    /* Input file with the tensor components */
    char p_file[400];
    /* Output file with the stress auto-correlation function */
    char out_sacf_file[500];
    /* Output file with the viscosity coefficients */
    char vis_file[500];

    clock_t start, end;
    double cpu_time_used;

    FILE *in, *out;

```

```

/* ***** */
/* Physical constants */
/* ***** */
kb = 1.38064852e-23;

/* ***** */
/* Reading input file */
/* ***** */
start = clock();
scanf("%s", infile);
in = fopen(infile, "r");
fscanf(in, "%s", com);
fscanf(in, "%f", &t);
fscanf(in, "%s", com);
fscanf(in, "%d", &n_steps);
fscanf(in, "%s", com);
fscanf(in, "%d", &n_max);
fscanf(in, "%s", com);
fscanf(in, "%s", p_file);
fscanf(in, "%s", com);
fscanf(in, "%s", out_sacf_file);
fscanf(in, "%s", com);
fscanf(in, "%s", vis_file);
fclose(in);
int half_n_steps = n_steps/2;

if (n_max > half_n_steps){
    printf(" Error! n_max must be lower than n_steps/2!");
}
else{

/* ***** */
/* Memory allocation */
/* ***** */
int r = n_steps;
/* Time in fs */
int *time = calloc (r, sizeof (int));
/* Pressure tensor components in atm */
float presxx, presyy, preszz;
float *presxy = calloc (r, sizeof (float));
float *presxz = calloc (r, sizeof (float));
float *presyz = calloc (r, sizeof (float));
float *presx1 = calloc (r, sizeof (float));
float *presy1 = calloc (r, sizeof (float));
float *presz1 = calloc (r, sizeof (float));
/* Normalized pressure tensor components */
float *presxy_n = calloc (r, sizeof (float));

```

```

float *presxz_n = calloc (r, sizeof (float));
float *presyz_n = calloc (r, sizeof (float));
float *presx1_n = calloc (r, sizeof (float));
float *presy1_n = calloc (r, sizeof (float));
float *presz1_n = calloc (r, sizeof (float));
/* Average of the stress correlation function */
float *savg      = calloc (half_n_steps, sizeof (float));

/* ***** */
/* Reading pressure tensor components file */
/* ***** */
in = fopen(p_file, "r");
printf("\nReading input file...\n");
for (step = 0; step < n_steps; step++){
    fscanf(in, "%d %f %f %f %f %f %f %f", &time[step],
        &presxx, &presxy[step], &presxz[step], &presyy,
        &presyz[step], &preszz, &density, &volume);
    presx1[step] = 0.5*(presxx - presyy);
    presy1[step] = 0.5*(presyy - preszz);
    presz1[step] = 0.5*(presxx - preszz);
}
fclose(in);
vol    = volume*1e-30;
cons   = 0.010266755*vol/kb/t;
/* ***** */
/* Normalization of the pressure tensor components */
/* ***** */
for (p = 0; p < 6; p++){
    sum[p] = 0.0;
    avg[p] = 0.0;
}
for (step = 0; step < n_steps; step++){
    sum[0] = sum[0]+presx1[step];
    sum[1] = sum[1]+presxy[step];
    sum[2] = sum[2]+presxz[step];
    sum[3] = sum[3]+presy1[step];
    sum[4] = sum[4]+presyz[step];
    sum[5] = sum[5]+presz1[step];
}
for (p = 0; p < 6; p++)
    avg[p] = sum[p]/(float)(n_steps);
for (k = 0; k < n_steps; k++){
    presx1_n[k] = presx1[k]-avg[0];
    presxy_n[k] = presxy[k]-avg[1];
    presxz_n[k] = presxz[k]-avg[2];
    presy1_n[k] = presy1[k]-avg[3];
    presyz_n[k] = presyz[k]-avg[4];
}

```

```

        presz1_n[k] = presz1[k]-avg[5];
    }

    /* ***** */
    /* Memory deallocation */
    /* ***** */
    free (presx1);
    free (presxy);
    free (presxz);
    free (presy1);
    free (presyz);
    free (presz1);

    /* ***** */
    /* Stress Auto-Correlation Function calculation */
    /* ***** */
    printf("Calculating Stress ACF...\n");
    out = fopen(out_sacf_file , "w");
    for (k = 0; k < half_n_steps; k++){
        sxy = 0.0;
        sxz = 0.0;
        syz = 0.0;
        sx1 = 0.0;
        sy1 = 0.0;
        sz1 = 0.0;
        for (step = 0; step < half_n_steps; step++){
            sxy = sxy+presxy_n[step]*presxy_n[step+k];
            sxz = sxz+presxz_n[step]*presxz_n[step+k];
            syz = syz+presyz_n[step]*presyz_n[step+k];
            sx1 = sx1+presx1_n[step]*presx1_n[step+k];
            sy1 = sy1+presy1_n[step]*presy1_n[step+k];
            sz1 = sz1+presz1_n[step]*presz1_n[step+k];
        }
        sxy = sxy/(float)(half_n_steps);
        sxz = sxz/(float)(half_n_steps);
        syz = syz/(float)(half_n_steps);
        sx1 = sx1/(float)(half_n_steps);
        sy1 = sy1/(float)(half_n_steps);
        sz1 = sz1/(float)(half_n_steps);
        savg[k] = (sxy+sxz+syz+sx1+sy1+sz1)/6.0;
        fprintf(out, "%d %f %f\n", time[k]-time[0], savg[k], savg[k]/
            savg[0]);
    }
    fclose(out);

    /* ***** */
    /* Integration of Stress Auto-Correlation Function */

```

```

/* Green-Kubo equation for viscosity */
/* ***** */
printf("Integrating Stress ACF to calculate viscosity...\n");
out = fopen(vis_file , "w");
for (k = 0; k < n_max; k++){
    vis = savg[0];
    for (step = 1; step < k-1; step++)
        vis = vis+2.0*savg[step];
    vis = cons*0.5*(float)(time[step]-time[0])*(vis+savg[step])/
        (float)(k-1);
    if (step > 1)
        fprintf(out, "%d %f\n", time[step]-time[0], vis);
}
fclose(out);
end = clock();
cpu_time_used = ((double) (end-start)) / CLOCKS_PER_SEC;
printf("The calculation is ended...\n\n");
printf("Elapsed time = %lf seconds...\n\n", cpu_time_used);
}

return 0;
}

```

B.2 Self-diffusion code

```

/* ***** */
/* School of Chemical Engineering, University of Campinas, Brazil */
/* Code to calculate the self-diffusion coef. using Green-Kubo equation */
/* Developer: Juliane Fiates */
/* Supervisor: Dr. Gustavo Doubek and Dr. Luis Fernando Mercier Franco */
/* ***** */
#include <stdlib.h>
#include <stdio.h>
#include <math.h>
#include <time.h>

int main(){
    /* ***** */
    /* Variables declaration */
    /* ***** */
    /* Counters */
    int i,j,k,step;
    /* Molecules per frame */
    int af,idx,type;
    /* Box size */
    float bxl,bxu;

```

```

float  byl,byu;
float  bzl,bzu;
/* Unit conversion */
double unit_conv;
/* Total number of steps */
int  n_steps;
/* ID number of the first atom in Dump file */
int  st_atom;
/* Maximum number of steps for integration */
int  n_max;
/* Total number of molecules */
int  n_mol;
/* Number of atoms per molecule */
int  n_atoms;
/* Masses */
float  mass;
/* Total mass */
float  totmass;
/* Velocity auto-correlation funcion */
double  vcfx ,vcfy ,vcfz ,vx ,vy ,vz;
/* Self-diffusion coefficient */
double  diff;
/* Input file */
char  infile[400];
/* Auxiliary string for comments in the input file */
char  com[1000];
/* Input file with velocities */
char  vel_file[400];
/* Output file with the velocity auto-correlation function */
char  out_vacf_file[500];
/* Output file with the self-diffusion coefficient */
char  diff_file[500];

clock_t  start , end;
double  cpu_time_used;

FILE  *in , *out;

/* ***** */
/* Reading input file */
/* ***** */
start = clock();
scanf("%s", infile);
in = fopen(infile , "r");
fscanf(in , "%s" , com);
fscanf(in , "%lf" , &unit_conv);
fscanf(in , "%s" , com);

```

```

fscanf(in, "%d", &st_atom);
fscanf(in, "%s", com);
fscanf(in, "%d", &n_steps);
fscanf(in, "%s", com);
fscanf(in, "%d", &n_max);
fscanf(in, "%s", com);
fscanf(in, "%d", &n_mol);
fscanf(in, "%s", com);
fscanf(in, "%d", &n_atoms);
fscanf(in, "%s", com);
fscanf(in, "%f", &totmass);
fscanf(in, "%s", com);
fscanf(in, "%s", vel_file);
fscanf(in, "%s", com);
fscanf(in, "%s", out_vacf_file);
fscanf(in, "%s", com);
fscanf(in, "%s", diff_file);
fclose(in);
int half_n_steps = n_steps/2;
/* ***** */

if (n_max > half_n_steps){
    printf(" Error! n_max must be lower than n_steps/2!");
}
else{

/* ***** */
/* Memory allocation */
/* ***** */
int r = n_steps;
int c = n_mol*n_atoms;
int x = n_mol;
double *vx_n = calloc (c, sizeof (double));
double *vy_n = calloc (c, sizeof (double));
double *vz_n = calloc (c, sizeof (double));
int *time = calloc (r, sizeof (int));
double *vacf_avg = calloc (half_n_steps, sizeof (double));
double *vcx[r], *vcy[r], *vcz[r];
for (i = 0; i < r; i++){
    vcx[i] = (double*) calloc (x, sizeof(double));
    vcy[i] = (double*) calloc (x, sizeof(double));
    vcz[i] = (double*) calloc (x, sizeof(double));
}

/* ***** */
/* Reading velocity input file */
/* ***** */

```

```

printf("Reading input file...\n");
in = fopen(vel_file , "r");
for (step = 0; step < n_steps; step++){
    fscanf(in , "%d" , &time[step]);
    fscanf(in , "%d" , &af);
    fscanf(in , "%e %e" , &bxl , &bxu);
    fscanf(in , "%e %e" , &byl , &byu);
    fscanf(in , "%e %e" , &bzl , &bzu);
    for (j = 0; j < (n_mol*n_atoms); j++){
        fscanf(in , "%d %d %f %lf %lf %lf" , &idx , &type , &mass , &
            vx , &vy , &vz);
        vx_n[idx]=(vx*mass)/totmass;
        vy_n[idx]=(vy*mass)/totmass;
        vz_n[idx]=(vz*mass)/totmass;
    }

/* ***** */
/* Calculation of velocity at center of mass of the molecule */
/* ***** */
    i=0;
    for(idx = st_atom; idx < (st_atom+(n_mol*n_atoms)); idx=idx+
        n_atoms){
        for (k = 0; k < n_atoms; k++){
            vcx[step][i] = vcx[step][i]+vx_n[idx+k];
            vcy[step][i] = vcy[step][i]+vy_n[idx+k];
            vcz[step][i] = vcz[step][i]+vz_n[idx+k];
        }
        i++;
    }
}
fclose(in);

/* ***** */
/* Velocity Auto-Correlation Function (VACF) calculation */
/* ***** */
printf("Calculating VACF...\n");
out = fopen(out_vacf_file , "w");
for (k = 0; k < half_n_steps; k++){
    vcfx = 0.0;
    vcfy = 0.0;
    vcfz = 0.0;
    for (step = 0; step < half_n_steps; step++){
        for (i = 0; i < n_mol; i++){
            vcfx = vcfx+vcx[step][i]*vcx[step+k][i];
            vcfy = vcfy+vcy[step][i]*vcy[step+k][i];
            vcfz = vcfz+vcz[step][i]*vcz[step+k][i];
        }
    }
}

```

```

    }
}
vacf_avg[k] = (vcfx+vcfy+vcfz)/(double)(n_mol)/(double)(
    half_n_steps)/3.0;
fprintf(out, "%d %e %e\n", time[k]-time[0], vacf_avg[k],
    vacf_avg[k]/vacf_avg[0]);
}
fclose(out);

/* ***** */
/* Numerical Integration of Velocity Auto-Correlation Function */
/* Green-Kubo equation for self-diffusion coefficient */
/* ***** */
printf("Integrating VACF...\n");
out = fopen(diff_file, "w");
for (k = 0; k < n_max; k++){
    diff = vacf_avg[0];
    for (step = 1; step < k-1; step++)
        diff = diff+2.0*vacf_avg[step];
    diff = unit_conv*0.5*(double)(time[step]-time[0])*(diff+
        vacf_avg[step])/(double)(k-1);
    if (step > 1)
        fprintf(out, "%d %e \n", time[step]-time[0], diff);
}
fclose(out);
end = clock();
cpu_time_used = ((double) (end-start)) / CLOCKS_PER_SEC;
printf("The calculation is ended...\n\n");
printf("Elapsed time = %lf seconds...\n\n", cpu_time_used);
}

return 0;
}

```

B.3 Ionic conductivity code

```

/* ***** */
/* School of Chemical Engineering, University of Campinas, Brazil */
/* Code to calculate the ionic conductivity using Green-Kubo equation */
/* Developer: Juliane Fiates */
/* Supervisor: Dr. Gustavo Doubek and Dr. Luis Fernando Mercier Franco */
/* ***** */
#include <stdlib.h>
#include <stdio.h>
#include <math.h>

```

```

#include <time.h>

int main() {
    /* ***** */
    /* Variables declaration */
    /* ***** */
    /* Counters */
    int i,j,k,l,step;
    /* Boltzmann constant in m2.kg/(s2.K) */
    double kb;
    /* Elemental electric charge in Coulomb */
    double ee;
    /* Temperature in K */
    float t;
    /* Box volume in m3 */
    float vol;
    /* Constant */
    double cons;
    /* Molecules per frame */
    int af,idx,type;
    /* Box size */
    float bxl, bxu;
    float byl, byu;
    float bzl, bzu;
    /* Unit conversion */
    double unit_conv;
    /* Anion electrical charge */
    float qa;
    /* Cation electrical charge */
    float qc;
    /* Total number of steps */
    int n_steps;
    /* Maximum number of steps for integration */
    int n_max;
    /* Total number of molecules */
    int n_mol;
    /* Masses */
    float mass;
    /* Total mass */
    float totmass;
    /* Number of atoms per molecule of anion */
    int n_anion;
    /* ID number of the first anion atom in Dump file */
    int st_at_a;
    /* Number of atoms per molecule of cation */
    int n_cation;
    /* ID number of the first cation atom in Dump file */

```

```

int st_at_c;
/* Velocities */
double vx,vy,vz;
/* Electrical current auto-correlation funcion */
double jcfx ,jcfy ,jcfz;
/* Electrical conductivity coefficient in Si/m */
double cond;
/* Input file */
char inpfile[400];
/* Auxiliary string for comments in the input file */
char com[1000];
/* Input anion file with velocities */
char anion_vel_file[400];
/* Input cation file with velocities */
char cation_vel_file[400];
/* Output file with the electrical auto-correlation function */
char out_jacf_file[500];
/* Output file with the electrical conductivity coefficient */
char cond_file[500];

clock_t start , end;
double cpu_time_used;

FILE *in , *out;

/* ***** */
/* Reading input file */
/* ***** */
scanf("%s", inpfile);
in = fopen(inpfile , "r");
fscanf(in , "%s", com);
fscanf(in , "%lf", &unit_conv);
fscanf(in , "%s", com);
fscanf(in , "%f", &t);
fscanf(in , "%s", com);
fscanf(in , "%f", &vol);
fscanf(in , "%s", com);
fscanf(in , "%f", &qa);
fscanf(in , "%s", com);
fscanf(in , "%f", &qc);
fscanf(in , "%s", com);
fscanf(in , "%d", &n_steps);
fscanf(in , "%s", com);
fscanf(in , "%d", &n_max);
fscanf(in , "%s", com);
fscanf(in , "%d", &n_mol);
fscanf(in , "%s", com);

```

```

fscanf(in, "%f", &totmass);
fscanf(in, "%s", com);
fscanf(in, "%d", &n_anion);
fscanf(in, "%s", com);
fscanf(in, "%d", &st_at_a);
fscanf(in, "%s", com);
fscanf(in, "%d", &n_cation);
fscanf(in, "%s", com);
fscanf(in, "%d", &st_at_c);
fscanf(in, "%s", com);
fscanf(in, "%s", anion_vel_file);
fscanf(in, "%s", com);
fscanf(in, "%s", cation_vel_file);
fscanf(in, "%s", com);
fscanf(in, "%s", out_jacf_file);
fscanf(in, "%s", com);
fscanf(in, "%s", cond_file);
fclose(in);
int half_n_steps = n_steps/2;

/* ***** */
/* Physical constants */
/* ***** */
kb = 1.38064852e-23;
ee = 1.60217657e-19;
vol = vol * 1e-30;
cons = unit_conv*ee*ee/kb/t/vol;

if (n_max > half_n_steps){
    printf(" Error! n_max must be lower than n_steps/2!");
}
else{

/* ***** */
/* General memory allocation */
/* ***** */
int r = n_steps;
int x = n_mol;

int *time = calloc (r, sizeof (int));
double *j_avg = calloc (half_n_steps, sizeof (double));
double *jx[r], *jy[r], *jz[r];
    for (i = 0; i < r; i++){
        jx[i] = (double*) calloc (x, sizeof(double));
        jy[i] = (double*) calloc (x, sizeof(double));
        jz[i] = (double*) calloc (x, sizeof(double));
    }
}

```

```

/* **** */
/* Memory allocation to anion */
/* **** */
int a = n_mol*n_anion;

double *vx_na = calloc (a, sizeof (double));
double *vy_na = calloc (a, sizeof (double));
double *vz_na = calloc (a, sizeof (double));
double *vcxa = calloc (a, sizeof (double));
double *vcya = calloc (a, sizeof (double));
double *vcza = calloc (a, sizeof (double));
double *jxa[r], *jya[r], *jza[r];
    for (i = 0; i < r; i++){
        jxa[i] = (double*) calloc (x, sizeof(double));
        jya[i] = (double*) calloc (x, sizeof(double));
        jza[i] = (double*) calloc (x, sizeof(double));
    }

/* **** */
/* Reading velocity input file of the anion */
/* **** */
printf("Reading anion input file...\n");
in = fopen(anion_vel_file, "r");
for (step = 0; step < n_steps; step++){
    fscanf(in, "%d", &time[step]);
    fscanf(in, "%d", &af);
    fscanf(in, "%e %e", &bxl, &bxu);
    fscanf(in, "%e %e", &byl, &byu);
    fscanf(in, "%e %e", &bzl, &bzu);
    for (j = 0; j < (n_mol*n_anion); j++){
        fscanf(in, "%d %d %f %lf %lf %lf", &idx, &type,
            &mass, &vx, &vy, &vz);
        vx_na[idx]=(vx*mass)/totmass;
        vy_na[idx]=(vy*mass)/totmass;
        vz_na[idx]=(vz*mass)/totmass;
    }

/* **** */
/* Calculation of velocity at center of mass of the molecule */
/* **** */
i=0;
for (idx=st_at_a; idx<(st_at_a+(n_mol*n_anion)); idx=idx+n_anion)
{
    for (k = 0; k < n_anion; k++){
        vcxa[i] = vcxa[i]+vx_na[idx+k];
        vcya[i] = vcya[i]+vy_na[idx+k];
    }
}

```

```

        vcza[i] = vcza[i]+vz_na[idx+k];
/* ***** */
/* Calculation of the electrical current of the anion */
/* ***** */
        jxa[step][i] = qa * vcxa[i];
        jya[step][i] = qa * vcya[i];
        jza[step][i] = qa * vcza[i];
    }
    i++;
}
fclose(in);

/* ***** */
/* Memory deallocation to anion */
/* ***** */
free (vx_na);
free (vy_na);
free (vz_na);
free (vcxa);
free (vcya);
free (vcza);

/* ***** */
/* Memory allocation to cation */
/* ***** */
int c = n_mol*n_cation;

double *vx_nc = calloc (c, sizeof (double));
double *vy_nc = calloc (c, sizeof (double));
double *vz_nc = calloc (c, sizeof (double));
double *vcxc = calloc (c, sizeof (double));
double *vcyc = calloc (c, sizeof (double));
double *vczc = calloc (c, sizeof (double));
double *jxc[r], *jyc[r], *jzc[r];
    for (i = 0; i < r; i++){
        jxc[i] = (double*) calloc (x, sizeof(double));
        jyc[i] = (double*) calloc (x, sizeof(double));
        jzc[i] = (double*) calloc (x, sizeof(double));
    }

/* ***** */
/* Reading velocity input file of the cation */
/* ***** */
printf("Reading cation input file...\n");
in = fopen(cation_vel_file , "r");
for (step = 0; step < n_steps; step++){

```

```

fscanf(in, "%d", &time[step]);
fscanf(in, "%d", &af);
fscanf(in, "%e %e", &bxl, &bxu);
fscanf(in, "%e %e", &byl, &byu);
fscanf(in, "%e %e", &bzl, &bzu);
for (j = 0; j < (n_mol*n_cation); j++){
    fscanf(in, "%d %d %f %lf %lf %lf", &idx, &type,
    &mass, &vx, &vy, &vz);
    vx_nc[idx]=(vx*mass)/totmass;
    vy_nc[idx]=(vy*mass)/totmass;
    vz_nc[idx]=(vz*mass)/totmass;
}

/* ***** */
/* Calculation of velocity at center of mass of the molecule */
/* ***** */
i=0;
for(idx=st_at_c;idx <(st_at_c+(n_mol*n_cation));idx=idx+
n_cation){
    for (k = 0; k < n_cation; k++){
        vcxc[i] = vcxc[i]+vx_nc[idx+k];
        vcyc[i] = vcyc[i]+vy_nc[idx+k];
        vczc[i] = vczc[i]+vz_nc[idx+k];
/* ***** */
/* Calculation of the electrical current of the cation */
/* ***** */
        jxc[step][i] = qc * vcxc[i];
        jyc[step][i] = qc * vcyc[i];
        jzc[step][i] = qc * vczc[i];
    }
    i++;
}
fclose(in);

/* ***** */
/* Memory deallocation to cation */
/* ***** */
free (vx_nc);
free (vy_nc);
free (vz_nc);
free (vcxc);
free (vcyc);
free (vczc);

/* ***** */
/* Calculation of the electrical current */
/* ***** */

```

```

/*****
for (step = 0; step < n_steps; step++){
    for (i = 0; i < n_mol; i++){
        jx[step][i] = jxa[step][i]+jxc[step][i];
        jy[step][i] = jya[step][i]+jyc[step][i];
        jz[step][i] = jza[step][i]+jzc[step][i];
    }
}

/*****
/* Electrical Current Auto-Correlation Function calculation */
/* JACF */
/*****
printf("Calculating JACF...\n");
out = fopen(out_jacf_file , "w");
for (k = 0; k < half_n_steps; k++){
    jcfx = 0.0;
    jcfy = 0.0;
    jcfz = 0.0;
    for (step = 0; step < half_n_steps; step++){
        for (i = 0; i < n_mol; i++){
            jcfx = jcfx+jx[step][i]*jx[step+k][i];
            jcfy = jcfy+jy[step][i]*jy[step+k][i];
            jcfz = jcfz+jz[step][i]*jz[step+k][i];
        }
    }
    j_avg[k] = (jcfx+jcfy+jcfz)/(double)(half_n_steps)/3.0;
    fprintf(out, "%d %e %e\n", time[k]-time[0], j_avg[k], j_avg[k]/
        j_avg[0]);
}
fclose(out);

/*****
/* Numerical Integration of JACF */
/* Green-Kubo equation for electrical conductivity coeff. */
/*****
printf("Integrating JACF...\n");
out = fopen(cond_file , "w");
for (k = 0; k < n_max; k++){
    cond = j_avg[0];
    for (step = 1; step < k-1; step++)
        cond = cond+2.0*j_avg[step];
    cond = cons*0.5*(double)(time[step]-time[0])*(cond+j_avg[step
    ])/(double)(k-1);
    if (step > 1)
        fprintf(out, "%d %e \n", time[step]-time[0], cond);
}

```

```

fclose(out);
end
    = clock();
cpu_time_used = ((double) (end-start)) / CLOCKS_PER_SEC;
printf(" The calculation is ended...\n\n");
printf(" Elapsed time = %lf seconds...\n\n", cpu_time_used);
}

return 0;
}

```

B.4 Radial distribution function and coordination number code

```

/* ***** */
/* School of Chemical Engineering, University of Campinas, Brazil */
/* Code to calculate the radial distribution function and */
/* the coordinate number at the bulk system based on atoms type */
/* Code to unwrapped coordinates */
/* Developer: Juliane Fiates */
/* Supervisor: Dr. Gustavo Doubek and Dr. Luis Fernando Mercier Franco */
/* ***** */
#include <stdlib.h>
#include <stdio.h>
#include <math.h>
#include <time.h>
#include <string.h>

int main(){
    /* ***** */
    /* Variables declaration */
    /* ***** */
    /* Counters */
    int i,j,k,bin,step,idx;
    /* Molecules per frame */
    int af,type;
    /* Box size fom dump file */
    float bxl,bxu;
    float byl,byu;
    float bzl,bzu;
    /* Time */
    int time;
    /* Total number of steps */
    int n_steps;
    /* Total number of molecules */
    int n_molt;

```

```

/* Atom types used to compute the distribution function */
int tp_1 ,tp_2;
/* Number of atoms of each type */
int cont1 ,cont2;
/* Coordinates */
float x,y,z;
/* Width of the bin */
float delr;
/* The lower value of radius */
float rlower;
/* The upper value of radius */
float rupper;
/* Number of ideal gas particles at same density */
float nideal;
/* Number of bins */
int maxbin;
/* Box size */
float boxl;
/* Volume */
float vol;
/* Distance between the atoms */
float rxij ,ryij ,rzij ,rijsq ,rij;
/* Coordination number */
float n;
/* Input file */
char inpfile[50];
/* Auxiliary string for comments in the input file */
char com[500];
/* Input file with the coordinates */
char cor_file[50];
/* Output file with the RDF */
char g_file[50];
/* Output file with the coordination number */
char n_file[50];

FILE *in , *out;

/* ***** */
/* Reading input file */
/* ***** */
scanf("%s", inpfile);
in = fopen(inpfile , "r");
fscanf(in , "%s", com);
fscanf(in , "%d", &n_steps);
fscanf(in , "%s", com);
fscanf(in , "%d", &n_molt);
fscanf(in , "%s", com);

```

```

fscanf(in, "%d", &tp_1);
fscanf(in, "%s", com);
fscanf(in, "%d", &tp_2);
fscanf(in, "%s", com);
fscanf(in, "%d", &maxbin);
fscanf(in, "%s", com);
fscanf(in, "%f", &vol);
fscanf(in, "%s", com);
fscanf(in, "%s", cor_file);
fscanf(in, "%s", com);
fscanf(in, "%s", g_file);
fscanf(in, "%s", com);
fscanf(in, "%s", n_file);
fclose(in);

/* ***** */
/* Memory allocation */
/* ***** */
int c = n_molt;
int a = maxbin;
/* Coordinates of atom 1 and 2 */
float *rx_i = calloc (c, sizeof (float));
float *ry_i = calloc (c, sizeof (float));
float *rz_i = calloc (c, sizeof (float));
float *rx_j = calloc (c, sizeof (float));
float *ry_j = calloc (c, sizeof (float));
float *rz_j = calloc (c, sizeof (float));
/* Histogram and RDF */
int *hist = calloc (r, sizeof (int));
float *gr = calloc (r, sizeof (float));
float *gr_n = calloc (a, sizeof (float));
float *r = calloc (a, sizeof (float));

/* ***** */
/* Reading the coordinates input file */
/* ***** */
printf("Reading input file...\n");
in = fopen(cor_file, "r");
for (step = 0; step < n_steps; step++){
    fscanf(in, "%d", &time);
    fscanf(in, "%d", &af);
    fscanf(in, "%e %e", &bxl, &bxu);
    fscanf(in, "%e %e", &byl, &byu);
    fscanf(in, "%e %e", &bzl, &bzu);
    cont1 = 0;
    cont2 = 0;
    for (i = 0; i < n_molt; i++){

```

```

fscanf(in, "%d %d %f %f %f", &idx, &type, &x, &y, &z);
    if(type == tp_1){
        rx_i[cont1] = x;
        ry_i[cont1] = y;
        rz_i[cont1] = z;
        cont1++;
    }
    if(type == tp_2){
        rx_j[cont2] = x;
        ry_j[cont2] = y;
        rz_j[cont2] = z;
        cont2++;
    }
}

/* ***** */
/* Calculation of the histogram */
/* ***** */
boxl = pow(vol,(1.0/3.0));
delr = (0.5*boxl)/(float)(maxbin);
    for (i = 0; i < cont1-1; i++){
        for (j = i+1; j < cont2; j++){
            rxij = rx_i[i]-rx_j[j];
            ryij = ry_i[i]-ry_j[j];
            rzij = rz_i[i]-rz_j[j];
            rxij = rxij-boxl*round(rxij/boxl);
            ryij = ryij-boxl*round(ryij/boxl);
            rzij = rzij-boxl*round(rzij/boxl);
            rijsq = rxij*rxij+ryij*ryij+rzij*rzij;
            rij = pow(rijsq,(1.0/2.0));
            bin = (int)(rij/delr)+1;
            if (bin <= maxbin)
                hist[bin]=hist[bin]+2;
        }
    }
}
fclose (in);

/* ***** */
/* Calculation of the Radial Distribution Function (RDF) */
/* ***** */
printf("Calculating the RDF...\n");
out = fopen(g_file, "w");
float cons_g = (4.0*M_PI*((cont1*cont2)/vol))/3.0;
float cons_n = cont2/vol;
for(bin = 0; bin < maxbin; bin++){
    rlower = (float)(bin)*delr;

```

```

    rupper = rlower + delr;
    nideal = cons_g * ((rupper*rupper*rupper)-(rlower*rlower*rlower
    ));
    gr[bin]= (float)(hist[bin])/(float)(n_steps)/nideal;
    gr_n[bin] = gr[bin]*(rlower*rlower);
    fprintf(out, "%e %e \n", rlower, gr[bin]);
}
fclose (out);

/* ***** */
/* Calculation of the coordination number (n) */
/* ***** */
printf("Integration of the RDF...\n");
out = fopen(n_file, "w");
for (bin = 0; bin < maxbin; bin++){
    r[bin] = (float)(bin)*delr;
    n      = gr_n[0];
    for (k = 1; k < bin-1; k++){
        n = n+2.0*gr_n[k];
    }
    n = cons_n*0.5*(r[k]-r[0])*(n+gr_n[k])/(float)(bin-1);
    if (k > 1)
        fprintf(out, "%e %e \n", r[k]-r[0], n);
}
fclose (out);

return 0;
}

```

B.5 Average and standard deviation code

```

/* ***** */
/* School of Chemical Engineering, University of Campinas, Brazil */
/* Code to calculate the average and standard deviation of properties */
/* Developer: Juliane Fiates */
/* Supervisor: Dr. Gustavo Doubek and Dr. Luis Fernando Mercier Franco */
/* ***** */
#include <stdlib.h>
#include <stdio.h>
#include <math.h>

int main(){
    /* ***** */
    /* Variables declaration */
    /* ***** */
    /* Counters */
    int i,k,step;

```

```

/* Property values */
double ppt;
/* Number of trajectories */
int n;
/* Total number of steps */
int n_steps;
/* Input file */
char infile[100];
/* Auxiliary string for comments in the input file */
char com[100];
/* Input files with the properties */
char filename[100];
/* Output file with the average and standard deviation */
char out_file[100];

FILE *in, *out;

/* ***** */
/* Reading input file */
/* ***** */
scanf("%s", infile);
in = fopen(infile, "r");
fscanf(in, "%s", com);
fscanf(in, "%d", &n);
fscanf(in, "%s", com);
fscanf(in, "%d", &n_steps);
fscanf(in, "%s", com);
fscanf(in, "%s", out_file);
fclose(in);

/* ***** */
/* Memory allocation */
/* ***** */
int r = n;
int x = n_steps;
double *sum1 = calloc (x, sizeof(double));
double *sum2 = calloc (x, sizeof(double));
double *avg = calloc (x, sizeof(double));
double *var = calloc (x, sizeof(double));
double *std = calloc (x, sizeof(double));
int *idx = calloc (x, sizeof(int));
double *ppt_n[r];
for (i = 1; i <= r; i++)
    ppt_n[i] = (double*) calloc (x, sizeof(double));

/* ***** */
/* Reading property input file */
/* ***** */

```

```

/*****
printf("Reading input file...\n");
for (i = 1; i <= n; i++){
    sprintf(filename , "name%d.data", i);
    in = fopen(filename , "r");
    if (in == NULL){
        printf("Change the information of the input file in line
            69! \n");
        exit(1);
    }
    for (step = 2; step < n_steps -1; step++){
        fscanf(in , "%d %lf", &idx[step], &ppt);
        ppt_n[i][step] = ppt;
    }
}
fclose(in);

/*****
/* Calculation of the average, variance and standard deviation */
/*****
printf("Calculating average...\n");
out = fopen(out_file , "w");
for (step = 2; step < n_steps -1; step++){
    for (i = 1; i <= n; i++){
        sum1[step] = sum1[step] + ppt_n[i][step];
    }
    avg[step] = sum1[step]/(float)(n);
}
printf("Calculating variance and standard deviation...\n");
for (step = 2; step < n_steps -1; step++){
    for (i = 1; i <= n; i++){
        sum2[step] = sum2[step] + pow((ppt_n[i][step]-avg[step]),
            2);
    }
    var[step] = sum2[step]/(float)(n-1);
    std[step] = sqrt(var[step]);
    fprintf(out , "%d %e %e \n", idx[step], avg[step], std[step]);
}
fclose(out);

return 0;
}

```

Appendix C

Effect of electrode material and solvent donor number in Li-air battery: insights from Molecular Dynamics simulations[‡]

Juliane Fiates^{a,b}, Yong Zhang^b, Luís F. M. Franco^a, Edward J. Maginn^b and Gustavo Doubek^a

^a *School of Chemical Engineering,
University of Campinas,
Campinas 13083-852, Brazil.*

^b *Department of Chemical and Biomolecular Engineering,
University of Notre Dame,
Notre Dame, Indiana 46556, USA.*

Dated: June 30, 2020

[‡]It will be submitted for publication at The Journal of Physical Chemistry C.

The information contained in this material is described as:

- Tables C.1 and C.2 present the Lennard-Jones and bond parameters used on the simulations. Figure C.1 illustrates the charge assignment for TEGDME molecule.
- Figures C.2, C.3, and C.4 show the averaged local concentration and the standard deviation for gold/DMSO, graphene/DMSO, and graphene/TEGDME systems, respectively.
- Figures C.5, C.6, and C.7 show the charge distribution, and the electric field for gold/DMSO, graphene/DMSO, and graphene/TEGDME systems, respectively.

Table C.1: Force field parameters for nonbonded interactions

Nonbonded Parameters			
atom	charge	$\epsilon / \text{kcal}\cdot\text{mol}^{-1}$	$\sigma / \text{\AA}$
H (DMSO) ^a	0.090	0.024	2.388
C (DMSO) ^a	-0.148	0.078	3.635
S (DMSO) ^a	0.312	0.350	3.564
O (DMSO) ^a	-0.556	0.120	3.029
H (TEGMDE) ^b		0.0141216	2.545
C (TEGMDE) ^b		0.0983942	3.502
O (TEGMDE) ^b		0.152897	3.090
Li ^c	1.00	0.10314	1.4424
P ^c	1.07	0.13169	3.695
F ^c	-0.345	0.028716	2.9347
Au ^d		0.11472	3.80
C (graphene) ^e		0.086	3.40

^a Strader and Feller⁹²; ^b Barbosa *et al.*¹⁴; ^c Jorn *et al.*⁹³; ^d Wright *et al.*¹³⁴; ^e Lee and Carignano¹³⁵.

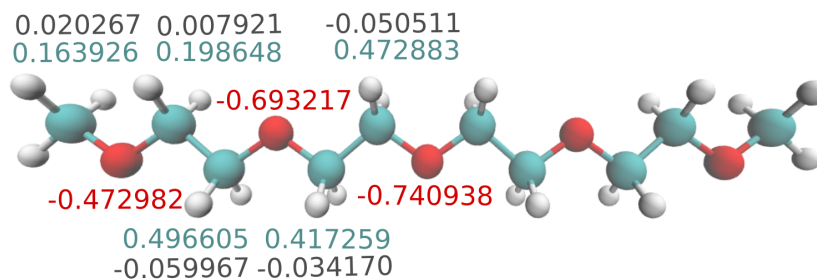


Figure C.1: TEGDME molecule charge assignment for each atom¹⁴. Color code: oxygen (red), hydrogen (white), carbon (cyan).

Table C.2: Force field parameters for bonded interactions

Bond Parameters			
bond	$k_b / \text{kcal}\cdot\text{mol}^{-1}\cdot\text{\AA}^{-2}$	$b_0 / \text{\AA}$	
H-C (DMSO) ^a	322	1.11	
C-S (DMSO) ^a	240	1.80	
S-O (DMSO) ^a	540	1.53	
C-H (TEGDME) ^b	335.674	1.093	
C-O (TEGDME) ^b	301.299	1.439	
C-C (TEGDME) ^b	302.898	1.535	
P-F ^c	370.8	1.606	
Angle Parameters			
angle	$k_\theta / \text{kcal}\cdot\text{mol}^{-1}\cdot\text{rad}^{-2}$	θ_0 / deg	
H-C-H (DMSO) ^a	35.5	108.4	
H-C-S (DMSO) ^a	46.1	111.3	
C-S-O (DMSO) ^a	79.0	106.75	
C-S-C (DMSO) ^a	34.0	95.0	
C-O-C (TEGDME) ^b	62.3485	112.45	
H-C-H (TEGDME) ^b	39.1535	109.55	
H-C-O (TEGDME) ^b	50.8066	108.82	
C-C-O (TEGDME) ^b	67.7342	108.82	
C-C-H (TEGDME) ^b	46.3285	110.07	
F-P-F ^c	139.4	90.0	
Dihedral Parameters			
Dihedral angle	$k_\phi / \text{kcal}\cdot\text{mol}^{-1}$	n	δ / deg
H-C-S-O (DMSO) ^a	0.2	3	0
H-C-S-C (DMSO) ^a	0.2	3	0
H-C-O-C (TEGDME) ^b	0.382738	3	0
C-C-O-C (TEGDME) ^b	0.382738	3	0
C-C-O-C (TEGDME) ^b	0.0999292	2	180
H-C-C-O (TEGDME) ^b	0.249823	1	0
H-C-C-H (TEGDME) ^b	0.155891	3	0
O-C-C-O (TEGDME) ^b	0.143897	3	0
O-C-C-O (TEGDME) ^b	1.17421	2	0

^a Strader and Feller⁹²; ^b Barbosa *et al.*¹⁴; ^c Kumar and Seminario⁸.

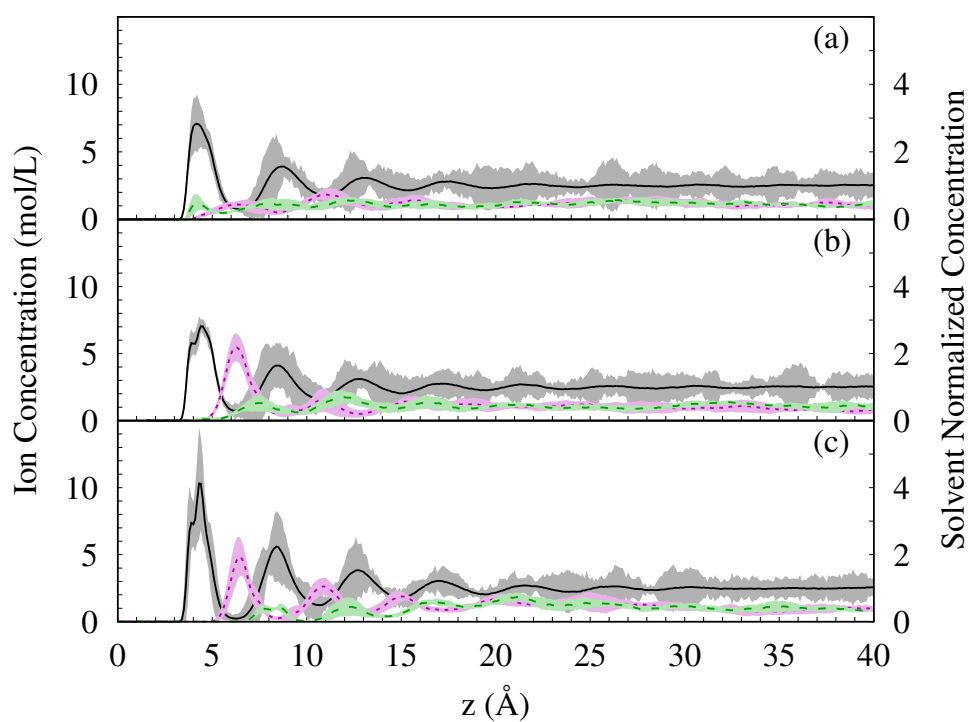


Figure C.2: Local concentration profiles and standard deviation for gold/DMSO systems: ions (left y axis), and solvent (right y axis). DMSO - black solid line; Li^+ - magenta dotted line; PF_6^- - green dashed line. Surface charges applied: (a) zero, (b) $-4.85 \mu\text{C}\cdot\text{cm}^{-2}$, and (c) $-9.7 \mu\text{C}\cdot\text{cm}^{-2}$. The shaded area represents the standard deviation.

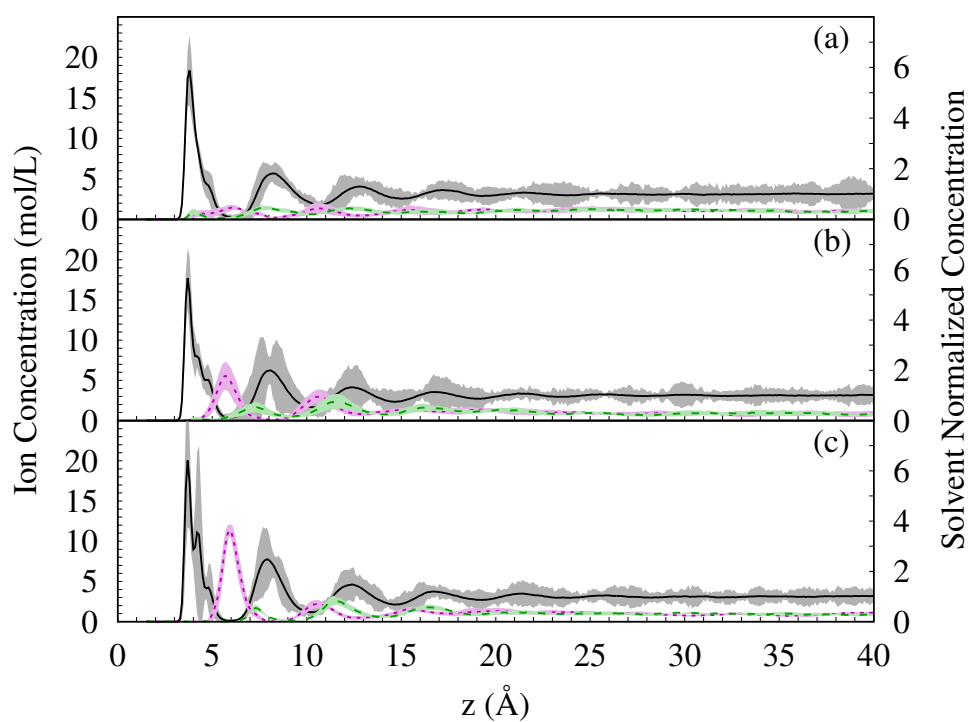


Figure C.3: Local concentration profiles and standard deviation for graphene/DMSO systems: ions (left y axis), and solvent (right y axis). DMSO - black solid line; Li^+ - magenta dotted line; PF_6^- - green dashed line. Surface charges applied: (a) zero, (b) $-4.85 \mu\text{C}\cdot\text{cm}^{-2}$, and (c) $-9.7 \mu\text{C}\cdot\text{cm}^{-2}$. The shaded area represents the standard deviation.

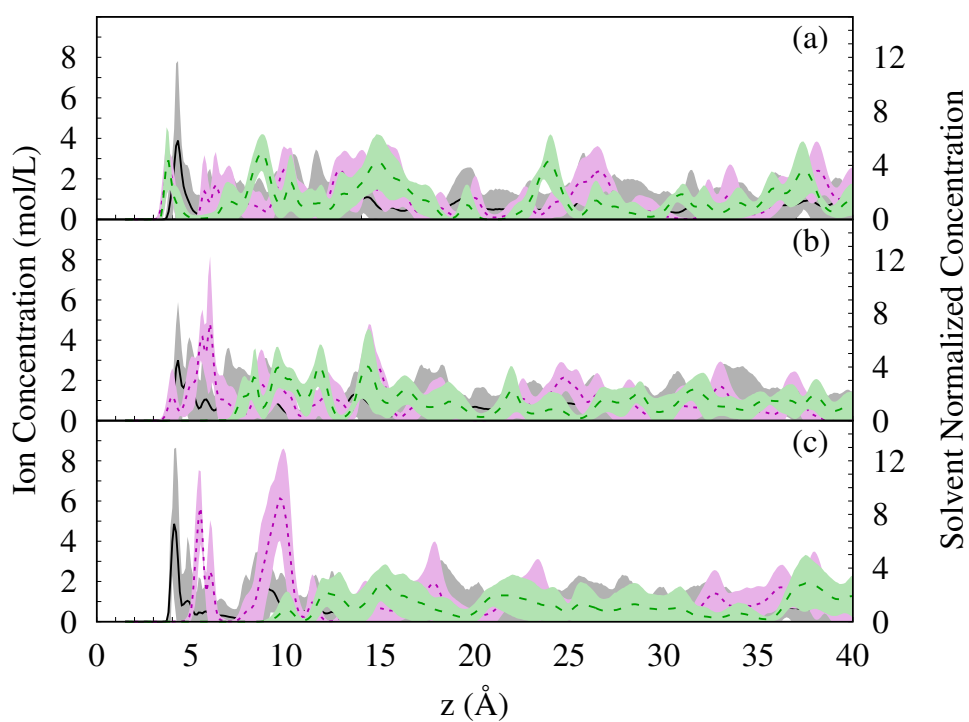
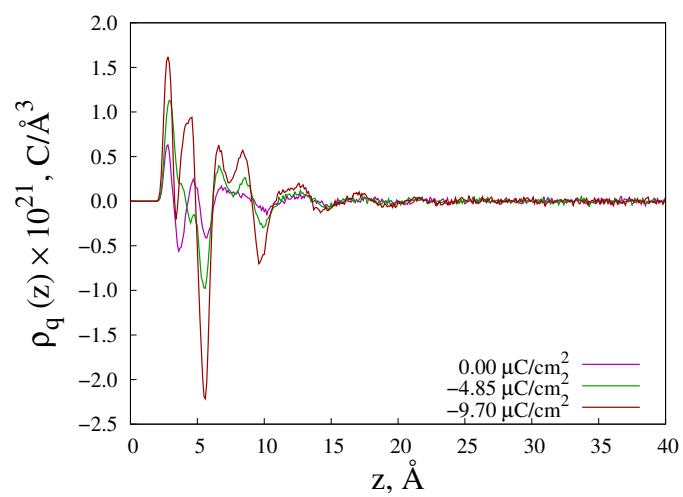
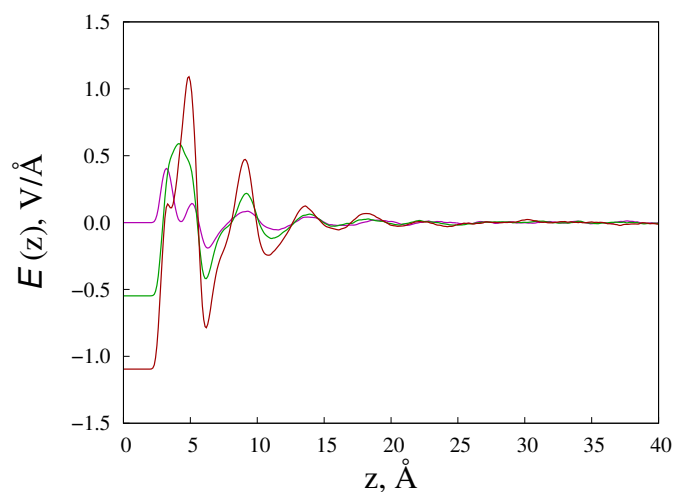


Figure C.4: Local concentration profiles and standard deviation for graphene/TEGDME systems: ions (left y axis), and solvent (right y axis). TEGDME - black solid line; Li^+ - magenta dotted line; PF_6^- - green dashed line. Surface charges applied: (a) zero, (b) $-4.85 \mu\text{C}\cdot\text{cm}^{-2}$, and (c) $-9.7 \mu\text{C}\cdot\text{cm}^{-2}$. The shaded area represents the standard deviation.

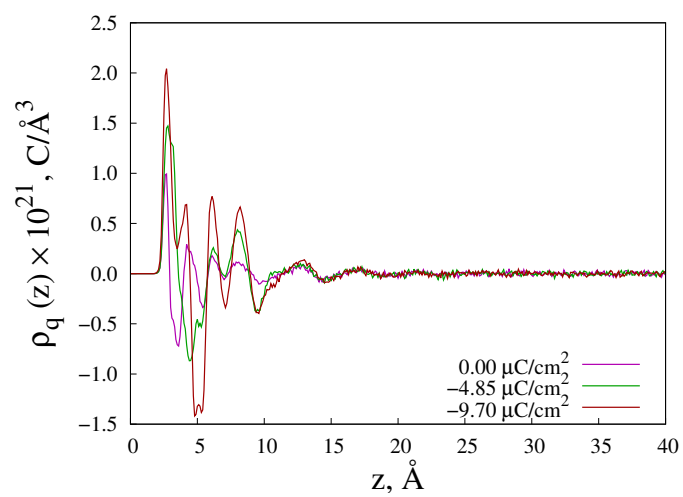


(a)

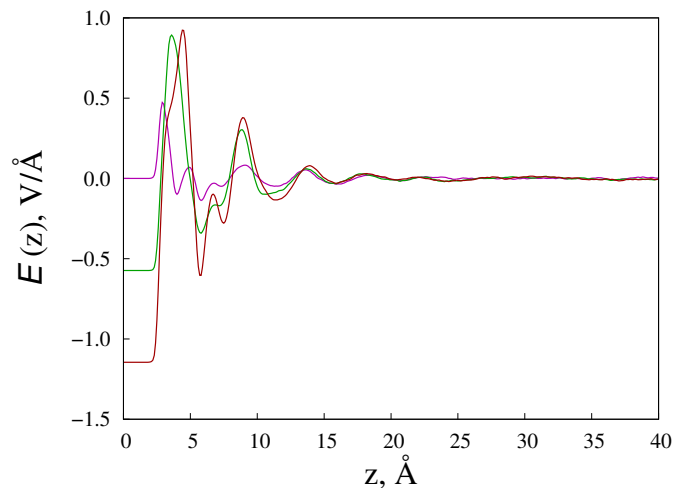


(b)

Figure C.5: Gold/DMSO profiles along z-direction for uncharged and charged electrodes: (a) charge density ($\rho_q(z)$), and (b) electric field ($E(z)$).

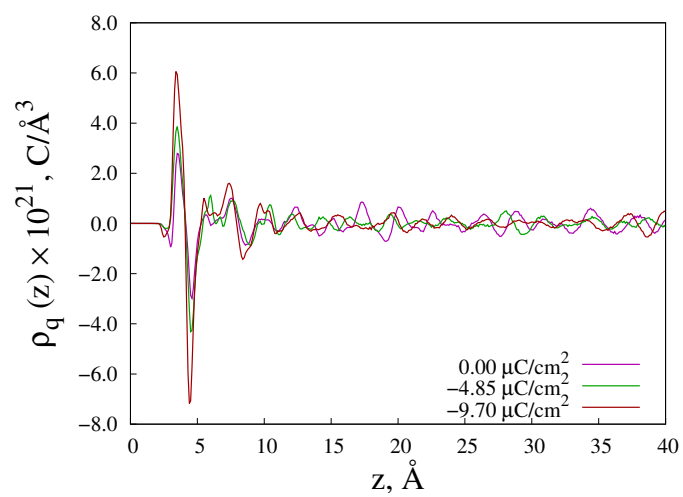


(a)

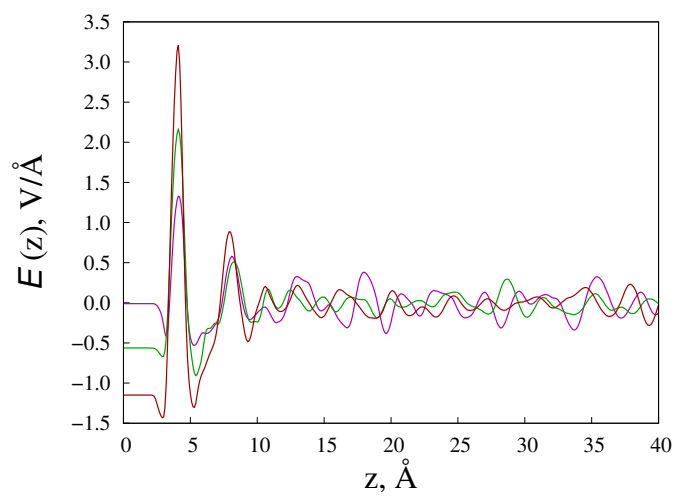


(b)

Figure C.6: Graphene/DMSO profiles along z-direction for uncharged and charged electrodes: (a) charge density ($\rho_q(z)$), and (b) electric field ($E(z)$).



(a)



(b)

Figure C.7: Graphene/TEGDME profiles along z -direction for uncharged and charged electrodes: (a) charge density ($\rho_q(z)$), and (b) electric field ($E(z)$).

Appendix D

LAMMPS and codes files to simulate and calculate properties on confined systems

D.1 LAMMPS running file

```

#Graphene charged/electrolyte
processors * * * grid numa

# Intialization
units          real
dimension      3
boundary       p p f
atom_style     full

variable       NRUNVE equal 20E6
variable       NRUNVP1 equal 2E6
variable       NRUNVP2 equal 2E6
variable       NRUNVP3 equal 2E6
variable       NRUNVP4 equal 2E6
variable       NRUNVP5 equal 2E6
variable       VTEMP equal 298
variable       VPRES equal 1.0
pair_style     lj/charmm/coul/long 10.0 12.0
pair_modify    mix arithmetic
bond_style     harmonic
angle_style    harmonic
dihedral_style charmm
kpace_style    ppm 1.0E-4
kpace_modify   slab 3.0

read_data      mysystem.data

```

```

set          mol 596 charge -0.0260
set          mol 597 charge 0.0260

region      side1 block EDGE EDGE EDGE EDGE -13.225 0.175 side in units
            box
region      side2 block EDGE EDGE EDGE EDGE 76.825 90.225 side in units
            box
region      graphene union 2 side1 side2

group       dmsol type 1 2 3 4
group       li type 5
group       pf6 type 6 7
group       electrolyte union dmsol li pf6
group       carbon type 8
group       all union electrolyte carbon

# Setup atoms
velocity    electrolyte create ${VTEMP} 123 mom yes rot yes dist
            gaussian

# Settings
timestep    1.0
neighbor    2.0 bin
neigh_modify delay 0 every 1 check yes

# Operations
thermo      1
thermo_style custom time temp press pe ke etotal density vol
fix         plates carbon wall/region graphene lj126 0.0859 3.3997 12.0
fix         1 electrolyte nvt temp ${VTEMP} ${VTEMP} 100
fix         2 all balance 10000 1.02 shift xyz 20 1.02

# Restart file
write_restart new_restart.dat

# Action – Equilibration
run         ${NRUNVE}

reset_timestep 0

# Output NVT
dump        myDump1.1 dmsol custom 100 dmsol.data id mol type mass xu yu
            zu
dump        myDump2.1 li custom 5 li1.data id type mass xu yu zu
dump        myDump3.1 pf6 custom 5 pf1.data id type mass xu yu zu
dump        myDump4.1 electrolyte custom 100 gl.data mol type xu yu zu
dump        myDump5.1 all xyz 10000 all1.xyz

```

```
dump          myDump6.1 electrolyte custom 2000 vis1.lammpstrj id type xu
             yu zu q
```

```
# Action – Production1
```

```
run          ${NRUNVP1}
```

```
undump      myDump1.1
```

```
undump      myDump2.1
```

```
undump      myDump3.1
```

```
undump      myDump4.1
```

```
undump      myDump5.1
```

```
undump      myDump6.1
```

```
# Output NVT
```

```
dump        myDump1.2 dms0 custom 100 dms02.data id mol type mass xu yu
             zu
```

```
dump        myDump2.2 li custom 5 li2.data id type mass xu yu zu
```

```
dump        myDump3.2 pf6 custom 5 pf2.data id type mass xu yu zu
```

```
dump        myDump4.2 electrolyte custom 2000 vis2.lammpstrj id type xu
             yu zu q
```

```
# Action – Production2
```

```
run          ${NRUNVP2}
```

```
undump      myDump1.2
```

```
undump      myDump2.2
```

```
undump      myDump3.2
```

```
undump      myDump4.2
```

```
# Output NVT
```

```
dump        myDump1.3 dms0 custom 100 dms03.data id mol type mass xu yu
             zu
```

```
dump        myDump2.3 li custom 5 li3.data id type mass xu yu zu
```

```
dump        myDump3.3 pf6 custom 5 pf3.data id type mass xu yu zu
```

```
dump        myDump4.3 electrolyte custom 2000 vis3.lammpstrj id type xu
             yu zu q
```

```
# Action – Production3
```

```
run          ${NRUNVP3}
```

```
undump      myDump1.3
```

```
undump      myDump2.3
```

```
undump      myDump3.3
```

```
undump      myDump4.3
```

```
# Output NVT
```

```
dump        myDump1.4 dms0 custom 100 dms04.data id mol type mass xu yu
```

```

zu
dump          myDump2.4 li custom 5 li4.data id type mass xu yu zu
dump          myDump3.4 pf6 custom 5 pf4.data id type mass xu yu zu
dump          myDump4.4 electrolyte custom 2000 vis4.lammpstrj id type xu
            yu zu q

# Action – Production4
run           ${NRUNVP4}

undump        myDump1.4
undump        myDump2.4
undump        myDump3.4
undump        myDump4.4

# Output NVT
dump          myDump1.5 dms0 custom 100 dms05.data id mol type mass xu yu
            zu
dump          myDump2.5 li custom 5 li5.data id type mass xu yu zu
dump          myDump3.5 pf6 custom 5 pf5.data id type mass xu yu zu
dump          myDump4.5 electrolyte custom 2000 vis5.lammpstrj id type xu
            yu zu q

# Action – Production5
run           ${NRUNVP5}

undump        myDump1.5
undump        myDump2.5
undump        myDump3.5
undump        myDump4.5

```

D.2 Post processing codes

All the codes presented below were written in C language. The instructions below explain how to run the code and they can be used with any of them:

1. To compile:

```
gcc name.c -lm -o name.exe
```

2. To run:

```
echo input_file | ./name.exe
```

All codes need an input file with specific information that must be provided by the user following the description of section *Reading input file* of the code, the format is shown in the follow example:

name_of_information data

D.2.1 Density distribution and free energy profile (W(z)) code

```

/* **** */
/* School of Chemical Engineering, University of Campinas, Brazil */
/* Code to calculate the density number/concentration and */
/* Free energy distribution (W(z)) */
/* Developer: Juliane Fiates */
/* Supervisor: Dr. Gustavo Doubek and Dr. Luis Fernando Mercier Franco */
/* **** */
#include <stdlib.h>
#include <stdio.h>
#include <math.h>
#include <time.h>

int main () {
    /* **** */
    /* Variables declaration */
    /* **** */
    /* Counters */
    int i, j, l, mol, bin, step;
    /* Avogadro number */
    float na = 6.0221409e23;
    /* Boltzmann constant in J/K */
    float kb = 1.38064852e-23;
    /* Total number of steps */
    int n_steps;
    /* Time */
    int time;
    /* Temperature */
    float T;
    /* Box bounding */
    float bxl, bxu;
    float byl, byu;
    float bzl, bzu;
    /* Total number of molecules */
    int n_mol;
    /* Number of atoms per molecule */
    int n_atoms;
    /* ID number of the first atom in Dump file */
    int st_atom;
    /* ID of the litio atom type */
    int li_tp;
    /* Molecules per frame */
    int af, idx, type;

```

```

/* Masses */
float mass;
/* Total mass */
float totmass;
/* Coordinates */
float x,y,z;
/* Number of bins */
int maxbin;
/* Width of the bin */
float delr;
/* Distance of the histogram */
float rlower;
/* Box size to calculation of the volume */
float boxlx;
float boxly;
float boxlz;
/* Volume in liters */
float voll;
/* Volume in cubic angstrom */
float vol2;
/* Lithium density sum in bulk region */
float rho_sum;
/* Lithium density average in bulk region */
float rho_avg;
/* Input file */
char inpfiler[50];
/* Auxiliary string for comments in the input file */
char com[500];
/* Input file with coordinates */
char cor_file[50];
/* Output file with the concentration distribution */
char cr_file[50];
/* Output file with the free energy distribution */
char A_file[50];

FILE *in, *out;

/* ***** */
/* Reading input file */
/* ***** */
scanf("%s", inpfiler);
in = fopen(inpfiler, "r");
fscanf(in, "%s", com);
fscanf(in, "%d", &n_steps);
fscanf(in, "%s", com);
fscanf(in, "%d", &n_mol);
fscanf(in, "%s", com);

```

```

fscanf(in, "%d", &n_atoms);
fscanf(in, "%s", com);
fscanf(in, "%d", &st_atom);
fscanf(in, "%s", com);
fscanf(in, "%d", &li_tp);
fscanf(in, "%s", com);
fscanf(in, "%f", &totmass);
fscanf(in, "%s", com);
fscanf(in, "%f", &T);
fscanf(in, "%s", com);
fscanf(in, "%d", &maxbin);
fscanf(in, "%s", com);
fscanf(in, "%f", &boxlx);
fscanf(in, "%s", com);
fscanf(in, "%f", &boxly);
fscanf(in, "%s", com);
fscanf(in, "%f", &boxlz);
fscanf(in, "%s", com);
fscanf(in, "%s", cor_file);
fscanf(in, "%s", com);
fscanf(in, "%s", cr_file);
fscanf(in, "%s", com);
fscanf(in, "%s", A_file);
fclose(in);

/* ***** */
/* Memory allocation */
/* ***** */
int r = maxbin;
int c = n_mol*n_atoms;
/* Coordinates */
float *x_n = calloc (c, sizeof (float));
float *y_n = calloc (c, sizeof (float));
float *z_n = calloc (c, sizeof (float));
float *cx = calloc (c, sizeof (float));
float *cy = calloc (c, sizeof (float));
float *cz = calloc (c, sizeof (float));
int *hist = calloc (r, sizeof (int));
/* Concentration in mol/L */
float *cr = calloc (r, sizeof (float));
/* Concentration in number of ions/cubic angstrom */
float *rho = calloc (r, sizeof (float));
/* Free energy in kJ/mol */
float *A = calloc (r, sizeof (float));

/* ***** */
/* Reading the coordinates input file */

```

```

/*****
printf("Reading input file...\n");
in = fopen(cor_file , "r");
for (step = 0; step < n_steps; step++){
    fscanf(in , "%d", &time);
    fscanf(in , "%d", &af);
    fscanf(in , "%e %e", &bxl , &bxu);
    fscanf(in , "%e %e", &byl , &byu);
    fscanf(in , "%e %e", &bzl , &bzu);
    for (j = 0; j < (n_mol*n_atoms); j++){
        fscanf(in , "%d %d %f %f %f %f", &idx , &type , &mass , &x ,
            &y , &z);
        x = x-boxlx*round(x/boxlx);
        y = y-boxly*round(y/boxly);
        x_n[idx]=(x*mass)/totmass;
        y_n[idx]=(y*mass)/totmass;
        z_n[idx]=(z*mass)/totmass;
    }

/*****
/* Calculation of coordinates at center of mass of the molecule */
/*****
i=0;
for (idx=st_atom ; idx <(st_atom+(n_mol*n_atoms)) ; idx=idx+n_atoms)
{
    cx[i] = 0.0;
    cy[i] = 0.0;
    cz[i] = 0.0;
    for (l = 0; l < n_atoms; l++){
        cx[i] = cx[i]+x_n[idx+l];
        cy[i] = cy[i]+y_n[idx+l];
        cz[i] = cz[i]+z_n[idx+l];
    }
    i++;
}

/*****
/* Histogram calculation */
/*****
delr = 0.5*boxlz/(float)(maxbin);
for (i= 0; i < n_mol; i++){
    bin = (int)(cz[i]/delr);
    if (bin<=maxbin)
        hist[bin]=hist[bin]+1;
}
}
fclose(in);

```

```

/* ***** */
/* Calculation of the concentration profile and free energy */
/* ***** */
printf("Calculating the concentration...\n");
out = fopen(cr_file , "w");
vol1 = (boxlx*boxly*delr)/(1e27);
vol2 = boxlx*boxly*delr;
for(bin = 0; bin < maxbin; bin++){
    rlower = (float)(bin)*delr;
    cr[bin] = (float)(hist[bin])/(float)(n_steps)/na/vol1;
    rho[bin]= (float)(hist[bin])/(float)(n_steps)/vol2;
    fprintf(out,"%e %e %e \n", rlower , cr[bin], rho[bin]);
}
fclose (out);

if(type == li_tp){
    out = fopen(A_file , "w");
    printf("Calculating the free energy...\n");
    rho_sum = 0.0;
    for(bin = 300; bin < 500; bin++){
        rho_sum = rho_sum+rho[bin];
    }
    rho_avg = rho_sum/200.0;

    for(bin = 0; bin < maxbin; bin++){
        rlower = (float)(bin)*delr;
        A[bin]= -kb*na*T*log (rho[bin]/rho_avg);
        fprintf(out,"%e %e \n", rlower , A[bin]/1000.0);
    }
    fclose (out);
}
return 0;
}

```

D.2.2 Integral of the normalized concentration code

```

/* ***** */
/* School of Chemical Engineering, University of Campinas, Brazil */
/* Code to calculate the integral of the normalized concentration */
/* Developer: Juliane Fiates */
/* Supervisor: Dr. Gustavo Doubek and Dr. Luis Fernando Mercier Franco */
/* ***** */
#include <stdlib.h>
#include <stdio.h>
#include <math.h>
#include <time.h>

```

```

int main (){
    /* ***** */
    /* Variables declaration */
    /* ***** */
    /* Counters */
    int i, j, k, l, mol, bin, step;
    /* Number of bins */
    int maxbin, maxint;
    /* Width of the bin */
    float delr, std;
    /* Box size to calculation of the volume */
    float boxlz;
    /* Lithium density sum in bulk region */
    double rho_sum;
    /* Lithium density average in bulk region */
    double rho_avg;
    /* Concentration number */
    float n;
    /* Input file */
    char inpfile[50];
    /* Auxiliary string for comments in the input file */
    char com[500];
    /* Input file with coordinates */
    char dens_file[50];
    /* Output file with the concentration number */
    char rho_file[50], n_file[50];

    FILE *in, *out;

    /* ***** */
    /* Reading input file */
    /* ***** */
    scanf("%s", inpfile);
    in = fopen(inpfile, "r");
    fscanf(in, "%s", com);
    fscanf(in, "%d", &maxbin);
    fscanf(in, "%s", com);
    fscanf(in, "%d", &maxint);
    fscanf(in, "%s", com);
    fscanf(in, "%f", &boxlz);
    fscanf(in, "%s", com);
    fscanf(in, "%s", dens_file);
    fscanf(in, "%s", com);
    fscanf(in, "%s", rho_file);
    fscanf(in, "%s", com);
    fscanf(in, "%s", n_file);

```

```

fclose(in);

/* ***** */
/* Memory allocation */
/* ***** */
int b = maxbin;
/* Concentration in number of ions/cubic angstrom */
double *rho = calloc (b, sizeof (double));
/* Concentration number (integral of rho) */
double *rho_n = calloc (b, sizeof (double));
float *r = calloc (b, sizeof (float));
float *rlower = calloc (b, sizeof (float));

/* ***** */
/* Reading the coordinates input file */
/* ***** */
printf("Reading input file...\n");
in = fopen(dens_file, "r");
delr = boxlz/(float)(maxbin);
for(bin = 0; bin < maxbin; bin++){
    fscanf(in, "%e %lf %e \n", &rlower[bin], &rho[bin], &std);
}
fclose(in);

out = fopen(rho_file, "w");
printf("Calculating the normalized concentration...\n");
rho_sum = 0.0;
for(bin = 300; bin < 500; bin++){
    rho_sum = rho_sum+rho[bin];
}
rho_avg = rho_sum/200.0;

for(bin = 0; bin < maxbin; bin++){
    rho_n[bin] = rho[bin]/rho_avg;
    fprintf(out, "%e %lf \n", rlower[bin], rho_n[bin]);
}

/* ***** */
/* Calculation of the concentration number (n) */
/* ***** */
printf("Integration of the concentration...\n");
out = fopen(n_file, "w");
for (bin = 0; bin < maxint; bin++){
    r[bin] = (float)(bin)*delr;
    n = rho_n[0];
    for (k = 1; k < bin-1; k++)
        n = n+2.0*rho_n[k];
}

```

```

        n = 0.5*(r[k]-r[0])*(n+rho_n[k])/(float)(bin-1);
        if (k > 1)
            fprintf(out, "%e %e \n", r[k]-r[0], n);
    }
    fclose (out);
    return 0;
}

```

D.2.3 Radial distribution function and coordination number code

```

/* ***** */
/* School of Chemical Engineering, University of Campinas, Brazil */
/* Code to calculate the radial distribution function */
/* and the coordinate number */
/* at the interfacial-layer based on atoms type */
/* Developer: Juliane Fiates */
/* Supervisor: Dr. Gustavo Doubek and Dr. Luis Fernando Mercier Franco */
/* ***** */
#include <stdlib.h>
#include <stdio.h>
#include <math.h>
#include <time.h>
#include <string.h>

int main(){
    /* ***** */
    /* Variables declaration */
    /* ***** */
    /* Counters */
    int i,j,k,bin,step,idx;
    /* Interfacial-layer size (position) */
    float zcut;
    /* Molecules per frame */
    int af,type;
    /* Box size fom dump file */
    float bxl,bxu;
    float byl,byu;
    float bzl,bzu;
    /* Time */
    int time;
    /* Total number of steps */
    int n_steps;
    /* Total number of molecules */
    int n_molt;
    /* Atom types used to compute the distribution function */
    int tp_1,tp_2;
    /* Number of atoms inside of the layer region */

```

```

int cont1 ,cont2 ,sum_atm1 ,sum_atm2;
/* Average number of atoms inside of the layer region */
float atm1_avg ,atm2_avg;
/* Coordinates */
float x,y,z;
/* Width of the bin */
float delr;
/* The lower value of radius */
float rlower;
/* The upper value of radius */
float rupper;
/* Number of ideal gas particles at same density */
float nideal;
/* Number of bins */
int maxbin;
/* Box size */
float boxlx ,boxly ,boxlz;
/* Box size average */
float boxlsq ,boxl;
/* Volume */
float vol;
/* Distance between the atoms */
float rxij ,ryij ,rzij ,rijsq ,rij;
/* Coordination number */
float n;
/* Input file */
char inpfile[50];
/* Auxiliary string for comments in the input file */
char com[500];
/* Input file with the coordinates */
char cor_file[50];
/* Output file with the RDF */
char g_file[50];
/* Output file with the coordination number */
char n_file[50];

FILE *in , *out;

/* ***** */
/* Reading input file */
/* ***** */
scanf("%s" , inpfile);
in = fopen(inpfile , "r");
fscanf(in , "%s" , com);
fscanf(in , "%d" , &n_steps);
fscanf(in , "%s" , com);
fscanf(in , "%f" , &zcut);

```

```

fscanf(in, "%s", com);
fscanf(in, "%d", &n_molt);
fscanf(in, "%s", com);
fscanf(in, "%d", &tp_1);
fscanf(in, "%s", com);
fscanf(in, "%d", &tp_2);
fscanf(in, "%s", com);
fscanf(in, "%d", &maxbin);
fscanf(in, "%s", com);
fscanf(in, "%f", &boxlx);
fscanf(in, "%s", com);
fscanf(in, "%f", &boxly);
fscanf(in, "%s", com);
fscanf(in, "%f", &boxlz);
fscanf(in, "%s", com);
fscanf(in, "%s", cor_file);
fscanf(in, "%s", com);
fscanf(in, "%s", g_file);
fscanf(in, "%s", com);
fscanf(in, "%s", n_file);
fclose(in);

/*****
/* Memory allocation
*****/
int c = n_molt;
int a = maxbin;
/* Coordinates of atom 1 and 2 */
float *rx_i = calloc (c, sizeof (float));
float *ry_i = calloc (c, sizeof (float));
float *rz_i = calloc (c, sizeof (float));
float *rx_j = calloc (c, sizeof (float));
float *ry_j = calloc (c, sizeof (float));
float *rz_j = calloc (c, sizeof (float));
/* Histogram and RDF */
int *hist = calloc (a, sizeof (int));
float *gr = calloc (a, sizeof (float));
float *gr_n = calloc (a, sizeof (float));
float *r = calloc (a, sizeof (float));

/*****
/* Reading the coordinates input file
*****/
printf("Reading input file...\n");
in = fopen(cor_file, "r");
for (step = 0; step < n_steps; step++){
    fscanf(in, "%d", &time);

```

```

fscanf(in, "%d", &af);
fscanf(in, "%e %e", &bxl, &bxu);
fscanf(in, "%e %e", &byl, &byu);
fscanf(in, "%e %e", &bzl, &bzu);
cont1 = 0;
cont2 = 0;
for (i = 0; i < n_molt; i++){
    fscanf(in, "%d %d %f %f %f", &idx, &type, &x, &y, &z);
    /* ***** */
    /* If it is the negative wall (z <=) */
    /* If it is the positive wall (z >=) */
    /* ***** */
    if (z <= zcut){
        if (type == tp_1){
            rx_i[cont1] = x;
            ry_i[cont1] = y;
            rz_i[cont1] = z;
            sum_atm1 += 1;
            cont1++;
        }
        if (type == tp_2){
            rx_j[cont2] = x;
            ry_j[cont2] = y;
            rz_j[cont2] = z;
            sum_atm2 += 1;
            cont2++;
        }
    }
}

/* ***** */
/* Calculation of the histogram */
/* ***** */

/* ***** */
/* If it is the negative wall z will be equal zcut */
/* If it is the positive wall z will be equal boxlz-zcut */
/* ***** */
vol=boxlx*boxly*zcut;
boxl=pow(vol,(1.0/3.0));
delr=(0.5*boxl)/(float)(maxbin);
for (i = 0; i < cont1; i++){
    for (j = 0; j < cont2; j++){
        rxij = rx_i[i]-rx_j[j];
        ryij = ry_i[i]-ry_j[j];
        rzij = rz_i[i]-rz_j[j];
        rxij = rxij-boxlx*round(rxij/boxlx);
    }
}

```

```

        ryij = ryij - boxly * round(ryij / boxly);
        rijsq = rxij * rxij + ryij * ryij + rzij * rzij;
        rij = pow(rijsq, (1.0 / 2.0));
        bin = (int) (rij / delr) + 1;
        if (bin <= maxbin)
            hist[bin] = hist[bin] + 1;
    }
}
fclose (in);

/* ***** */
/* Calculation of the Radial Distribution Function (RDF) */
/* ***** */
printf("Calculating the RDF...\n");
out = fopen(g_file, "w");
atm1_avg = (float)(sum_atm1) / (float)(n_steps);
atm2_avg = (float)(sum_atm2) / (float)(n_steps);
float cons_g = (4.0 * M_PI * ((atm1_avg * atm2_avg) / vol)) / 3.0;
float cons_n = (atm2_avg / vol) * 4.0 * M_PI;
for (bin = 0; bin < maxbin; bin++){
    rlower = (float)(bin) * delr;
    rupper = rlower + delr;
    nideal = cons_g * ((rupper * rupper * rupper) - (rlower * rlower *
        rlower));
    gr[bin] = (float)(hist[bin]) / (float)(n_steps) / nideal;
    gr_n[bin] = gr[bin] * (rlower * rlower);
    fprintf(out, "%e %e \n", rlower, gr[bin]);
}
fclose (out);

/* ***** */
/* Calculation of the coordination number (n) */
/* ***** */
printf("Integration of the RDF...\n");
out = fopen(n_file, "w");
for (bin = 0; bin < maxbin; bin++){
    r[bin] = (float)(bin) * delr;
    n = gr_n[0];
    for (k = 1; k < bin - 1; k++){
        n = n + 2.0 * gr_n[k];
    }
    n = cons_n * 0.5 * (r[k] - r[0]) * (n + gr_n[k]) / (float)(bin - 1);
    if (k > 1)
        fprintf(out, "%e %e \n", r[k] - r[0], n);
}
fclose (out);

```

```

    return 0;
}

```

D.2.4 Order parameter code ($P_2(\cos \theta)$)

```

/*****
/* School of Chemical Engineering, University of Campinas, Brazil */
/* Code to calculate the P2(cos theta) order parameter */
/* Developer: Juliane Fiates */
/* Supervisor: Dr. Gustavo Doubek and Dr. Luis Fernando Mercier Franco */
/*****
#include <stdlib.h>
#include <stdio.h>
#include <math.h>
#include <time.h>
#include <string.h>

int main(){
    /*****
    /* Variables declaration */
    /*****
    /* Counters */
    int i, bin, step, idx, j, l, cont1, cont2;
    /* Molecules per frame */
    int af, type;
    /* Box size fom dump file */
    float bxl, bxu;
    float byl, byu;
    float bzl, bzu;
    /* Time */
    int time;
    /* Total number of steps */
    int n_steps;
    /* Total number of molecules */
    int n_mol;
    /* Number of atoms per molecule */
    int n_atoms;
    /* ID number of the first atom in Dump file */
    int st_atom;
    /* Masses */
    float mass;
    /* Total mass */
    float totmass;
    /* Atom types used to calculate the vector S/O */
    int tp_1, tp_2;
    /* Coordinates */
    float x, y, z;

```

```

/* Distance coordinates between S/O and S/z direction */
float x_so, y_so, z_so, x_s0, y_s0, z_s1;
/* Vector module resultant of product S/O and S/z */
float r_so_sq, r_so, r_sz_sq, r_sz, pr_so_sz;
/* Cosine of the angle between S/O and S/z */
float cos_th, cos_th_sq;
/* Width of the bin */
float delr;
/* Distance of the histogram */
float rlower;
/* Number of bins */
int maxbin;
/* Box size */
float boxlx, boxly, boxlz;
/* Input file */
char inpfile[50];
/* Auxiliary string for comments in the input file */
char com[500];
/* Input file with the coordinates */
char cor_file[50];
/* Output file with the P2 order parameter */
char p_file[50];

FILE *in, *out;

/* ***** */
/* Reading input file */
/* ***** */
scanf("%s", inpfile);
in = fopen(inpfile, "r");
fscanf(in, "%s", com);
fscanf(in, "%d", &n_steps);
fscanf(in, "%s", com);
fscanf(in, "%d", &n_mol);
fscanf(in, "%s", com);
fscanf(in, "%d", &n_atoms);
fscanf(in, "%s", com);
fscanf(in, "%d", &st_atom);
fscanf(in, "%s", com);
fscanf(in, "%f", &totmass);
fscanf(in, "%s", com);
fscanf(in, "%d", &tp_1);
fscanf(in, "%s", com);
fscanf(in, "%d", &tp_2);
fscanf(in, "%s", com);
fscanf(in, "%d", &maxbin);
fscanf(in, "%s", com);

```

```

fscanf(in, "%f", &boxlx);
fscanf(in, "%s", com);
fscanf(in, "%f", &boxly);
fscanf(in, "%s", com);
fscanf(in, "%f", &boxlz);
fscanf(in, "%s", com);
fscanf(in, "%s", cor_file);
fscanf(in, "%s", com);
fscanf(in, "%s", p_file);
fclose(in);

/* ***** */
/* Memory allocation */
/* ***** */
int r = maxbin;
int c = n_mol*n_atoms;
int o = n_mol;

/* Coordinates */
float *x_s = calloc (o, sizeof (float));
float *y_s = calloc (o, sizeof (float));
float *z_s = calloc (o, sizeof (float));
float *x_o = calloc (o, sizeof (float));
float *y_o = calloc (o, sizeof (float));
float *z_o = calloc (o, sizeof (float));
float *x_n = calloc (c, sizeof (float));
float *y_n = calloc (c, sizeof (float));
float *z_n = calloc (c, sizeof (float));
float *cx = calloc (c, sizeof (float));
float *cy = calloc (c, sizeof (float));
float *cz = calloc (c, sizeof (float));
/* Histograms of P2 and number of atoms */
float *hist = calloc (r, sizeof (float));
int *num = calloc (r, sizeof (int));
/* P2(cos theta) order parameter */
float *p2 = calloc (r, sizeof (float));
float *p2_avg = calloc (r, sizeof (float));

/* ***** */
/* Reading the coordinates input file */
/* ***** */
printf("Reading input file...\n");
in = fopen(cor_file, "r");
for (step = 0; step < n_steps; step++){
    fscanf(in, "%d", &time);
    fscanf(in, "%d", &af);
    fscanf(in, "%e %e", &bxl, &bxu);

```

```

fscanf(in, "%e %e", &byl, &byu);
fscanf(in, "%e %e", &bzl, &bzu);
cont1=0;
cont2=0;
for (j = 0; j < (n_mol*n_atoms); j++){
    fscanf(in, "%d %d %f %f %f %f", &idx, &type, &mass, &x,
        &y, &z);
    x = x-boxlx*round(x/boxlx);
    y = y-boxly*round(y/boxly);
    x_n[idx]=(x*mass)/totmass;
    y_n[idx]=(y*mass)/totmass;
    z_n[idx]=(z*mass)/totmass;
    if(type == tp_1){
        x_s[cont1] = x;
        y_s[cont1] = y;
        z_s[cont1] = z;
        cont1++;
    }
    if(type == tp_2){
        x_o[cont2] = x;
        y_o[cont2] = y;
        z_o[cont2] = z;
        cont2++;
    }
}

/*****
/* Calculation of coordinates at center of mass of the molecule */
/*****
i=0;
for (idx=st_atom; idx < (st_atom+(n_mol*n_atoms)); idx=idx+n_atoms)
{
    cx[i] = 0.0;
    cy[i] = 0.0;
    cz[i] = 0.0;
    for (l = 0; l < n_atoms; l++){
        cx[i] = cx[i]+x_n[idx+l];
        cy[i] = cy[i]+y_n[idx+l];
        cz[i] = cz[i]+z_n[idx+l];
    }
    i++;
}

/*****
/* Calculation of P2(cos theta) order parameter */
/*****
delr = boxlz/(float)(maxbin);

```

```

    for (i = 0; i < n_mol; i++){
        x_so = x_o[i]-x_s[i];
        y_so = y_o[i]-y_s[i];
        z_so = z_o[i]-z_s[i];
        x_s0 = 0.0-x_s[i];
        y_s0 = 0.0-y_s[i];
        z_s1 = 1.0-z_s[i];
        pr_so_sz = (x_so*x_s0)+(y_so*y_s0)+(z_so*z_s1);
        r_so_sq = (x_so*x_so)+(y_so*y_so)+(z_so*z_so);
        r_sz_sq = (x_s0*x_s0)+(y_s0*y_s0)+(z_s1*z_s1);
        r_so = pow(r_so_sq,(1.0/2.0));
        r_sz = pow(r_sz_sq,(1.0/2.0));
        cos_th = pr_so_sz/(r_so*r_sz);
        cos_th_sq = (cos_th*cos_th);
        bin = (int)(cz[i]/delr);
        p2[bin] = cos_th_sq;
        if(bin<=(maxbin)){
            hist[bin] = hist[bin]+p2[bin];
        }
    }

}

fclose (in);

/* ***** */
/* Calculation of the P2(cos theta) profile in z direction */
/* ***** */
printf("Calculating the P2 order parameter...\n");
out = fopen(p_file , "w");
for(bin=0; bin < maxbin; bin++){
    rlower = (float)(bin)*delr;
    p2_avg[bin] = (3.0/2.0)*(hist[bin]/(float)(n_steps))-(1.0/2.0);
    fprintf(out,"%e %e \n", rlower , p2_avg[bin]);
}
fclose (out);

return 0;
}

```

D.2.5 Charge density and electric field code

```

/* ***** */
/* School of Chemical Engineering, University of Campinas, Brazil */
/* Code to calculate the charge density and the electric field */
/* Developer: Juliane Fiates */
/* Supervisor: Dr. Gustavo Doubek and Dr. Luis Fernando Mercier Franco */

```

```

/*****
#include <stdlib.h>
#include <stdio.h>
#include <math.h>
#include <time.h>
#include <string.h>

int main(){
    /*****
    /* Variables declaration */
    /*****
    /* Counters */
    int i, bin, step, idx, k;
    /* Vacuum electric permittivity in Farad per meters */
    double E0 = 8.8541878128e-12;
    /* Elementary charge in Coulomb */
    double ee = 1.60217654e-19;
    /* Molecules per frame */
    int af, type;
    /* Box size fom dump file */
    float bxl, bxu;
    float byl, byu;
    float bzl, bzu;
    /* Time */
    int time;
    /* Total number of steps */
    int n_steps;
    /* Total number of atoms in the system */
    int n_atoms;
    /* Coordinates */
    float x, y, z;
    /* Atom charge */
    float q;
    /* Width of the bin */
    float delr;
    /* Distance of the histogram */
    float rlower;
    /* Number of bins */
    int maxbin;
    /* Box size to calculation of the volume */
    float boxlx;
    float boxly;
    float boxlz;
    /* Volume in cubic angstrom */
    float vol;
    /* Electric field in volts per angstrom */
    float elec;

```

```

/* Input file */
char infile[50];
/* Auxiliary string for comments in the input file */
char com[500];
/* Input file with the coordinates and charges */
char cor_file[50];
/* Output files */
char ch_file[50];
char elec_file[50];

FILE *in, *out;

/* *****/
/* Reading input file */
/* *****/
scanf("%s", infile);
in = fopen(infile, "r");
fscanf(in, "%s", com);
fscanf(in, "%d", &n_steps);
fscanf(in, "%s", com);
fscanf(in, "%d", &n_atoms);
fscanf(in, "%s", com);
fscanf(in, "%d", &maxbin);
fscanf(in, "%s", com);
fscanf(in, "%f", &boxlx);
fscanf(in, "%s", com);
fscanf(in, "%f", &boxly);
fscanf(in, "%s", com);
fscanf(in, "%f", &boxlz);
fscanf(in, "%s", com);
fscanf(in, "%s", cor_file);
fscanf(in, "%s", com);
fscanf(in, "%s", ch_file);
fscanf(in, "%s", com);
fscanf(in, "%s", elec_file);
fclose(in);

/* *****/
/* Memory allocation */
/* *****/
int b = maxbin;

/* Histogram */
float *hist = calloc (b, sizeof (float));
float *r = calloc (b, sizeof (float));
/* Charge density */
float *ch = calloc (b, sizeof (float));

```

```

float *ch_avg = calloc (b, sizeof (float));

/*****
/* Reading the charge and position input file
*****/
printf("Reading input file...\n");
in = fopen(cor_file , "r");
delr =boxlz/(float)(maxbin);
for (step = 0; step < n_steps; step++){
    fscanf(in, "%d", &time);
    fscanf(in, "%d", &af);
    fscanf(in, "%e %e", &bxl, &bxu);
    fscanf(in, "%e %e", &byl, &byu);
    fscanf(in, "%e %e", &bzl, &bzu);
    for (i = 0; i < n_atoms; i++){
        fscanf(in, "%d %d %f %f %f %f", &idx, &itype, &x, &y, &z,
            &q);
        bin = (int)(z/delr);
        ch[bin] = q*ee;
        if(bin<=maxbin){
            hist[bin]=hist[bin]+ch[bin];
        }
    }
}
fclose (in);

/*****
/* Calculation of the charge density profile (C/A3)
*****/
printf("Calculating the charge density profiles...\n");
vol = (boxlx*boxly*delr);
out = fopen(ch_file , "w");
for(bin=0; bin < maxbin; bin++){
    rlower = (float)(bin)*delr;
    ch_avg[bin] = hist[bin]/(float)(n_steps)/vol;
    fprintf(out,"%e %e \n", rlower, ch_avg[bin]);
}
fclose (out);

/*****
/* Calculation of the electric field (V/A)
*****/
printf("Integration of the charge density to calculate the electric
    field...\n");
out = fopen(elec_file , "w");
for (bin = 0; bin < maxbin; bin++){
    r[bin] = (float)(bin)*delr;

```

```

        elec    = ch_avg[0];
        for (k = 1; k < bin-1; k++)
            elec = elec+2.0*ch_avg[k];
        elec = (1.0/E0)*1E10*0.5*(r[k]-r[0])*(elec+ch_avg[k])/(float)(
            bin-1);
        if (k > 1)
            fprintf(out, "%e %e \n", r[k]-r[0], elec);
    }
fclose (out);

return 0;
}

```

D.2.6 Electrostatic potential code

```

/*****
/* School of Chemical Engineering, University of Campinas, Brazil */
/* Code to calculate the electrostatic potential based on */
/* integration of the electric field */
/* Developer: Juliane Fiates */
/* Supervisor: Dr. Gustavo Doubek and Dr. Luis Fernando Mercier Franco */
/* Note: the elec_avg value comes from fitting of bulk electric field */
*****/
#include <stdlib.h>
#include <stdio.h>
#include <math.h>
#include <time.h>

int main (){
    /*****
    /* Variables declaration */
    *****/
    /*****
    /* Counters */
    int i, j, k, l, mol, bin, step;
    /* Number of bins */
    int maxbin;
    /* Width of the bin */
    float delr;
    /* Box size to calculation of the volume */
    float boxlz;
    /* Averaged electrical field at the bulk region */
    float elec_avg;
    /* Electrostatic potential in Volts */
    float pot;
    /* Input file */
    char infile[50];
    /* Auxiliary string for comments in the input file */

```

```

char com[500];
/* Input file with coordinates */
char elec_file[50];
/* Output file with the concentration number */
char pot_file[50];

FILE *in, *out;

/* ***** */
/* Reading input file */
/* ***** */
scanf("%s", inpfiler);
in = fopen(inpfiler, "r");
fscanf(in, "%s", com);
fscanf(in, "%d", &maxbin);
fscanf(in, "%s", com);
fscanf(in, "%f", &boxlz);
fscanf(in, "%s", com);
fscanf(in, "%f", &elec_avg);
fscanf(in, "%s", com);
fscanf(in, "%s", elec_file);
fscanf(in, "%s", com);
fscanf(in, "%s", pot_file);
fclose(in);

/* ***** */
/* Memory allocation */
/* ***** */
int b = maxbin;

/* Electric field */
double *elec = calloc (b, sizeof (double));
double *elec_n = calloc (b, sizeof (double));
float *r = calloc (b, sizeof (float));
float *rlower = calloc (b, sizeof (float));

/* ***** */
/* Reading the electrical field input file */
/* ***** */
printf("Reading input file...\n");
in = fopen(elec_file, "r");
delr = boxlz/(float)(maxbin);
for(bin = 0; bin < maxbin; bin++){
    fscanf(in, "%e %lf \n", &rlower[bin], &elec[bin]);
    elec_n[bin]=elec[bin]-elec_avg;
}
fclose(in);

```

```

/* ***** */
/* Calculation of the potential */
/* ***** */
printf("Integration of the electrical field ...\n");
out = fopen(pot_file , "w");
for (bin = 0; bin < maxbin; bin++){
    r[bin] = (float)(bin)*delr;
    pot     = elec_n[0];
    for (k = 1; k < bin-1; k++)
        pot = pot+2.0*elec_n[k];
    pot = -0.5*(r[k]-r[0])*(pot+elec_n[k])/(float)(bin-1);
    if (k > 1)
        fprintf(out, "%e %e \n", r[k]-r[0], pot);
}
fclose (out);
return 0;
}

```

D.2.7 Electrostatic potential calculation using LAMMPS

Alternatively the calculation of electrostatic potential can be performed using AtC subroutine implemented in LAMPPS¹⁴⁹. More details about the method can be found in Templeton *et al.*¹⁴⁹.

```

#Calculation of potential

# Intialization
units          real
dimension      3
boundary       p p f
atom_style     full

pair_style     lj/charmm/coul/long 10.0 12.0
pair_modify    mix arithmetic
bond_style     harmonic
angle_style    harmonic
dihedral_style charmm
kpace_style    ppm 1.0E-4
kpace_modify   slab 3.0

read_restart   new_restart.data

variable       NMESHX equal 1
variable       NMESHY equal 1
variable       NMESHZ equal 800

```

```
lattice          sc 1

fix              ATC all atc field
region          BOX block EDGE EDGE EDGE EDGE -13.225 90.225
fix_modify      ATC mesh create ${NMESHX} ${NMESHY} ${NMESHZ} BOX p p f
fix_modify      ATC atom_element_map eulerian 1
fix_modify      ATC fields add electric_potential
fix_modify      ATC output out.atc_potential 2000 text binary

rerun           vis1.lammpstrj dump x y z q
```